Laser Control and Spectroscopy of Molecular Vibrations and Reaction Dynamics

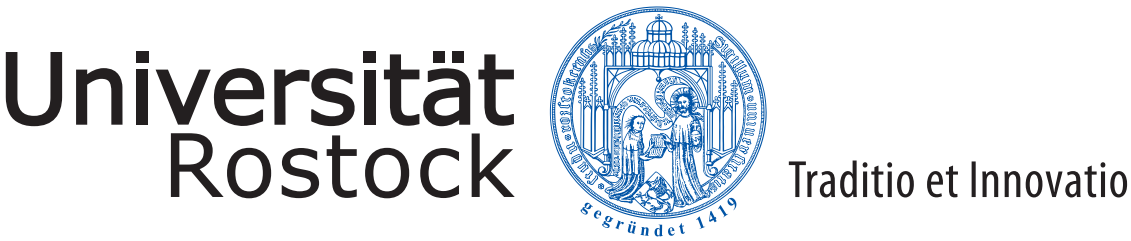

Dissertation
zur
Erlangung des akademischen Grades
doctor rerum naturalium (Dr. rer. nat.)
der Mathematisch-Naturwissenschaftlichen Fakultät
der Universität Rostock

vorgelegt von

Mateusz Lisaj

Rostock, 2015

urn:nbn:de:gbv:28-diss2015-0132-4

Gutachter:

1. Gutachter:

   Prof. Dr. Oliver Kühn,

   Institut für Physik, Universität Rostock

2. Gutachter:

   Priv. Doz. Dr. habil. Volkhard May,

   Institut für Physik, Humboldt Universität zu Berlin

Datum der Einreichung: 19.05.2015

Datum der Verteidigung: 22.07.2015

To my lovely parents,
and wise teachers.

Contents

Glossary

4D Four-Dimensional
B3LYP Becke 3-Parameter (Exchange), Lee, Yang and Parr
BS Bulirsch-Stoer
BSSE Basis Set Superposition Error
CMF Constant Mean Field
DFT Density Functional Theory
DMS Dipole Moment Surface
DOF(s) Degree(s) of Freedom
DVR Discrete Variable Representation
ECP Effective Core Potential
EOM(s) Equation(s) of Motion
EX Exchange-Correlation
FFT Fast Fourier Transform
FWHM Full Width at Half Maximum
GTO(s) Gaussian Type Orbital(s)
HF Hartree Fock
HK Hohenberg-Kohn
HO DVR Harmonic Oscillator DVR
IR Infrared
IRC Intrinsic Reaction Coordinate
IVR Intramolecular Vibrational Energy Redistribution
LanL2DZ Los Alamos ECP
LSDA Local Spin-Density Approximation
MCTDH Multi Configuration Time Dependent Hartree
MP2 Møller-Plesset 2
ncl non-classical
NOP Natural Orbital Population
PCM Polarizable Continuum Model
PES Potential Energy Surface
PIC Phenylisocyanate
SIL Short-Iterative Lanczos
SPF(s) Single Particle Function(s)
TDI 2,4-Toluene-DiIsocyanate
TDSE Time Dependent Schrödinger Equation
TISE Time Independent Schrödinger Equation

Abstract

The main subjects of this work are the ultrafast laser-driven quantum dynamics of collective CO vibrations in a metal-dicarbonyl complex and the alcoholysis reaction of isocyanates.

Metal-carbonyl complexes play important roles in physiological and catalytic processes. The present goal is to obtain a fundamental insight into the interactions responsible for bond dissociation by using shaped laser pulses to steer molecular quantum dynamics. Specifically, *CpCo(CO)$_2$* is studied on the basis of a four-dimensional reactive potential energy surface, containing the two carbonyl vibrations as well as the respective metal-carbonyl bond dissociation coordinates. Potential and dipole moment surfaces are obtained using density functional theory with the B3LYP functional and the LanL2DZ basis set. The time-dependent Schrödinger equation is solved employing the multiconfiguration time-dependent Hartree method. It is shown that two perpendicularly polarized IR laser pulses can be used to trigger an excitation of the delocalized CO stretching modes, which corresponds to an alternating localization of the vibration within one CO bond. The switching time for localization in either of the two bonds is determined by the energy gap between the symmetric and antisymmetric fundamental transition frequencies. The phase of the oscillations between the two local bond excitations can be tuned by the relative phase of the two pulses. The extent of control of bond localization is limited by the anharmonicity of the potential energy surfaces leading to wave packet dispersion. This prevents such a simple pulse scheme from being used for laser-driven bond breaking in the considered example.

Using density functional theory two alcoholysis reactions are investigated, i.e. phenylisocyanate with cyclohexanol (**I**) and 2,4-toluene-diisocyanate with chloralhydrate (**II**). Anharmonic frequency calculations are performed to identify reactants and products in IR absorption spectra. From the reaction barrier one observes that the activation energy for model **II** is E_{act}=32.2 kcal/mol in a gas phase. This is in a strong contrast with the experimental results. Reaction coordinates for reaction **II** are determined in order to see how the system is moving on the potential energy surface.

Zusammenfassung

Die Hauptaspekte der vorliegenden Arbeit sind die ultraschnelle lasergetriebene Quantendynamik der kollektiven CO-Vibration in Metaldicarbonylkomplexen und die Alkoholyse von Isocyanaten.

Metalcarbonylkomplexe sind von großer Bedeutung in physiologischen und katalytischen Prozessen. Das Ziel ist, durch den Einsatz von geformten Laserpulsen die molekulare Quantendynamik zu steuern und somit einen fundamentalen Einblick in die für das Aufbrechen von Bindungen verantwortlichen Wechselwirkungen zu erhalten. Insbesondere wird $CpCo(CO)_2$ auf Basis einer 4-dimensionalen Potentialhyperfläche bestehend aus zwei Carbonylvibrationen und der jeweiligen Dissoziationskoordinate studiert. Die Hyperfläche von Energie und Dipolmoment werden mittels Dichtefunktionaltheorie mit dem B3LYP Funktional und dem LanL2DZ Basissatz berechnet. Die zeitabhängige Schrödingergleichung wird mit Hilfe der multiconfiguration time-dependent Hartree Methode gelöst. Es wird gezeigt, dass zwei senkrecht polarisierte Laserpulse eine Anregung der delokalisierten CO-Streckschwingungsmode auslösen, welche einer abwechselnden Lokalisierung der Vibration in einer CO-Bindung entspricht. Die übergangszeit für die Lokalisierung auf jeweils einer der beiden Bindungen wird durch den Energieabstand zwischen den symmetrischen und antisymmetrischen fundamentalen Übergangsfrequenzen bestimmt. Die Phase der Oszillationen zwischen den zwei lokalen Bindungsanregungen kann über die relative Phase der Laserpulse eingestellt werden. Das Ausmaß der Kontrolle der Lokalisierung ist durch die Anharmonizität der Potentialhyperfläche eingeschränkt, die zu einer Dispersion der Wellenpackete führt. Dies verhindert die Verwendung eines so einfachen Pulseschemas, um im betrachteten Beispiel Bindungen lasergetrieben zu brechen.

Unter Benutzung von Dichtefunktionaltheorie werden zwei Alkoholysereaktionen, Phenylisocyanat mit Cyclohexanol (**I**) und 2,4-Toluol-Diisocyanat mit Chloralhydrat (**II**), untersucht. Anharmonische Frequenzen werden berechnet um Reaktand und Produkt an Hand von IR Absorbtionsspektren zu identifizieren. Aus der Reaktionsbarriere wird die Aktivierungsenergie innerhalb des Models **II** mit E_{act}=32 kcal/mol in der Gasphase abgelesen. Dieses Resultat steht in starkem Kontrast zu experimentellen Resultaten. Die Reaktionskoordinaten der Reaktion **II** werden bestimmt um zu sehen wie sich das System auf der potentiellen Energieoberfläche bewegt.

Chapter 1

Introduction

Quantum control is a fascinating area of research in modern Physics [1–3]. The development of femtosecond infrared (IR) laser sources and pulse shapers give the possibilities for studying processes that occur on ultrafast time scales, such as molecular vibrations, bond breaking or nanopolymerization. Understanding the dynamics of chemical reactions paved the way for controlling the molecular processes. Often, the main goal is to get a desired product from the existing reactants. Traditionally, thermochemical techniques have been used, such as to control pressure (p) and temperature (T) in order to manipulate the rate constant k(p,T). Catalysis is a way to accelerate the chemical processes and the catalyst itself is a special substance that increases the rate of reaction. The invention of lasers opened a way to intensify a proper product yield selectively.

Many different strategies for laser control have been invented through the years [1]. One of them is the so-called *two-pathway quantum interference*. The quantum interference is created between two reaction pathways by two monochromatic laser beams with the same frequencies and tunable phases and intensities. It can be used i.e. for controlling the energy and angular distributions of photoionized electrons [4] and photodissociation products in bound-to-continuum transitions [5]. Another method is the so-called *pump-dump control* [6]. By using two sequential femtosecond laser pulses, with a tunable time delay between them, it is possible to selectively control intramolecular processes. First, a 'pump' pulse creates a wave packet on the excited potential energy surface (PES) and then it evolves freely until second, a 'dump' pulse transfers some part of the population back to the ground PES into the required reaction channel. One more method, is the so-called *optimal control theory* [7]. The tailored laser pulse is systematically shaped in order to steer the wave packet from the ground state to the desired target state. Additionally, *linearly chirped pulses* may be used for controlling atomic and molecular processes, i.e. population transfer between atomic states [8] or molecular vibrational levels [9], via 'ladder-climbing' mechanism and electronic excitation in molecules [10]. By using tailored laser pulses it became possible to explore the

potential energy surface and control the dynamics of the wave packets. For example, the vibrational ladder climbing mechanism is adapted to the anharmonicity of the PES, what is presented in Fig. 1.1.

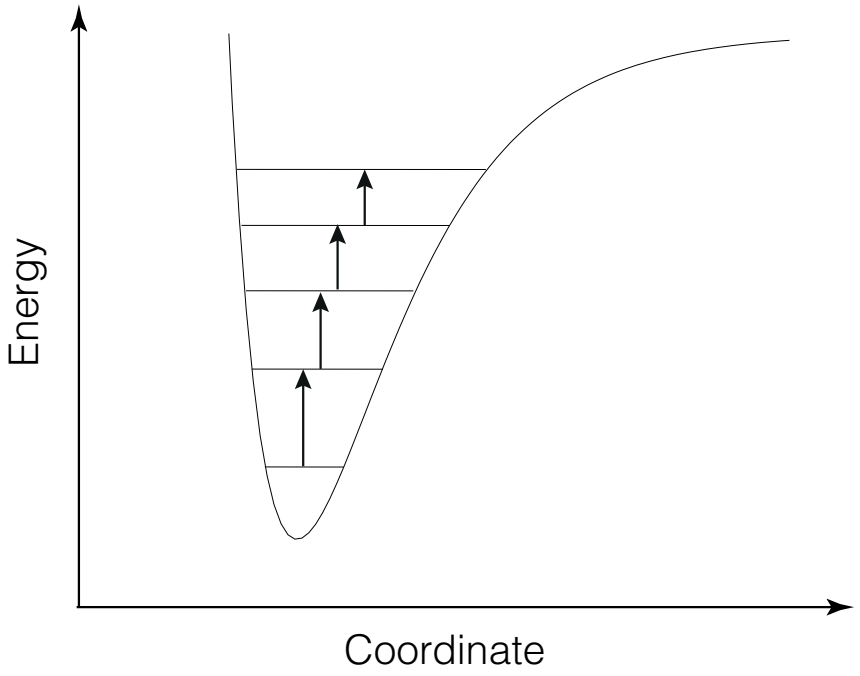

Figure 1.1: Vibrational ladder climbing for anharmonic Morse potential.

In this thesis, the cyclopentadienyl cobalt dicarbonyl model system, $CpCo(CO)_2$, presented in Ch. 3, will be investigated. Especially, the metal-carbonyl bond will be considered and relevant laser control schemes for selective bond excitation will be studied in the context of a possible dissociation process.

Another topic presented in the dissertation is the alcoholysis reaction of isocyanates discussed in Ch. 4. The prerequisites for the nanopolymerization process that is triggered by the ultrashort laser pulses is to find the reaction coordinates and to identify reactants and products. The intrinsic reaction coordinate (IRC) path connects a transition state with reactants and a product. The Arrhenius activation energies, as well as the harmonic and anharmonic IR absorption spectra are calculated.

1.1 Metal-Dicarbonyl System

Collective vibrations of equal functional groups are a frequent phenomenon in symmetric molecules. They lead to distinct features in IR absorption and Raman spectra according to the respective selection rules. While traditional IR spectroscopy had been focused on identifying species or establishing the correlation with structural motifs, ultrafast laser spectroscopy and pulse shaping techniques provide direct access to a broader

range of the PES, covering its anharmonicity as well as bond-breaking channels. For instance, anharmonic couplings between collective normal modes can be studied in quite some detail using ultrafast two-dimensional IR spectroscopy. Taking metal-carbonyl compounds as an example, anharmonic couplings [11] and spectral diffusion [12] have been studied for $Mn_2(CO)_{10}$.

Tailoring laser pulses such as to selectively break bonds has been a goal of laser-assisted reaction control for many years [13–15]. Although there is a considerable number of theoretical studies, experimental realizations are scarce. A pre-requisite for IR selective bond-breaking is mode-specific vibrational ladder climbing. Here, chirped pulse excitation was shown to enhance ladder-climbing efficiency since the pulse frequency is adjusted instantaneously to the decreasing vibrational level spacing [16]. This has been demonstrated for a number of relatively small molecules in Refs. [17–20]. With the development of flexible mid-IR pulse shapers based on acousto-optic modulators [21], it became possible to control specific populations beyond what can be achieved with simple linearly chirped pulses [22]. This was demonstrated for the collective CO vibrations in $W(CO)_6$. An extension, now including polarization shaping, was later shown to be able to discriminate between excitation of different carbonyl-stetching modes in $MnBr(CO)_5$ [23]. Phase shaping laser control of coherent superposition states corresponding to two different CO vibrations was demonstrated by Ashihara et al. for an iridium dicarbonyl complex in solution [24]. Pushing vibrational ladder climbing towards reaction control it was shown experimentally that rather high excitation levels can be reached enabling bond breaking mediated by intramolecular vibrational energy redistribution (IVR) [19] or by direct excitation of the reaction coordinate [20].

Due to their relevance for many chemical and biological processes, breaking metal-carbonyl bonds with laser light is a particular interesting target. Carboxymyoglobin or -hemoglobin are among those systems, which attracted the most interest in this respect. Although there is only a single CO group, proposed mechanisms and challenges are characteristic for control of this type of bond motion. In particular, current laser sources only enable for an efficient excitation of the CO vibration. Hence, ultrafast metal-carbonyl bond-breaking can only occur as a consequence of anharmonic coupling between the metal-carbon and the carbon-oxygen bond. Joffre et al. [25] have been the first to demonstrate coherent vibrational ladder climbing in a protein, exciting the anharmonic CO oscillator up to the $\nu = 6$ level. Even though the energy of this level ($\sim$12 700 cm^{-1}) is well above the threshold for Fe-CO bond-breaking ($\sim$6000-7500 cm^{-1}), no reaction products could be observed. In order to understand this behavior, an all Cartesian reaction surface model had been developed in Ref. [26]. Based on this model and using the multi-configuration time-dependent Hartree (MCTDH) method [27], wave packet simulations have been performed, mimicking CO stretch

vibrational excitation above the Fe-CO bond dissociation threshold. Here, it was found that the wave packet stays localized in the CO-stretch coordinate up to 1.5 ps, which points to lacking anharmonic coupling to the Fe-CO center of mass motion. The same conclusion was reached in [28] based on the analysis of simulations taking into account the chirped pulse explicitly for the model of Ref. [26] and using $MnBr(CO)_5$ as a mimic in Ref. [29]. Vibrational ladder climbing in carboxyhemoglobin was also addressed by Meier and co-workers [30–33]. In Ref. [30] local control theory (for a review, see Ref. [31]) was applied to a two-dimensional non-reactive model to show that upon extending the pulse duration, the predicted pulse shape changes from a simple chirp to a multiple sweep form, composed of several chirped pulses. This model was later supplemented by the effect of the fluctuating protein environment on the excitation efficiency of the CO-stretching mode [32, 33]. Note that control theory has also been used in a proof of principle study of metal-CO bond dissociation in $HCo(CO)_4$ by *direct* excitation of the metal-carbonyl bond [34]. Further studies on this molecule focused on the competitive Co-H vs. Co-CO bond breaking [35–37].

Viewed in the context of laser control of molecular dynamics, the collective nature of the CO normal mode vibrations in cases of multiple CO groups introduces even another challenge, i.e. the energy is not deposited into a *single* bond, but spread over *many* bonds within the molecule. This can be expected to make non-statistical bond breaking impossible. Therefore, a pre-requisite for selective metal-carbonyl bond-breaking in compounds with multiple CO groups would be a localization of the vibration along a single CO bond. Whether this can be achieved using femtosecond IR laser pulses is one of the main topic of this thesis. Previously, the manipulation of the collective CO vibrations by circularly-polarized laser pulses was studied for $Mn_2(CO)_{10}$ [38]. In that work vibrational excitation circles around the molecular axis. The topic is expanded in the present study on the effect of localization of vibrational motion, achieved by two perpendicularly-polarized laser pulses.

1.2 Monitoring the Alcoholysis of Isocyanates

Polymerization, polycondensation, and polyaddition reactions are used to manufacture materials having a wide range of properties. A common procedure employs thermally generated radicals in the electronic ground state, which act as triggers for the reactions. An alternative photochemical route involves photopolymers, capable of forming three-dimensional nanostructures upon ultrafast laser excitation [39]. Interestingly, despite its significance, little is known about the molecular details of the polymerization reaction

dynamics, both in theory and experiment. Considering isocyanate compounds as an example there is a host of physico-chemical investigations (for a review, see Ref. [40]). The general reaction scheme for alcoholysis of isocyanate to urethane is summarized in Fig. 1.2. It is commonly accepted that the addition occurs preferentially at the C=N group, i.e. according to a concerted reaction mechanism as opposed to a step-wise addition via an enol intermediate at the C=O group.

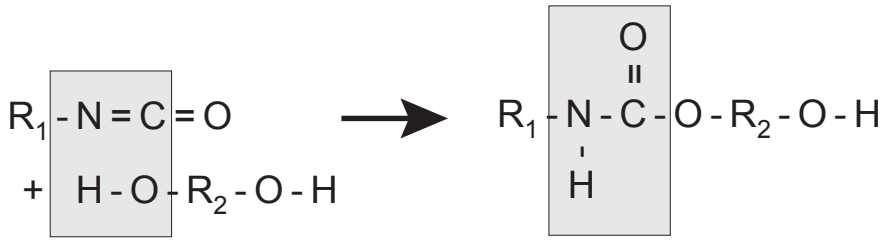

Figure 1.2: Reaction scheme for alcoholysis of isocyanates. In the present case we have for reaction **I** R_1 = phenylisocyanate, R_2 = cyclohexanol and for reaction **II** R_1 = 2,4-toluene-diisocyanate, R_2 = chloralhydrate.

The present study was triggered by recent experiments on ultrafast laser-induced non-photochemical nanopolymerization [41]. Experimental results were obtained by the group of Prof. K. Heyne. In these experiments a focused ultrafast mid-infrared laser pulse was used to initiate a localized polymerization reaction between 2,4-toluene-diisocyanate (TDI) and chloralhydrate in solution. By direct vibrational excitation of the putative reaction coordinate or vibrations coupled to the reaction coordinate the otherwise thermally-driven reaction was modified. Beyond heating, vibrational excitation can only affect hydrogen bonded educts, since vibrational lifetimes are typically in the range of picoseconds in solution at room temperature [42–45]. Thus, in order to understand the reaction dynamics towards urethane formation the initial reaction steps have to be studied.

1.3 Goals and Structure of This Work

In this section the main goals of this work are sketched and the structure is outlined. The first target is to investigate the laser-driven wave packet dynamics for the $CpCo(CO)_2$ molecular system. To this end, a four-dimensional model surface is created by applying quantum chemical calculations. Then, the quantum dynamic is performed using the MCTDH method. Next goal, is to explore the possibility of bond breaking i.e by using linearly polarized light. Another target is to find the way to control local oscillations

of a collective CO vibrations. Additionally, the system is exposed to artificial initial conditions to explore the PES and the goal is to observe whether dissociation is possible.

In a second study, the goal is to monitor the alcoholysis reaction of isocyanates. It is done by using infrared spectroscopy together with anharmonic frequency calculations that employ density functional theory. Another aim is the calculation of the Arrhenius activation energy and comparison with experimental results. Moreover, the goal is to find the relevant reaction coordinates to see how the system moves on the PES and what are the reaction barriers.

Following, the structure of this work is summarized. In Ch. 2 the theoretical background of the subject is explained. Specifically, in Sec. 2.2 the quantum chemistry and in Sec. 2.3 quantum dynamics are described. The laser-driven quantum dynamics is clarified in Sec. 2.4.

In Ch. 3 the results for Metal-Dicarbonyl system are presented. Mainly, in Sec. 3.3 the four-dimensional (4D) PES and dipole moment surface (DMS) are presented. In Sec. 3.5 the absorption spectra for the model are given. Results for linearly polarized light are shown in Secs. 3.6. The localization of collective CO vibrations is discussed in Sec. 3.7. The simulation for instantaneous displacement is presented in Sec. 3.8.

In Ch. 4 the results for alcoholysis reaction of isocyanates are shown. Specifically, in Sec. 4.2 the IR spectroscopy and reaction rates are presented for equilibrium structures and Arrhenius activation energies are calculated. In Sec. 4.3 the reaction coordinate path is shown and the reaction barriers are analyzed.

Finally, the Summary and Outlook are presented in Ch. 5.

Chapter 2

Theoretical Background

2.1 Overview

In this chapter the theoretical view of the subject will be presented. Central to quantum control simulations is the laser-driven wave packet dynamics. To prepare the prerequisites one needs to solve time-independent Schrödinger equation (TISE). This is refered to as the so-called quantum chemistry part, presented in Sec. 2.2. Solutions of the TISE are obtained by using the density functional theory (DFT) method. PES acquired in this way are defined on a special grid, such as the so-called Discrete Variable Representation (DVR) or Fast Fourier Transform (FFT) grid.

After quantum chemistry calculations are completed and the model is prepared, one can start the quantum dynamics simulations. Here, the time-dependent Schrödinger equation (TDSE) has to be solved. In this work, the MCTDH method, described in Sec. 2.3, will be used for that purpose.

The laser-matter interaction renders the Hamiltonian to become time-dependent. Different schemes of laser control, i.e. the determination of appropriate electric fields, are discussed in Sec. 2.4.

2.2 Quantum Chemistry

2.2.1 Stationary Molecular Schrödinger Equation

Quantum chemical computations are done by solving TISE

$$H_{mol}\Psi(\{\vec{r}_{N_{el}}\};\{\vec{R}_{N_{nuc}}\}) = \epsilon\Psi(\{\vec{r}_{N_{el}}\};\{\vec{R}_{N_{nuc}}\}). \tag{2.1}$$

Here, $\{\vec{r}_{N_{el}}\}$ is the set of electronic Cartesian coordinates and $\{\vec{R}_{N_{nuc}}\}$ is the set of nuclear Cartesian coordinates. The solutions of TISE give us an energy spectrum

ϵ_λ with corresponding eigenfunctions $\Psi_\lambda(\{\vec{r}_{N_{el}}\};\{\vec{R}_{N_{nuc}}\})$. The *ground state* is the energetically lowest eigenstate ϵ_0. The notation is simplified by setting $\{\vec{r}_{N_{el}}\} = r$ and $\{\vec{R}_{N_{nuc}}\} = \{R_{3N_{nuc}}\} = R$.

The molecular Hamiltonian operator H_{mol} for the molecule composed of N_{nuc} atoms having atomic numbers $Z_1, \ldots, Z_{N_{nuc}}$ with M_n being the mass, $\vec{P}_n$ the momentum operator and $\vec{R}_n$ the Cartesian coordinates of nth nuclei, surrounded by N_{el} electrons with momentum operator $\vec{p}_j$ and Cartesian coordinates $\vec{r}_j$ for jth electron has the form

$$H_{mol} = T_{el} + V_{el-nuc} + V_{el-el} + T_{nuc} + V_{nuc-nuc}, \tag{2.2}$$

where the kinetic energy operator of the electrons is given by

$$T_{el} = \sum_{j=1}^{N_{el}} \frac{\vec{p}_j^2}{2} = -\frac{1}{2}\sum_{j=1}^{N_{el}} \nabla_j^2, \tag{2.3}$$

the Laplacian operator ∇_i^2 is defined as

$$\nabla_i^2 = \frac{\partial^2}{\partial x_i^2} + \frac{\partial^2}{\partial y_i^2} + \frac{\partial^2}{\partial z_i^2}. \tag{2.4}$$

The kinetic energy operator for the nuclei is

$$T_{nuc} = \sum_{n=1}^{N_{nuc}} \frac{\vec{P}_n^2}{2M_n} = -\frac{1}{2}\sum_{n=1}^{N_{nuc}} \frac{\nabla_n^2}{M_n}. \tag{2.5}$$

The electron-electron repulsive Coulomb interaction is

$$V_{el-el} = \sum_{i<j}^{N_{el}} \frac{1}{r_{ij}}, \tag{2.6}$$

where r_{ij} is the distance between particle i and j, i.e. $r_{ij} = |\vec{r}_i - \vec{r}_j|$ and for the repulsive nuclear-nuclear Coulomb interaction one has

$$V_{nuc-nuc} = \sum_{m<n}^{N_{nuc}} \frac{Z_m Z_n}{R_{mn}}, \tag{2.7}$$

where $R_{mn} = |\vec{R}_m - \vec{R}_n|$. The attractive nuclear-electron Coulomb interaction is

$$V_{el-nuc} = -\sum_{m,i}^{N_{nuc},N_{el}} \frac{Z_m}{r_{mi}}, \tag{2.8}$$

where $r_{mi} = |\vec{R}_m - \vec{r}_i|$. Here and throughout this text, the system of atomic units is used. Constants such as mass of the electron, m_{el}, modulus of electron charge, $|e|$, reduced Planck constant, $\hbar = h/2\pi$, and vacuum permittivity, $4\pi\varepsilon_0$, are all set equal to unity and, therefore, have been dropped from equations.

To solve this equation one applies the Born-Oppenheimer approximation. At the beginning, the nuclear and electronic motion is separated, which is possible due to the large mass difference between these particles ($m_{el}/M_n < 10^{-3}$), i.e. electrons move much faster than the nuclei. The electronic configuration of the system will respond instantaneously to any changes in the nuclei positions and these changes will not cause any transitions between electronic states. In Born-Oppenheimer approximation, the so-called *nonadiabatic* operator is neglected (for details see Ref. [46]). Then the total molecular wave function can be separated into electronic and nuclear part

$$\Psi(r;R) \approx \Psi_{el}(r;R)\Psi_{nuc}(R). \tag{2.9}$$

Here, the nuclear wave function, $\Psi_{nuc}(R)$, depends on the position of the nuclei, and the electronic wave function, $\Psi_{el}(r;R)$, depends on electronic coordinates r and parametrically on nuclear coordinates R. The electronic wave function is the solution of a stationary Schrödinger equation describing the electronic state for static nuclei, where nuclear-nuclear repulsion is a constant

$$H_{el}(R)\Psi_{el}(r;R) = E_{el}(R)\Psi_{el}(r;R). \tag{2.10}$$

Here, the electronic Hamiltonian, which depends on the nuclear coordinates, is defined as

$$H_{el}(R) = T_{el} + V_{el-nuc} + V_{el-el}. \tag{2.11}$$

Within the Born-Oppenheimer approximation the function, which describes the potential for nuclear motion is called PES. It is given by

$$V(R) = E_{el}(R) + V_{nuc-nuc}(R). \tag{2.12}$$

The nuclear Schrödinger equation can then be written as

$$H_{nuc}\Psi_{nuc}(R) = \epsilon\Psi_{nuc}(R), \tag{2.13}$$

where the nuclear Hamiltonian operator for the electronic state *'el'* is expressed as

$$H_{nuc} = T_{nuc} + E_{el}(R) + V_{nuc-nuc}(R) = T_{nuc} + V(R). \tag{2.14}$$

In Eq (2.13) the energy ϵ presents the total energy of the molecule. At the first step we will need to obtain $V(R)$ by solving the electronic Schrödinger equation with the DFT method desribed in Sec. 2.2.2. Subsequently, we will focus on the time-dependent perspective to solve the nuclear Schrödinger equation as described in Sec. 2.3.

2.2.2 Solution of Electronic Schrödinger Equation

To solve time-independent electronic Schrödinger equation one can use DFT. This method is founded on two theorems given by P. Hohenberg and W. Kohn in 1964 [47]. During recent years DFT has become a powerful tool for solving the stationary electronic Schrödinger equation. For a detailed description see [48].

Electron density

The key quantity of DFT is the electron density. It is defined as follows:

$$\rho(r_1) = N \int \cdots \int |\Psi(x_1, x_2, \ldots, x_N)|^2 ds_1 dx_2 \ldots dx_N, \tag{2.15}$$

here one needs to integrate over all spin coordinates, s, and over $N-1$ spatial coordinates ($x = r, s$), keeping in mind that r and therefore x are vectors. The electron density $\rho(r_1)$ gives the probability of finding any of the N electrons inside the volume element dr_1 with arbitrary spin. The remaining $N-1$ electrons have arbitrary spin and arbitrary position. The state of the system is represented by a wavefunction, that is equal to the electronic wavefunction from the previous subsection $\Psi = \Psi_{el}$. Electron density vanishes at infinity for spatial variables and gives the total number of electrons, N, by integrating over dr_1

$$\rho(r \to \infty) = 0, \tag{2.16}$$

$$\int \rho(r_1) dr_1 = N. \tag{2.17}$$

Hohenberg - Kohn theorem

The N-electron wavefunction $|\Psi(x_1, x_2, \ldots, x_N)|^2$ with $3N$ spatial and N spin variables can be replaced by a simpler function such as the electron density $\rho(r)$. The first Hohenberg-Kohn theorem states that there cannot be two different external potentials (V_{ext}, V'_{ext}) that yield to the same ground state electron density. The ground state energy E_0 for the ground state electron density is expressed as follows:

$$E_0[\rho_0] = E_{Ne}[\rho_0] + T[\rho_0] + E_{ee}[\rho_0] = E_{Ne}[\rho_0] + F_{HK}[\rho_0], \tag{2.18}$$

where $E_{Ne}[\rho_0]$ is the potential energy due to nuclei-electron attraction and $F_{HK}[\rho_0]$ is the Hohenberg-Kohn functional constructed of the kinetic energy for the electrons $T[\rho_0]$ and the potential energy due to electron-electron repulsion $E_{ee}[\rho_0]$. From this term one can extract classical Coulomb part $J[\rho]$

$$E_{ee}[\rho] = \frac{1}{2}\int\int \frac{\rho(r_1)\rho(r_2)}{r_{12}} dr_1 dr_2 + E_{ncl}[\rho] = J[\rho] + E_{ncl}[\rho] \tag{2.19}$$

and the remaining $E_{ncl}[\rho]$ gives the non-classical contribution to the electron-electron interactions. In this term one has the self-interaction correction, as well as exchange and Coulomb correlation effects.

The Schrödinger equation could be solved exactly, if the Hohenberg-Kohn functional were known exactly. Since this is not the case, one needs to search for the suitable functionals, $T[\rho]$ and $E_{ncl}[\rho]$, that can be used for the system in which one is interested.

The second Hohenberg-Kohn theorem is based on the variational principle. It states that the Hohenberg-Kohn functional $F_{HK}[\rho]$ gives the ground state energy E_0 of the system if and only if the input density is the true ground state density ρ_0

$$\langle\Psi|\hat{H}|\Psi\rangle = E[\rho] \geq E_0[\rho_0] = \langle\Psi_0|\hat{H}|\Psi_0\rangle. \tag{2.20}$$

Kohn-Sham equations

The second breaktrough paper of DFT written by Kohn and Sham appeared in 1965 [49]. They showed how to turn the equation (2.18) into a practical scheme for computation. They developed the so-called "Kohn-Sham equations", which also gives a method to determine the kinetic energy by considering a non-interacting reference system and how to treat the non-classical contributions to the electron-electron repulsion.

The kinetic energy of a non-interacting system is expressed as

$$T_S = -\frac{1}{2}\sum_{i}^{N_{el}} \langle\varphi_i|\nabla^2|\varphi_i\rangle. \tag{2.21}$$

Because the non-interacting kinetic energy is not equal to the true kinetic energy the following separation of the functional $F[\rho]$ is introduced

$$F[\rho(r)] = T_S[\rho(r)] + J[\rho(r)] + E_{XC}[\rho(r)], \tag{2.22}$$

where $E_{XC}[\rho(r)]$, is the exchange-correlation functional

$$E_{XC}[\rho] \equiv (T[\rho] - T_S[\rho]) + (E_{ee}[\rho] - J[\rho]) = T_C[\rho] + E_{ncl}[\rho]. \tag{2.23}$$

The energy of the real, interacting system can now be written as follows:

$$\begin{aligned} E[\rho(r)] &= T_S[\rho(r)] + J[\rho(r)] + E_{XC}[\rho(r)] + E_{Ne}[\rho(r)] \\ &= T_S[\rho] + \frac{1}{2}\int\int \frac{\rho(r_1)\rho(r_2)}{r_{12}} dr_1 dr_2 + E_{XC}[\rho] + \int V_{Ne}\rho(r) dr \end{aligned} \tag{2.24}$$

The term $E_{XC}[\rho(r)]$ is still unknown and different functionals have been developed. In this study, the functional like B3LYP has been used (see below). To minimize this energy expression one needs to find the set of orbitals $\{\varphi_i\}$ such that the density equals exactly the ground state density

$$\rho_0(r) = \sum_i^{N_{el}} \sum_s |\varphi_i(r,s)|^2, \tag{2.25}$$

$\varphi_i(x_i)$ are spin orbitals, frequently called Kohn-Sham orbitals, made of spatial orbital $\phi(r)$ and one of spin functions $\alpha(s)$ or $\beta(s)$

$$\varphi(x) = \phi(r)\sigma(s), \;\; \sigma = \{\alpha, \beta\}. \tag{2.26}$$

In order to find spin orbitals, one solves the following so-called 'Kohn-Sham equations' (for details see [50]):

$$\left(-\frac{1}{2}\nabla^2 + \left[\int \frac{\rho(r_2)}{r_{12}} dr_2 + V_{XC}(r_1) - \sum_n^{N_{nuc}} \frac{Z_n}{r_{1n}} \right] \right) \varphi_i = \varepsilon_i \varphi_i \tag{2.27}$$

Potential V_{XC} is related to the exchange-correlation energy E_{XC} via

$$V_{XC} \equiv \frac{\delta E_{XC}[\rho]}{\delta \rho}. \tag{2.28}$$

All orbitals are combined in the Slater determinant Θ_S

$$\Theta_S = \frac{1}{\sqrt{N!}} \begin{vmatrix} \varphi_1(x_1) & \varphi_2(x_1) & \cdots & \varphi_N(x_1) \\ \varphi_1(x_2) & \varphi_2(x_2) & \cdots & \varphi_N(x_2) \\ \vdots & \vdots & \ddots & \vdots \\ \varphi_1(x_N) & \varphi_2(x_N) & \cdots & \varphi_N(x_N) \end{vmatrix}. \tag{2.29}$$

Exchange-Correlation Functionals

Since the exact exchange correlation energy E_{XC} is not known approximate functionals have been developed. One of them is the hybrid functional B3LYP suggested by Becke in 1993 [51]. It is considered an all-purpose functional with a good performance for an

organic reactions [48]. For study of metal-ligand bond breaking see [52]. It is made of Becke's 1988 exchange functional (B88 or B) [53] and Lee-Yang-Parr (LYP) correlation functional [54]. It is given by

$$E_{XC}^{B3LYP} = aE_X^{Slater} + (1-a)E_X^{HF} + b\Delta E_X^{B88} + cE_C^{LYP} + (1-c)E_C^{LSDA}. \tag{2.30}$$

Here, three semiempirical coefficients a, b and c are included. They were determined by fitting experimental data to DFT computations. This gave the constant values a=0.20, b=0.72 and c=0.81. LSDA is a local spin-density approximation and HF the exact Hartree-Fock exchange.

The functional described above is implemented in the Gaussian 09 package [55] and was used throughout this work.

Beyond DFT

At a large distance there is an attractive interaction due to the correlated electron motion. Thereby the two atoms mutually polarized each other. It has inverse 6th power dependence according to the distance between the atoms and it is called dispersion interaction [56]. In quantum chemistry it is used by adding an empirical correction to the overall potential [57].

The Møller Plesset perturbation theory, in contrast to DFT, is a wave function method. It was proposed by the C. Møller and M. S. Plesset in 1934 [58]. It provides a means to account for dynamical correlations between the electrons. The method is referred as to MPn, i.e. MP2, where number 2 indicates second order correction terms to the energy with respect to the Hartree-Fock reference.

Basis Sets

In order to perform quantum chemical computations within DFT theory, the basis set needs to be defined. Here, the linear combination of atomic orbitals - molecular orbitals *ansatz* was used. The molecular orbitals are formed as a superposition (or linear combination) of atomic orbitals

$$\phi_i(\vec{r}) = \sum_{\mu=1}^{n} c_{\mu i} g_\mu(\vec{r}), \tag{2.31}$$

here $\phi_i(\vec{r})$ is the i-th molecular orbital, $c_{\mu i}$ is the linear combination coefficient, $g_\mu(\vec{r})$ is the μ-th atomic orbital and n is the number of atomic orbitals. In accordance to have functions appropriate for fast calculation Gaussian Type Orbitals (GTOs) were

introduced. They are expressed as

$$g(\alpha, l, m, n; x, y, z) = Ne^{-\alpha r^2} x^l y^m z^n, \tag{2.32}$$

here N is a normalization constant, exponent α controls the extension of a basis function, x, y, z are the cartesian coordinates, l, m, n are integers and $r^2 = x^2 + y^2 + z^2$. GTOs are frequently called Gaussian primitives and for molecular calculations they have to be contracted to look like Slater Type Orbitals. For Pople's basis set one has $n-ijk$G, where n is the number of primitives for inner shell and $ijk-$ number of primitives for contractions in the valence shell. The valence electrons are more likely to form bonds than the inner (core) electrons. In the so-called split-valence basis set, like 6-31 or TZVP (triple zeta valence plus polarization [59,60]) more contractions are employed to characterized valence orbitals rather than the core orbitals. Valence orbitals do not get more primitives but they allocate more basis functions. For example, the 6-311G basis set has (12s,9p) primitives contracted to [6,5] basis functions with contraction scheme (631111,42111). It means that there are 6 s-type contractions (or basis functions) consisting of 6, 3, 1, 1, 1, 1 primitives (one is doubled), respectively, and the p-shell consists of 5 basis functions with 4, 2, 1, 1, 1 primitives, respectively [61]. For more examples see the Ref. [62].

By adding polarization functions, i.e. functions of higher angular momentum number (L), one can improve the basis set. These functions are added as uncontracted gaussians. For example, 6-31G(d,p) or 6-31G** means that a d-type gaussians are added to each heavy (non-hydrogen) atom and a p-type primitive gaussian to each hydrogen atom.

Another way to improve the basis set is to use diffuse functions. They are useful for the description of the electron density at large distance from the nuclei. For the Pople basis sets diffuse functions are represented by '+' or '++', i.e. 6-31+G or 6-311+G means that 1 diffuse s-type and p-type gaussian with the same exponents are added to the heavy atoms and 6-31++G or 6-311++G means that 1 diffuse s-type and p-type gaussian is added on heavy atoms and 1 diffuse s-type gaussian is added on hydrogen.

Another way to reduce the costs of computations is to use Effective Core Potentials (ECP). In this method the inner (core) orbitals are treated as an averaged potential (some modifications to the hamiltonian) rather than with explicit electrons. This is reasonable, because these orbitals are often not affected by chemical bonds. For the valence electrons the basis functions have to be provided. An example of this basis set is the Los Alamos ECP, LanL2DZ [63–65].

All quantum chemical calculations have been performed using Gaussian 09 package [55].

2.2.3 Potential Energy Surface

Born-Oppenheimer PES are required to study quantum dynamical processes. Since the procedure to obtain the $V(R)$ is described above, in the following one can illustrates some features of it (for details see [46,66]). First of all the gradient of the potential will be defined

$$\nabla V(R) = \{\partial V(R)/\partial R_1, \ldots, \partial V(R)/\partial R_{3N_{nuc}}\}, \tag{2.33}$$

whose negative describes the force acting on the atoms. One more important quantity is the $3N_{nuc} \times 3N_{nuc}$ force constant matrix or *Hessian matrix*. It is defined as the second derivative of the PES

$$k_{mn} = \frac{\partial^2 V(R)}{\partial R_m \partial R_n} \qquad (m, n = 1, \ldots, 3N_{nuc}). \tag{2.34}$$

The gradient of the potential disappear for the point which is called *stationary*

$$\nabla V(R) = 0. \tag{2.35}$$

In the vicinity of the *stationary* point the character of the potential energy surface can be explored. To this end one has to take a look at the eigenvalues of the Hessian matrix at this point. In general there will be $3N_{nuc}$ eigenvalues. Three of them correspond to translational motions and three of them to rotational motions, so six eigenvalues are equal to zero. The remaining $3N_{nuc} - 6$ eigenvalues and the related eigenvectors define the *normal modes* of vibrational motion. For the linear molecule there will be $3N_{nuc} - 5$ normal modes. If all of these eigenvalues are positive we are at the minimum of the potential energy surface. If one eigenvalue of the Hessian matrix is negative one is at the saddle point i.e. the transition state of the system. If two eigenvalues are negative one is at some second order saddle point of the surface, and so on.

To construct the surface one has to change the coordinates in a well-defined way. One method is to use internal coordinates. They are made up of bond lengths, bond angles or dihedral (torsion) angles. In this work, for the frozen equilibrium geometry we were simultaneously changing bond lengths for dissociation and vibration coordinates to construct a four-dimensional PES. For each single point the corresponding energy was calculated to generate the PES. Because other degrees of freedom, like bond or dihedral angles, are not changing at all there is no information about them in the PES. In this method we don't need to calculate forces or the Hessian matrix once a stationary point has been identified.

Another way is to use normal mode coordinates. They are made up of the *linear combination* of the Cartesian *displacements* for every atom. If one has a system with $3N_{nuc} - 6$ degrees of freedom, $Q = \{Q_1, \ldots, Q_{3N_{nuc}-6}\}$, then the PES would look like

this:

$$V(Q) = V^{(1)} + V^{(2)} + V^{(3)} + \cdots V^{(3N_{nuc}-6)}. \tag{2.36}$$

In this expression one has correlation expansion of the potential, where $V^{(1)}$ is *one-mode* potential for *uncoupled* modes

$$V^{(1)} = \sum_i V_i^{(1)}(Q_i). \tag{2.37}$$

$V^{(2)}$ is the *two-modes* potential for the two *coupled* modes (doesn't contain the separable part Eq. (2.37))

$$V^{(2)} = \sum_{i<j} V_{ij}^{(2)}(Q_i, Q_j). \tag{2.38}$$

The coupling between three modes symbolize by $V^{(3)}$ is expressed as follows:

$$V^{(3)} = \sum_{i<j<k} V_{ijk}^{(3)}(Q_i, Q_j, Q_k). \tag{2.39}$$

At the end the potential for the coupling between all of the normal modes in the system is $V^{(3N_{nuc}-6)}$.

2.3 Quantum Dynamics

When the electronic Schrödinger equation is finally solved and the PES is obtained, we can turn our interests to the quantum dynamics simulations. Throughout this work the time-dependent Schrödinger equation is solved using the MCTDH method. The introduction of MCTDH algorithm was presented in 1990 in the paper of H.-D. Meyer et al. [67]. They showed the general ansatz for the wavefunction as well as working equations for this procedure. It will be described in this section. For the detailed description about MCTDH as well as the overview of the predecessors of MCTDH such as time-dependent Hartree or multiconfiguration time-dependent self-consistent field see the Refs. [27, 68, 69].

2.3.1 *Ansatz* for the wave function

The MCTDH algorithm gives us the possibility to solve the TDSE. The ansatz for the wavefunction for a system of f degrees of freedom looks as follows:

$$\begin{aligned}\Psi(Q_1,\dots,Q_f,t) &= \sum_{j_1=1}^{n_1}\cdots\sum_{j_f=1}^{n_f} A_{j_1\cdots j_f}(t)\prod_{\kappa=1}^{f}\varphi_{j_\kappa}^{(\kappa)}(Q_\kappa,t)\\ &= \sum_{J} A_J\Phi_J,\end{aligned} \tag{2.40}$$

here $Q_1,\dots,Q_f$ are the nuclear coordinates, the $A_{j_1\cdots j_f}(t)$ are time-dependent expansion coefficients and the $\varphi_{j_\kappa}^{(\kappa)}$ are time-dependent basis functions, known as *single-mode* single-particle functions (SPFs). The form of the equations is simplified by setting up the composite index J

$$\begin{aligned}A_J &= A_{j_1\cdots j_f}\\ \Phi_J &= \prod_{\kappa}^{f}\varphi_{j_\kappa}^{(\kappa)}.\end{aligned} \tag{2.41}$$

The *multiconfiguration* wavefunction for p "particles" may be expressed as follows:

$$\Psi(q_1,\dots,q_p,t) = \sum_{j_1=1}^{\tilde{n}_1}\cdots\sum_{j_p=1}^{\tilde{n}_p} A_{j_1\cdots j_p}(t)\prod_{\kappa=1}^{p}\varphi_{j_\kappa}^{(\kappa)}(q_\kappa,t), \tag{2.42}$$

here $q_\kappa = (Q_i, Q_j, \dots)$ denotes the set of coordinates *combined* in a single particle and $\varphi_{j_\kappa}^{(\kappa)}$ are called *multimode* single-particle functions. Combined modes were used in this work to speed up the calculations. The modes that were combined were strongly correlated.

Single-particle functions are represented as a *linear combinations* of so-called *primitive basis functions*

$$\varphi_{j_\kappa}^{(\kappa)}(Q_\kappa,t) = \sum_{i_\kappa=1}^{N_\kappa} c_{i_\kappa j_\kappa}^{(\kappa)}(t)\chi_{i_\kappa}^{(\kappa)}(Q_\kappa), \tag{2.43}$$

here the index N_κ represents the number of the grid points. By setting $n_\kappa = N_\kappa$ in Eq. 2.40 we can achieve the expansion of the wavefunction, that corresponds to the *ansatz* for the standard method.

2.3.2 Grid Representation

For calculation matrix elements of the Hamiltonian the DVR method is used [70]. To this end the following procedure is applied:
(i) Matrix representation of the $\hat{x}$ position operator in a truncated basis of N orthogonal

polynomials, $\mathbf{x}_\mathrm{N}$, is constructed.
(ii) $\mathbf{X}_\mathrm{N}$ is diagonalized by a unitary transformation

$$\mathbf{U}^\dagger \mathbf{X}_N \mathbf{U} = \mathbf{x}, \tag{2.44}$$

where $(\mathbf{x})_{ij} = x_i \delta_{ij}$.
(iii) The diagonal matrix of potential energy V($\mathbf{x}$) is computed.
(iv) The kinetic energy matrix elements, $\mathbf{T}_N$, in the basis of orthogonal polynomials are calculated. They are usually known analytically.
(v) The DVR Hamiltonian is created by adding kinetic and potential energies

$$\mathbf{H}_N^{DVR} = \mathbf{T}_N^{DVR} + \mathbf{V}_N^{DVR}. \tag{2.45}$$

For the coordinates that describe vibrational motion the *harmonic oscillator* (HO DVR) orthogonal basis functions are used, and they have the form of Hermite polynomials. For other types of coordinates, that describe dissociation motion, the FFT method is used. This is based on a plane waves on equally-spaced grid.

2.3.3 Equations of motion

To derive the equations of motion (EOMs) for the MCTDH ansatz in Eq. (2.40) the Dirac-Frenkel variational principle is applied [71, 72]:

$$\langle \delta\Psi | H - i\partial_t | \Psi \rangle = 0, \tag{2.46}$$

here ∂_t is the partial derivative with respect to time and δ is a small variation for the wavefunction. Then the EOMs for the A-vector and φ-vector take the form

$$i\dot{A}_J = \sum_L \langle \Phi_J | H | \Phi_L \rangle A_L, \tag{2.47}$$

$$i\dot{\vec{\varphi}}^{(\kappa)} = (1 - P^{(\kappa)})(\boldsymbol{\rho}^{(\kappa)})^{-1} \langle \boldsymbol{H} \rangle^{(\kappa)} \vec{\varphi}^{(\kappa)}. \tag{2.48}$$

Here, single particle functions are represented by a vector $\vec{\varphi}^{(\kappa)} = (\varphi_1^{(\kappa)}, \ldots, \varphi_{n_\kappa}^{(\kappa)})^T$, $P^{(\kappa)}$ is the projection operator, $P^{(\kappa)} = \sum_{j=1}^{n_\kappa} |\varphi_j^{(\kappa)}\rangle\langle\varphi_j^{(\kappa)}|$. The $\langle \boldsymbol{H} \rangle^{(\kappa)}$ is the *mean-field* operator, whose matrix elements are defined as follows: $\langle H \rangle_{jl}^{(\kappa)} = \langle \Psi_j^{(\kappa)} | H | \Psi_l^{(\kappa)} \rangle$. Here $\Psi_l^{(\kappa)}$ are *single-hole functions* that are expressed as the linear combination of Hartree products of $(f-1)$ single particle functions (and do not include single-particle functions for Q_κ coordinate). $\boldsymbol{\rho}^{(\kappa)}$ is the density matrix and can be written as $\rho_{jl}^{(\kappa)} = \langle \Psi_j^{(\kappa)} | \Psi_l^{(\kappa)} \rangle$. More details about the equations of motion can be found in Ref. [27].

The integration scheme used for solving the MCTDH equations of motion is called

constant mean-field (CMF) integrator [73]. The concept of this method is that the matrix elements $H_{JL} = \langle \Phi_J | H | \Phi_L \rangle$ and the product of the inverse density and mean-field matrices $(\boldsymbol{\rho}^{(\kappa)})^{-1} \langle \boldsymbol{H} \rangle^{(\kappa)}$ are changing much slower in time than the MCTDH coefficients and single-particle functions. That is why for the former quantities the time step for the propagation can be larger than for the latter one. In the sense the former quantities are kept constant for some time t. Working equations for A-vector can be solved using special integrators like Chebyshev [74] or short iterative Lanczos (SIL) [75] implemented in [76]. The set of equations for the single-particle functions are non-linear because of the projection operator $P^{(\kappa)}$. To solve this equations one can use the Bulirsch-Stoer (BS) extrapolation method.

The convergence in MCTDH is checked by monitoring the Natural Orbital Population (NOP) [27].

2.3.4 Preparing the initial state

An important task is the generation of the initial wave packet. To generate a ground state wave packet one can use the procedure of energy relaxation [77]. In this method the wave packet is propagated in the negative imaginary time $t = -i\tau$. So the wavepacket expanded in the set of eigenstates of time independent Hamiltonian H

$$\Psi(t) = \sum_j a_j e^{-iE_j t} \varphi_j, \tag{2.49}$$

will be replaced by

$$\Psi(\tau) = \sum_j a_j e^{-E_j \tau} \varphi_j. \tag{2.50}$$

Here, $H\varphi_j = E_j \varphi_j$ and $a_j = \langle \varphi_j | \Psi(0) \rangle$. The vibrational ground state will be obtained after relaxation of every excited eigenfunction to zero.

2.3.5 Product representation of the Hamiltonian

To have a better numerical performance of the integration of EOMs the Hamiltonian should be separated into two parts - one is operating only on one degree of freedom $h^{(\kappa)}$ (separable part) and the second one covers all correlations between degrees of freedom H_R (residual part)

$$H = \sum_{\kappa=1}^{f} h^{(\kappa)} + H_R. \tag{2.51}$$

After this step the EOMs in Eqs. 2.47 and 2.48 take the form

$$i\dot{A}_J = \sum_L \langle \Phi_J | H_R | \Phi_L \rangle A_L, \tag{2.52}$$

$$i\dot{\vec{\varphi}}^{(\kappa)} = h^{(\kappa)} \mathbf{1}_{n_\kappa} \vec{\varphi}^{(\kappa)} + (1 - P^{(\kappa)})(\boldsymbol{\rho}^{(\kappa)})^{-1} \langle \boldsymbol{H}_R \rangle^{(\kappa)} \vec{\varphi}^{(\kappa)}. \tag{2.53}$$

Here, the matrix elements $\langle \Phi_J | H_R | \Phi_L \rangle$ and the mean-fields $\langle \boldsymbol{H}_R \rangle^{(\kappa)}$ are now evaluated using only the residual part of the Hamiltonian.

Moreover, for the efficiency of the algorithm the residual part of the Hamiltonian is expressed as the sum of the products for the single-particle operators

$$H_R = \sum_{r=1}^{s} c_r \prod_{\kappa=1}^{f} h_r^{(\kappa)}, \tag{2.54}$$

where c_r are the expansion coefficients. The kinetic energy operator usually has this form, but the potential energy operator needs to be fitted to the product form. To this end, we need to have the potential energy $V(Q_{i_1}^{(1)}, \ldots, Q_{i_f}^{(f)})$ on the product grid, where f denotes the number of degrees of freedom and $Q_{i_\kappa}^{(\kappa)}$ denotes the i_κth grid point for the κth one-dimensional grid, where $1 \leq i_\kappa \leq N_\kappa$. Then, we may build the eigenvectors $v_j^{(\kappa)}$ - with components $v_j^{(\kappa)}(Q_i^{(\kappa)})$ - and eigenvalues $\lambda_j^{(\kappa)}$ of the *potential density matrix*. They are called *natural potentials* and *natural potential populations*, respectively [27]. The potential can be approximated in the way

$$\begin{aligned} V(Q_{i_1}^{(1)}, \ldots, Q_{i_f}^{(f)}) &\approx V^{app}(Q_{i_1}^{(1)}, \ldots, Q_{i_f}^{(f)}) \\ &= \sum_{j_1=1}^{m_1} \cdots \sum_{j_1=1}^{m_f} C_{j_1 \ldots j_f} v_{j_1}^{(1)}(Q_{i_1}^{(1)}) \ldots v_{j_f}^{(f)}(Q_{i_f}^{(f)}), \end{aligned} \tag{2.55}$$

where $C_{j_1 \ldots j_f}$ are the expansion coefficients and $\{m_\kappa\}$ is the set of expansion orders. If the expansion orders and the number of grid points are equal, then the approximated potential and the exact potential are equal. It is possible to decrease the number of expansion terms in Eq. (2.55) by using the so-called *contraction over κth mode* procedure. To this end *contracted expansion functions* are used. Because the entire PES is not important for the observing processes, one can use the *separable weights* method to choose only the region that is relevant. Another way is to use the *non-separable weights* method, it means to use a function that will give the value between 0 and 1 for every point in the potential. The most important points will get the weight 1 and the less important points will get weight less than 1 or 0. It is also important to check the error convergence for the calculations. One way is to use the global $\mathcal{L}^2$-error Δ^2 to check the quality of the potential fit. For the separable weights one can

use the *weighted* $\mathcal{L}^2$-error Δ^w. One more way is to use the *weighted root-mean-square error* Δ^w_{rms}. For more details see Ref. [27]. To produce the fitted form of the potential, we use the prepared *ab initio* data of the PES in the *potfit* module of the MCTDH package [76].

2.4 Laser-Driven Wave Packet Dynamics

If the system interacts with a laser field, the time dependent Schrödinger equation has the form

$$i\partial_t|\Psi(t)\rangle = (H_{mol} + H_{field}(t))|\Psi(t)\rangle. \tag{2.56}$$

Here, H_{mol} is the molecular system Hamiltonian and $H_{field}(t)$ is time-dependent field Hamiltonian that introduces a perturbation to the molecular system. The molecular system Hamiltonian has been discussed before. The field Hamiltonian is defined in a so-called *dipole approximation*. It means that the electric field interacts with the electric dipole moment operator of the molecule

$$H_{field}(t) = -\vec{d}\vec{E}(t). \tag{2.57}$$

$\vec{E}(t)$ is the electric field that is defined as

$$\vec{E}(t) = \mathcal{E}(t)\vec{e}\cos(\omega t + \phi). \tag{2.58}$$

Here, ω is the angular frequency, ϕ is the phase, $\vec{e}$ defines the direction of the field and $\mathcal{E}(t)$ is the field envelope for which we will use a gaussian shape given by

$$\mathcal{E}(t) = E_0 \exp(-2\ln 2(t - t_0)^2/\tau^2). \tag{2.59}$$

Here, E_0 is the pulse amplitude, τ is the full width at half maximum (FWHM) and t_0 is the center of the pulse. Electric dipole moment is a vector and, in general, has three components, $\vec{d} = (d_x, d_y, d_z)$. Below we will use two different scenarios with relation to the polarization, assuming that the molecule is fixed in the laboratory frame. First, we will consider the linear polarization and the single pulse. Second, we will use two pulses that interact with two components of DMS

$$\vec{E}(t) = \sum_{i=1}^{2} \mathcal{E}(t)\vec{e}_i \cos(\omega_i t + \phi_i). \tag{2.60}$$

Here, the frequencies of the pulses may be different and i.e. be resonant with two distinct molecular vibrations. We will specify Eq. (2.60) to the perpendicularly polarized laser

pulses

$$\vec{E}(t) = \mathcal{E}(t)(\vec{e}_X \cos(\omega_X t + \phi_X) + \vec{e}_Y \cos(\omega_Y t + \phi_Y)) \,. \tag{2.61}$$

Here, the field envelope, $\mathcal{E}(t)$ is like in Eq. (2.59). The frequencies $\omega_{X,Y}$ and the phases $\phi_{X,Y}$ have different values for different polarization directions $\vec{e}_{X,Y}$. In fact, only the relative phase $\Delta\phi = \phi_Y - \phi_X$ will be of interest in the application.

The anharomonic IR absorption spectrum can be calculated in 2nd order perturbation theory from the *autocorrelation* function of the dipole. It is the overlap between the initial and the propagated wavefunction [27]

$$C(t) = \langle \tilde{\Psi}(0) | \tilde{\Psi}(t) \rangle. \tag{2.62}$$

The dipole moment operator, d_α, acts on the ground state wave function in such a way $\langle \Psi_0 | d_\alpha = \langle \tilde{\Psi}(0) |$. Vibrational spectrum is then computed by Fourier transform of $C(t)$

$$\alpha(\omega) \propto A_0 \omega \sum_{\alpha=x,y,z} Re \int_0^\infty dt e^{i\omega t} e^{-t/\tau} \langle \Psi_0 | d_\alpha e^{-iH_{mol}t} d_\alpha | \Psi_0 \rangle. \tag{2.63}$$

Here, A_0 is a normalization constant, and τ is a parameter responsible for the broadening of the spectrum.

Chapter 3

Laser-Driven Quantum Dynamics of Metal-Dicarbonyls

3.1 Overview

In this chapter, the dicarbonyl model system $CpCo(CO)_2$ will be investigated. The quantum chemical computations will be done at the DFT/ B3LYP/LanL2DZ level of theory in order to build 4D PES and DMS.

Harmonic and anharmonic IR absorption spectra will be obtained by normal mode analysis and quantum dynamics simulations, respectively. The latter is described in Sec. 2.4 and calculated according to Eq. (2.63).

Possibility of bond breaking will be investigated in Sec. 3.6, where linearly-polarized light induces symmetric or antisymmetric molecular vibrations. In Sec. 3.7 the possibility of inducing local bond oscillations will be studied by tuning the relative phase between two perpendicularly-polarized laser pulses. Moreover, in Sec. 3.8, the ground state wave packet will be initially displaced on the PES and propagated freely, i.e. without any laser field.

3.2 Model System

In order to explore the possibility of bond breaking we examine the dicarbonyl complex $CpCo(CO)_2$ (cyclopentadienyl cobalt dicarbonyl, $(C_5H_5)Co(CO)_2$), see Fig. 3.1. The Co-CO bond dissociation energy of this system is relatively low, which is why this complex has been chosen [26, 78]. Quantum chemical computations, described in Sec. 2.2, have been performed using DFT at the B3LYP/LanL2DZ level of theory as implemented in the Gaussian 09 program package [55]. Previously, with this level of theory CO ligated heme group was explored in Ref. [79]. The bond lengths for optimized

geometry in the equilibrium are 1.75 Å for Co-C(1,2) and 1.18 Å for C(1,2)-O(1,2), summarized in Table 3.1. This is in good agreement with electron diffraction data, 1.69 Å and 1.19 Å gave in Ref. [80]. It is assumed that the $Co(CO)_2$ fragment is in the X - Y frame and the X - axis bisecting the angle C1-Co-C2.

Bond	Distance Å	Exp. [80] Å
Co-C1	1.75	1.69
Co-C2	1.75	1.69
C1-O1	1.18	1.19
C2-O2	1.18	1.19
Co-C3	2.14	-
Co-C4	2.20	-
Co-C5	2.18	-
Co-Cp ring	1.79	-
Angle	Degree	
C1-Co-C2	95^o	

Table 3.1: Bonds, distances and angle between main atoms and experimental results for selected ones.

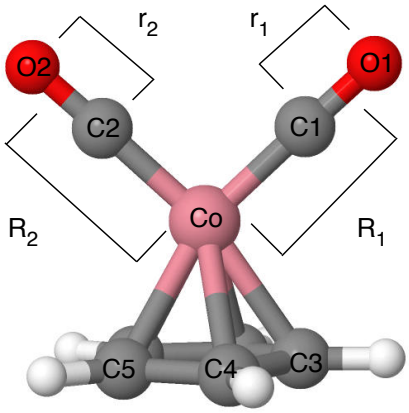

Figure 3.1: The coordinates for CO vibration (r_1, r_2) and for Co-CO dissociation (R_1, R_2) are defined along the two bond directions. Dissociation coordinates are between the Cobalt metal and the center-of-mass of the carbonyl groups and vibration coordinates are between Carbon and Oxygen.

Four-dimensional model surface was created to describe metal-carbonyl bonds dissociation and carbonyl vibrations. In Fig. 3.1 it is shown how the coordinates are defined along the two bond directions. This includes CO bond vibration coordinates r_1 and r_2, and in addition center-of-mass coordinates of the two CO groups with respect to the Cobalt metal center, R_1 and R_2. The motion is presumed to take place only along the

two bonds directions. The other degrees of freedom, like bond angles or dihedrals are not taken into account i.e. they are assumed to be frozen at their equilibrium geometry during the short propagation time. In particular for the CO motions, which are energetically decoupled in the vicinity of the global PES minimum, this will be a very good assumption.

The molecule has C_S symmetry. It means that it has two symmetry operations. Identity operation (denoted as E) is the rotation by 360° and a reflection operation about a mirror plane (denoted as σ). It can be noticed that the projection of the vector associated with R_1 points along the CH bond of the Cp ring, in contrast to R_2 which bisects a CC bond.

3.3 PES and DMS

3.3.1 PES

In the following the 4D PES will be discussed. Only the four coordinates shown in Fig. 3.1 are considered and all other degrees of freedom (DOFs) are frozen. To generate the surface, the vectors R_i are defined between Cobalt metal and the center-of-mass of Carbon and Oxygen in both carbonyl groups, where subscript $i = \{1, 2\}$ denotes the carbon monoxide group,

$$R_i = \frac{m_C r_{Ci} + m_O r_{Oi}}{M_{CO}}, \tag{3.1}$$

here m_C and m_O are the atomic mass of Carbon and atomic mass of Oxygen, respectively. The position along bonds of the Carbon and Oxygen atoms are then expressed as follows:

$$r_{Ci} = R_i + \tfrac{m_O}{M_{CO}} r_i, \tag{3.2}$$

$$r_{Oi} = R_i - \tfrac{m_C}{M_{CO}} r_i, \tag{3.3}$$

where $r_i = r_{Oi} - r_{Ci}$. The positions for Carbon and Oxygen, are determined for the R_1 and R_2 coordinates on the FFT grid, and for the r_1 and r_2 coordinates on the HO DVR grid, see Sec. 2.3.2. For the FFT grid 80 points were chosen in the interval [-1.73:5.11] a_B. For the vibrational motion 17 points were chosen in the interval [-0.50:1.00] a_B. In total there were about 1.85 milion grid points. The number of grid points and boundaries were chosen such that to have the potential minimum at a proper position. The energies at that boundaries were 64 464 cm^{-1} and 20 365 cm^{-1} for dissociation bond. For the positive value, that correspond to the dissociation motion, the exit channels were long enough to allow for a free motion of the wave packet. For vibrational bond the boundaries were 53 881 cm^{-1} and 46 793 cm^{-1}. Various cuts of the

PES are shown in Fig. 3.2. In the upper-left panel the PES is shown for two dissociation coordinates. The dissociation energy at the end of the grid along R_1 coordinate is 20 365 cm^{-1} and along R_2 coordinate is 20 191 cm^{-1}. Notice that the energy is a bit higher than from the previous studied systems [26,78]. The reason for the energy difference between two exit channels is that the projection of the vector associated with R_1 points along CH bond of the Cp ring and vector associated with R_2 bisects a CC bond. This effect is also responsible for the asymmetry of the PES, shown in the upper-right panel for CO bonding vibrations, with respect to r_1=r_2. This figure also shows the anharmonicity, which is clearly visible already for the lowest contours. The two lower panels present PES along the mixed bond vibration - dissociation coordinates, r_1-R_1 (left) and r_2-R_2 (right). There is a tilt of the PES around the equilibrium structure which points to the anharmonic coupling between these two coordinates. The values of the contours for the surfaces are presented under the figures.

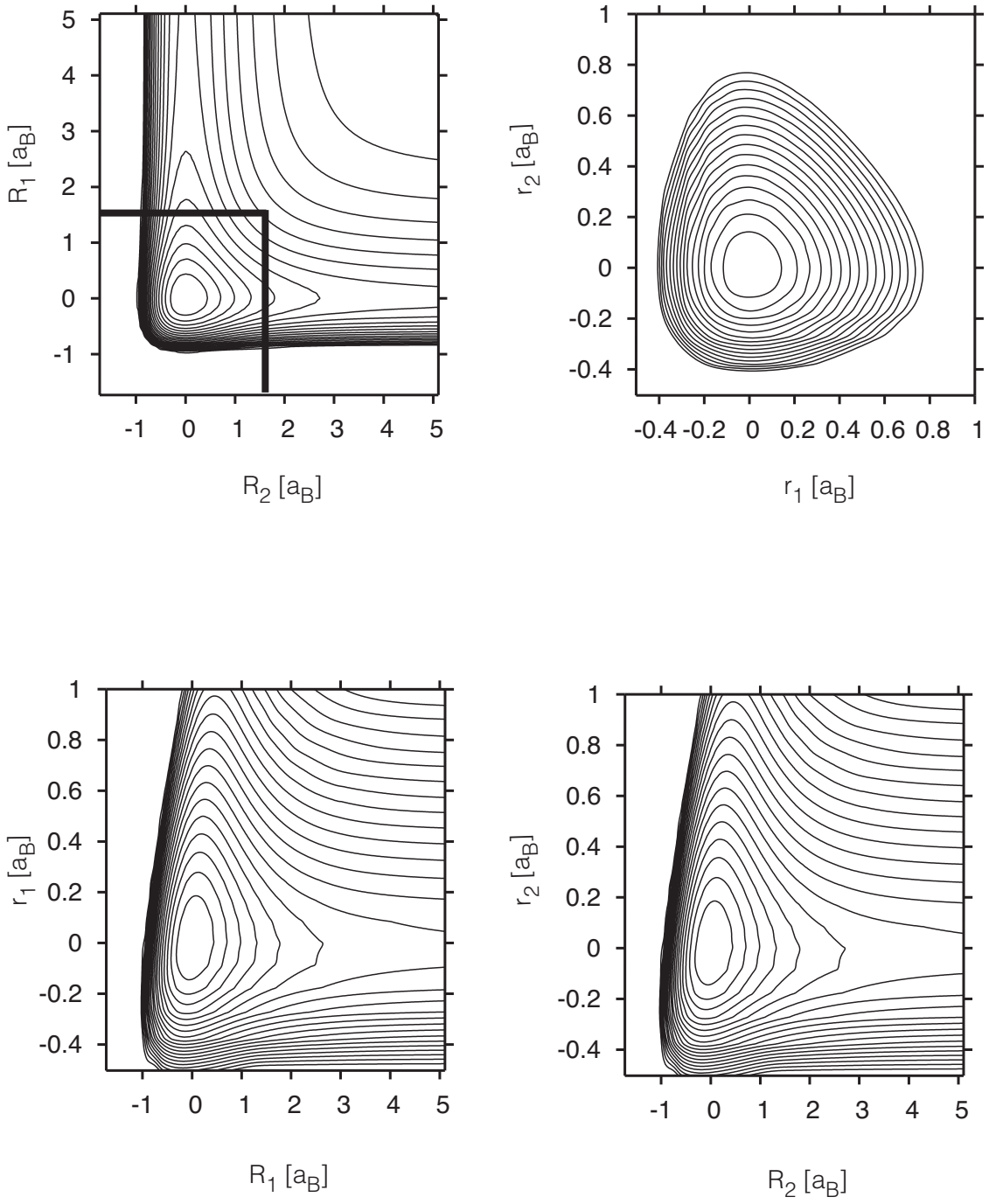

Figure 3.2: Potential Energy Surface. The upper-left panel presents the surface for dissociation coordinates. The contour values are from 3 000 cm^{-1} to 60 000 cm^{-1} in steps of 3 000 cm^{-1}. Black bars show the position of the exit channels, R_{exit}=1.5 a_B, from where reaction yield is calculated. The upper-right panel shows the surface for the vibrational coordinates. The contour lines are from 2 000 cm^{-1} to 32 000 cm^{-1} in steps of 2 000 cm^{-1}. Two lower panels present vibration - dissociation surfaces for two sets of coordinates, r_1-R_1 (left) and r_2-R_2 (right). The contour values are from 3 000 cm^{-1} to 60 000 cm^{-1} in steps of 3 000 cm^{-1}. All the coordinates that are not considered, are frozen at the equilibrium position.

3.3.2 DMS

In Fig. 3.3 we can see how the dipole moment is changing while altering the position of the carbonyl group. These changes can be seen on the dissociation coordinates surface R_1-R_2 in the upper panels of Fig. 3.4. The top middle model is in equilibrium position. The dipole moment is negative in X-direction and equal to zero in Y-direction. When R_1 coordinate is changing (top left) the dipole moment gets the negative value in Y-direction and increasing value in X-direction. When R_2 coordinate is changing (top right) the dipole moment takes a positive value in Y-direction and increasing value in X-direction. When we compress the carbonyl groups (bottom left) the dipole moment has maximum negative value in X-direction and is zero in Y-direction. When both coordinates R_1 and R_2 are changing (bottom right) the dipole is positive in X-direction and nearly zero in Y-direction. In all cases the value in Z-direction is zero.

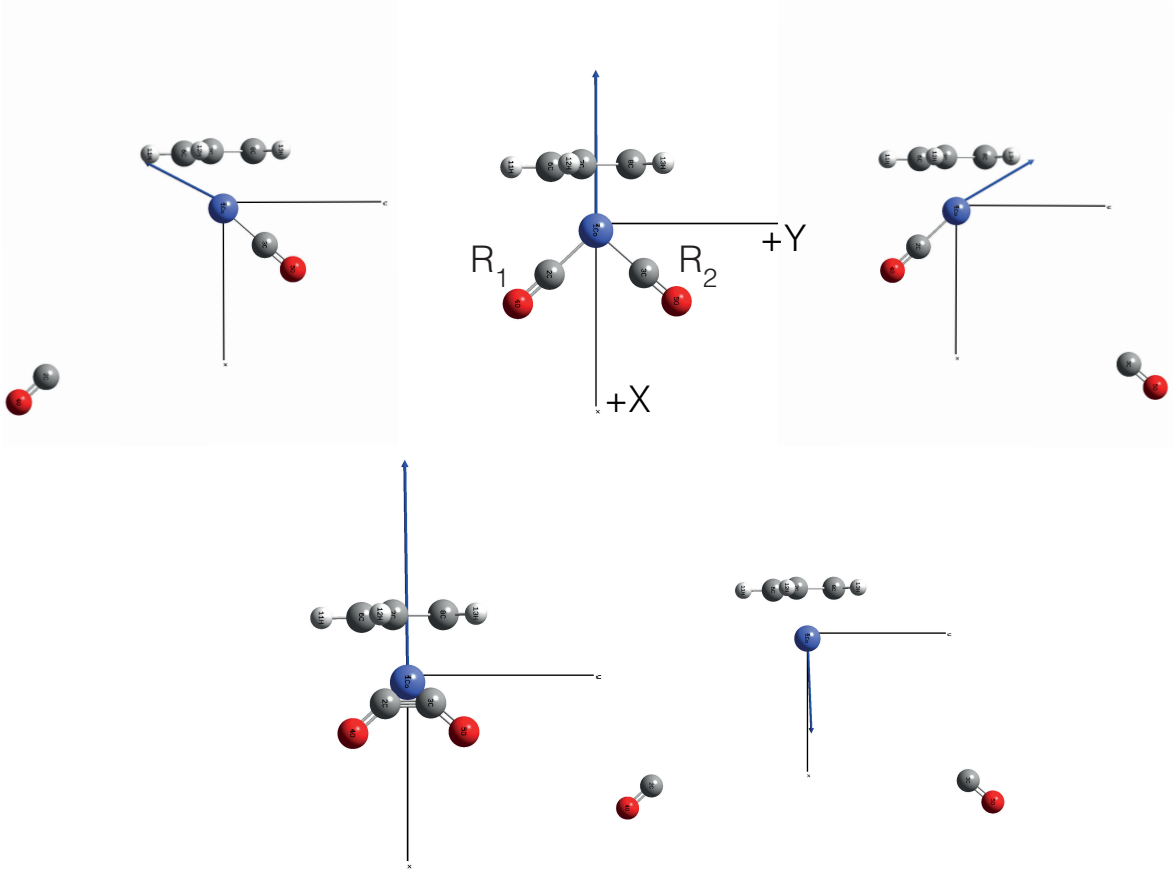

Figure 3.3: Blue arrow represents the dipole moment changing in the X-Y plane while manipulating the position of the carbonyl groups.

The 4D DMS, $\vec{d}(r_1, r_2, R_1, R_2)$ is presented in Figs. 3.4 and 3.5. These surfaces are shown for X- and Y-directions, because the dipole moment changes only in the X-Y plane.

In the upper panels of the Fig. 3.4 the DMS along dissociation coordinates R_1 and R_2 is shown for X- (left) and Y-direction (right) dipoles. The dashed lines correspond to the negative region and solid lines correspond to the positive region of the surface. The dashed and solid lines have the same meaning for all surfaces. It can be clearly seen how the value of the dipole moment is altered while dissociaiton coordinates are changing.

In the lower panels of the Fig. 3.4 the DMS along the vibration coordinates r_2 and r_1 is presented for X- (left) and Y-direction (right) dipoles. The gradient, which is easily visible from this figure, indicates that IR excitation will yield an X-polarized symmetric vibration (ν_s) along the collective coordinate $q_s = (r_1 + r_2)/2$ and an Y-polarized antisymmetric vibration (ν_a) along the collective coordinate $q_a = (r_2 - r_1)/2$. For low frequencies ($\sim$500 cm^{-1}) the symmetric and antisymmetric vibrations could be seen also for R_1 and R_2 coordinates.

The upper panels of the Fig. 3.5 present the DMS along the mixed vibration-dissociation (r_1-R_1) coordinates for X- (left) and Y-direction (right) dipoles.

The lower panels of the Fig. 3.5 show the DMS along the mixed vibration-dissociation (r_2-R_2) coordinates for X- (left) and Y-direction (right) dipoles.

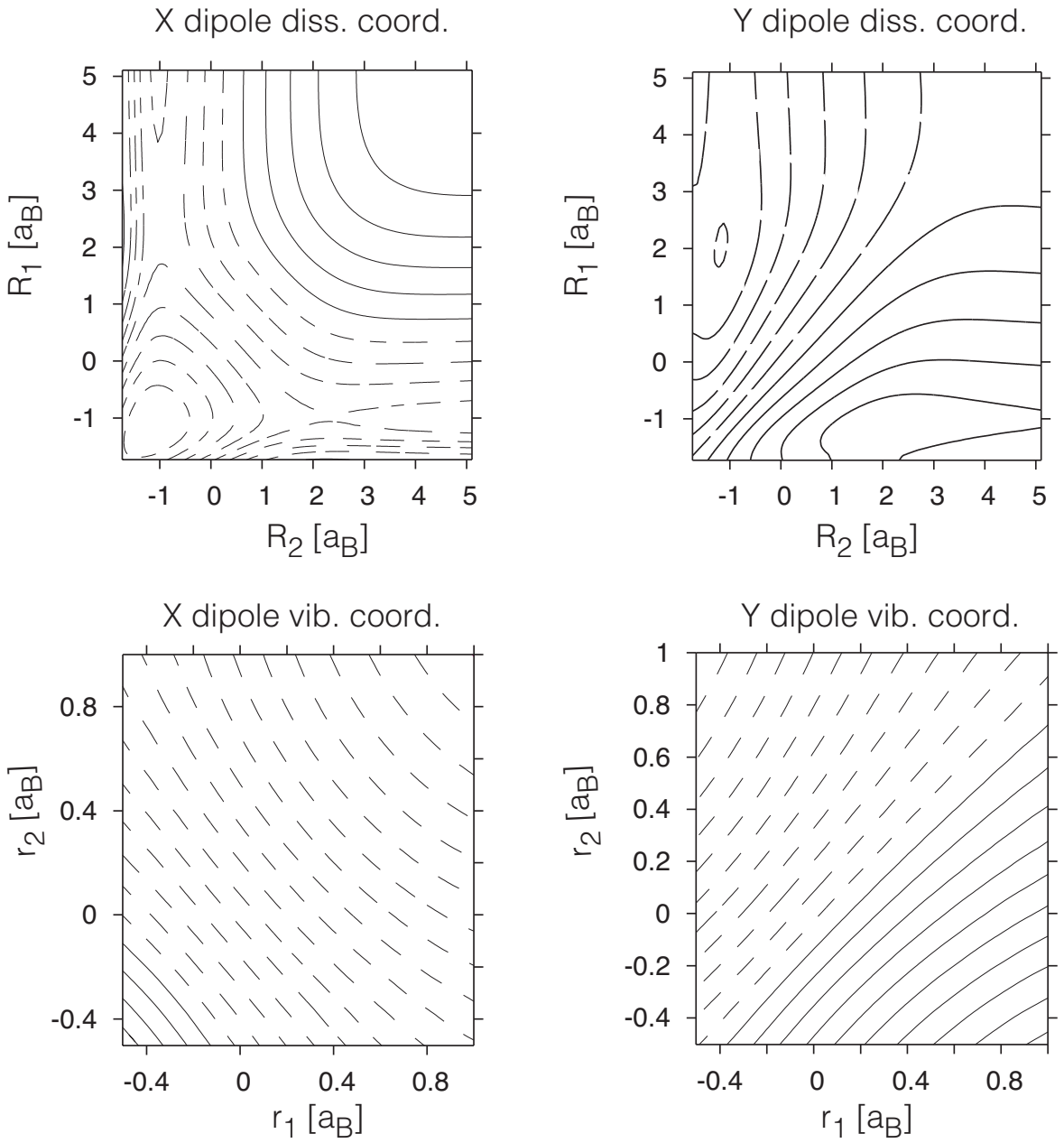

Figure 3.4: DMS for X (left column) and Y (right column) directions. In the upper (lower) panels surfaces are presented for dissociation (vibrational) coordinates. In the upper panels the contours for X-direction starts from -1.76 ea_B in steps of 0.2 and for Y-direction starts from -1.06 ea_B in steps of 0.2. In the lower panels the contour lines for X-direction starts from -3.2 ea_B in steps of 0.2 and for Y-direction starts from -2.15 ea_B in steps of 0.2. All the coordinates that are not considered, are frozen at the equilibrium position.

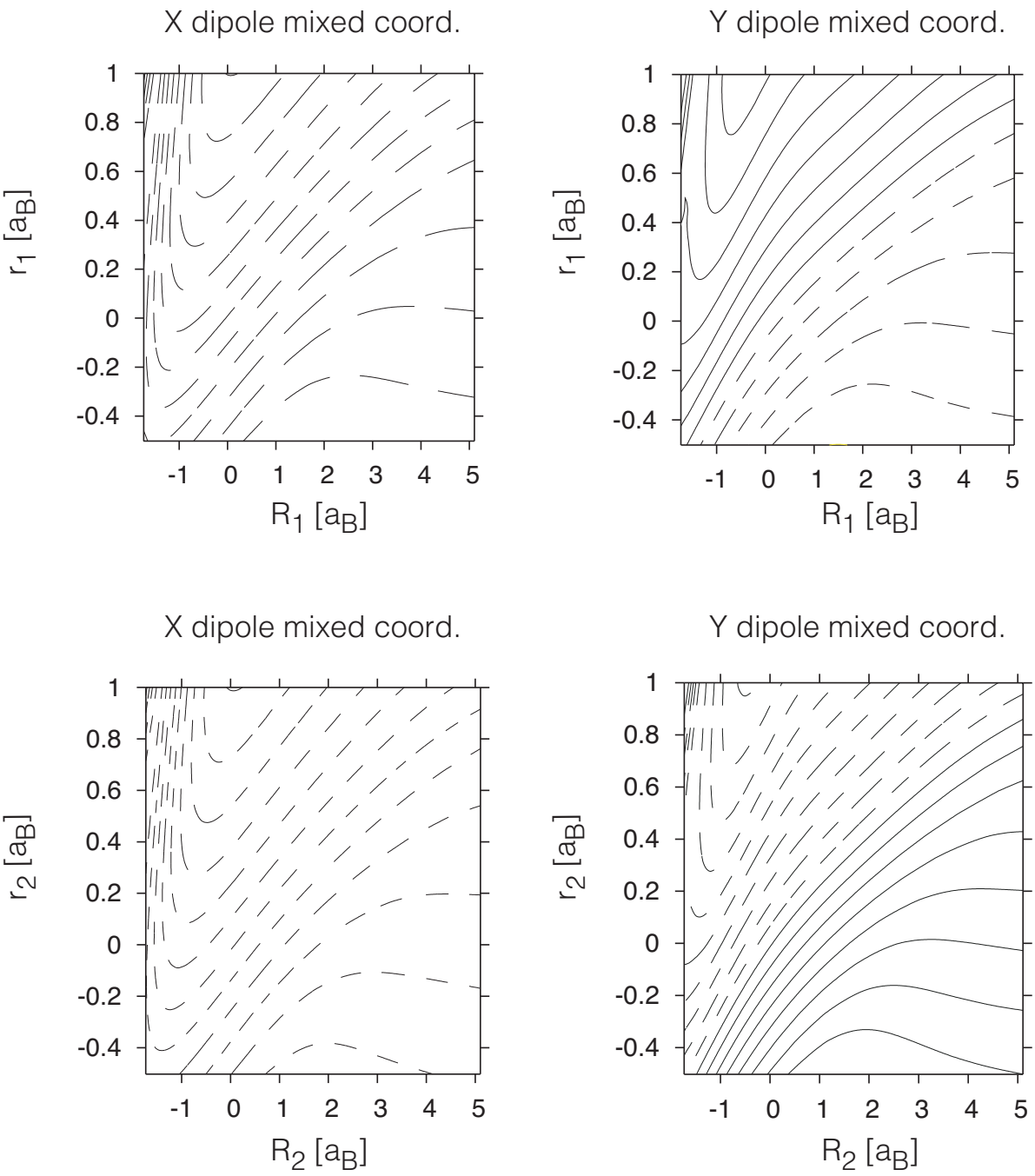

Figure 3.5: DMS for X (left column) and Y (right column) directions. In the upper panels contour lines for X-direction starts from -2.31 ea_B in steps of 0.2, notice that the entire surface is negative (dashed lines). For Y-direction contour lines starts from -1.13 ea_B in steps of 0.2. In the lower panels contour lines for X-direction starts from -2.31 ea_B in steps of 0.2 (the whole surface is negative). For the Y-direction contour lines starts from -1.69 ea_B in steps of 0.2. All the coordinates that are not considered, are frozen at the equilibrium position.

3.4 Quantum Dynamics

The time-dependent Schrödinger equation (2.56) has been solved using MCTDH method [27, 67, 69] that is implemented in the Heidelberg program package [76]. The time-dependent Hamiltonian for this model is given by

$$\begin{aligned} H(t) &= H_{mol} + H_{field}(t) \\ &= \sum_{i=1}^{2} \left(\frac{p_i^2}{2\mu_{red}} + \frac{P_i^2}{2M_{CO}} \right) + V(r_1, r_2, R_1, R_2) \\ &- \vec{d}(r_1, r_2, R_1, R_2) \cdot \vec{E}(t). \end{aligned} \tag{3.4}$$

Here, H_{mol} and $H_{field}(t)$ are the time-independent and time-dependent parts of the Hamiltonian, respectively. The first part of H_{mol} is the kinetic energy operator, where M_{CO} is the total CO mass, $M_{CO} = m_C + m_O = 12u + 16u = 28u$ and μ_{red} is the reduced mass of the CO vibration defined as

$$\mu_{red} = \frac{m_C m_O}{m_C + m_O}, \tag{3.5}$$

and in this case has the value, $\mu_{red} = 6.86u$. The second part of H_{mol} is the PES, $V(r_1, r_2, R_1, R_2)$. The time-dependent part of the Hamiltonian $H_{field}(t)$ describes the matter-field interaction. Within the dipole approximation the electric field $\vec{E}(t)$ interacts with the DMS - $\vec{d}(r_1, r_2, R_1, R_2)$. The 4D wave function $\Psi(t)$ is represented - on the DVR grid - by the SPFs. The number of SPFs will be different for the different types of simulations and will be specified below. For all of the simulations the combination of modes has been used, such that mode r_1 was combined with R_1 and r_2 with R_2. The propagation has been performed using CMF scheme together with the BS and the SIL integrators for the SPFs and A-coefficients, respectively (see Sec. 2.3).

The PES and DMS were fitted to a product representation using the *potfit* module of the MCTDH package [81]. The PES has been cut-off at 8 eV. 25 natural potentials have been used for r_2-R_2 combined modes and have been contracted over r_1-R_1 combined modes. Correlated weights have been chosen such that gridpoints associated with energies > 5 eV had zero weights. For X and Y DMS, the number of natural potentials was the same but there were no cut-off and no correlated weights specified.

The ground state expectation values in a_B for the position and their standard deviation are shown in Table 3.2.

Moreover, the reaction yield for bond breaking will also be studied. It is defined in terms of the Heaviside step function operator, placed into the exit channel of the

	r_1	R_1	r_2	R_2
position	0.0081	0.0120	0.0081	0.0120
standard deviation	0.0673	0.0699	0.0673	0.0700

Table 3.2: The expectation values for position and standard deviation for equilibrated system.

PES [82]

$$\begin{aligned} Y_1(t) &= \langle \Psi(t) | \, \Theta(R_1 - R_{\text{exit}}) \, | \Psi(t) \rangle \, , \\ Y_2(t) &= \langle \Psi(t) | \, \Theta(R_2 - R_{\text{exit}}) \, | \Psi(t) \rangle \, . \end{aligned} \tag{3.6}$$

$Y_1(t)$ and $Y_2(t)$ are the reaction yields for the two exit channels R_1 and R_2. Step function $\Theta(R - R_{\text{exit}})$ is placed at $R_{\text{exit}} = 1.5$ a_B. The R_{exit} are shown in the Fig. 3.2 in the upper-left panel as two black bars for two channels.

3.5 IR Spectrum

The IR spectra were calculated for harmonic and anharmonic cases, see Eq. (2.63). The interesting range of the collective CO stretching vibrations is around 2000 cm^{-1}. Within the harmonic approximation the antisymmetric and symmetric CO vibrations are found at 1949 cm^{-1} and 1997 cm^{-1}, respectively. The vibration of Co-CO is located at 559 cm^{-1}. This three normal modes of vibrations are presented in Fig. 3.6. Black arrows show the displacements of the atoms. Vibrations of the Cp ring are located around 800 cm^{-1}.

Figure 3.6: Normal mode displacement vectors and harmonic frequencies for selected modes.

Harmonic (upper panel) and anharmonic (lower panel) IR spectra are presented

in Fig. 3.7. Anharmonic IR absorption spectrum were computed in terms of Fourier transform of autocorrelation function presented in Eq. (2.63) and discussed in Ref. [46]. According to this equation the normalization constant and energy prefactor have been used and τ, which is responsible for the broadening of the spectrum, has been set to $\tau = 1667$ fs. This value has been chosen, because the FWHM for the harmonic spectrum was 3 cm^{-1} in order to have a good resolution. The final propagation time was 4000 fs and the number of SPFs for both combine modes was 4. When including anharmonicity within 4D model the CO vibrations change to 1922 cm^{-1} (Y-polarized ν_a) and 1968 cm^{-1} (X-polarized ν_s). Because of the anharmonicity their frequency decreases. Additional transitions were found at 433 and 443 cm^{-1} for X- and Y-dipole surface, respectively. They correspond to symmetric and antisymmetric contributions of the dissociation bond coordinates. The intensity of these peaks was magnified 10 times.

There are no experimental data up-to-date for the gas phase model. IR spectra were taken in a $CHCl_3$ solution and have values 1967 cm^{-1} and 2028 cm^{-1} for antisymmetric and symmetric vibrations, respectively [83]. They are presented as black bars in the lower panel of the Fig. 3.7. The difference between the theory and the experiment comes from the fact that the experiment was done in a solution. Moreover, theoretical model has only four DOFs and interactions with the additional vibrations could shift the spectrum. Furthermore, different choice of the functional and basis set in the DFT calculation could make the PES look different and cause a shift of the spectrum as well.

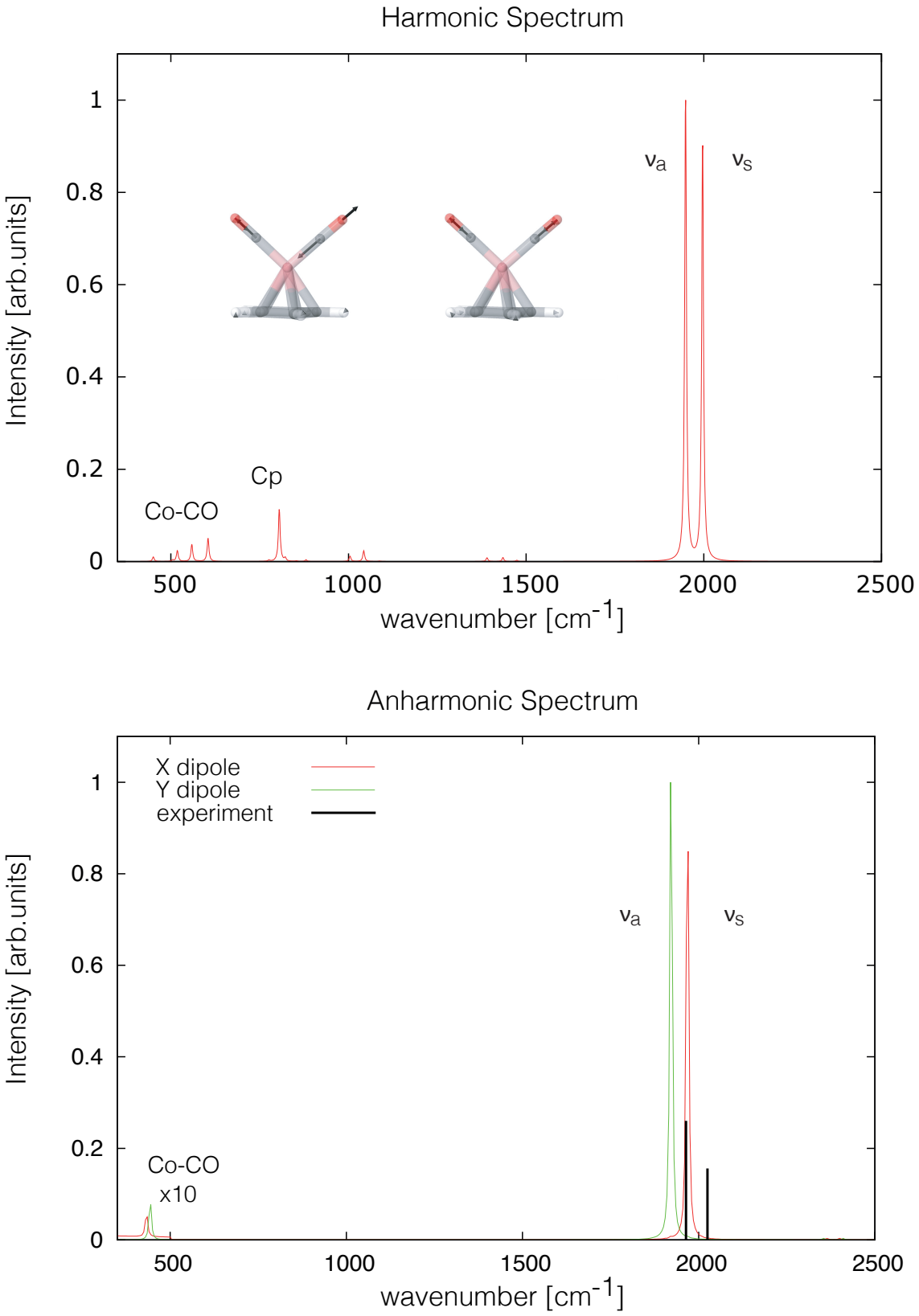

Figure 3.7: Harmonic (upper panel) and anharmonic (lower panel) IR spectra. The symmetric and antisymmetric collective CO vibrations are around 2000 cm^{-1}. Normal modes displacement are illustrated in the upper panel. The FWHM for the harmonic spectrum is 3 cm^{-1}. Experimental values taken in $CHCl_3$ solution from [83].

3.6 Linearly-Polarized Light

Linearly-polarized light is used to investigate the possibility of bond breaking by inducing collective carbonyl vibrations. According to the DMS, light polarized in X-direction will induce symmetric CO vibrations and light polarized in Y-direction will induce antisymmetric CO vibrations. In all simulations using polarized light the molecule is assumed to be fixed with respect to the laboratory frame. This can be achieved, for example, on the surface. The molecule is relatively large and rotations, on the time scale of the laser field, can be neglected. TDSE given in Eq. (2.56) has been solved with the time-independent molecular system Hamiltonian, H_{mol}, and the time-dependent field Hamiltonian, $H_{field}(t)$, having the form as presented in Eq. (3.4). For linear light the electric field $\vec{E}(t)$ is given by

$$\vec{E}(t) = \mathcal{E}(t)\vec{e}\cos(\omega t + \phi). \tag{3.7}$$

Here, ϕ is a phase, ω is the angular frequency and $\mathcal{E}(t)$ is the field envelope defined in Eq. (2.59). In order to induce symmetric CO vibrations, electric field interacts with the X-component of DMS. In Fig. 3.8 the lower panel shows the electric field that was used. Amplitude was chosen to be, $E_0 = 0.03$ $\mathrm{E_h/ea_B}$, the width of the Gaussian was $\tau = 25$ fs and was centered at $t_0 = 750$ fs. The frequency of the pulse, ω was chosen to be approximately in resonance with the symmetric CO vibrations and was $\omega = 1965$ $\mathrm{cm^{-1}}$. There were 18 SPFs for each combined mode (consist of two degrees of freedom, r_1, R_1 and r_2, R_2) and the maximum population of the least occupied SPF was about 0.4%. The pulse was tuned such as to excite the system to the energy approximately equal the energy of dissociation, $\langle H_{mol} \rangle = 2.5$ eV $= 20\ 160$ $\mathrm{cm^{-1}}$. This change of the energy according to the molecular Hamiltonian H_{mol} can be seen in the upper panel of Fig. 3.8. In Fig. 3.9 the reaction yield for bond breaking is presented by means of a step-function operator, Eq. (3.6). The yield is $\sim 10^{-7}$ and consequently there is no dissociation taking place.

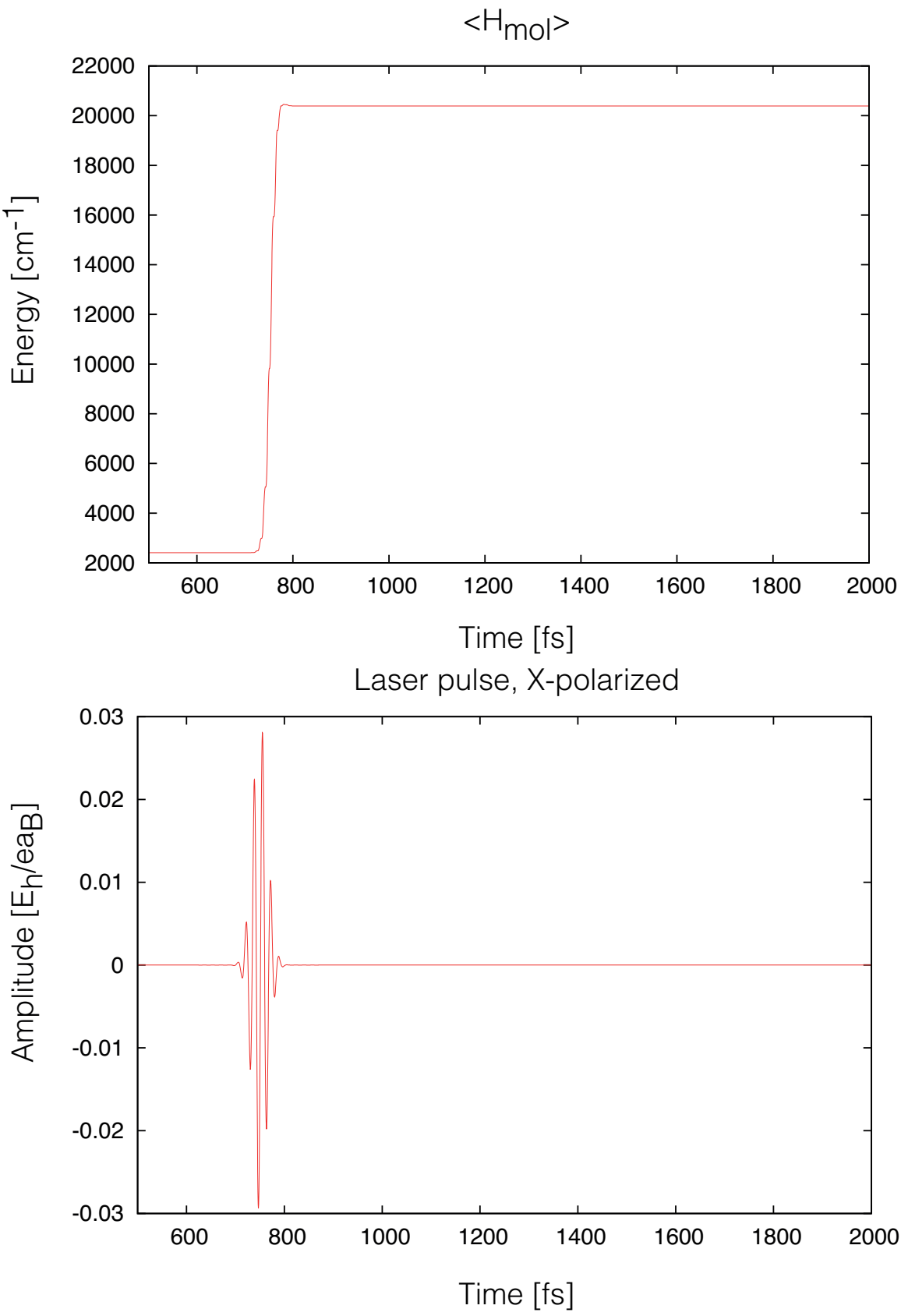

Figure 3.8: Expectation value of the system Hamiltonian for the simulation with linearly-polarized light (upper panel) and laser pulse (lower panel).

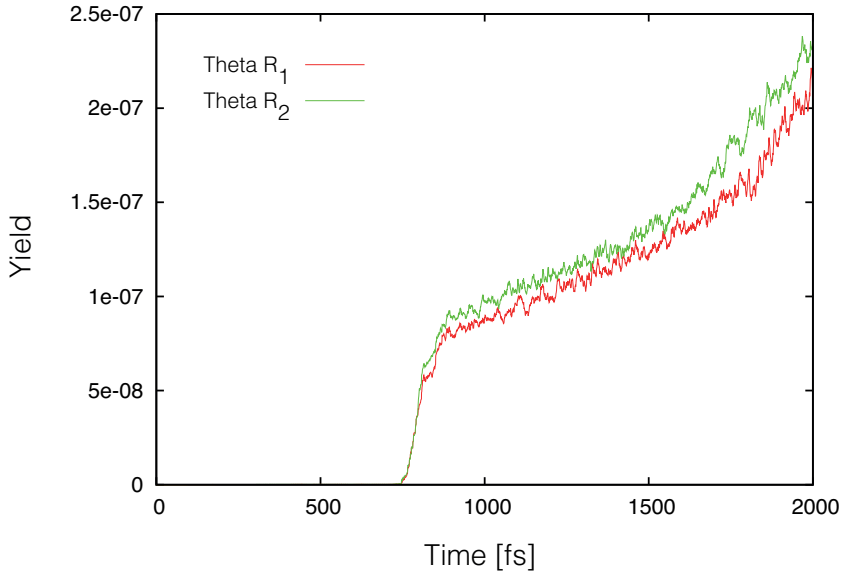

Figure 3.9: Reaction yields for two exit channels for the simulation with linearly-polarized light (X-direction).

In Fig. 3.10 the position and standard deviation (defined as $\sqrt{< r^2 > - < r >^2}$) for vibrational coordinates are presented. The wave packet starts to change its position in the laser field and its width increases. Then it oscillates with respect to an on-average constant position and with an on-average constant width.

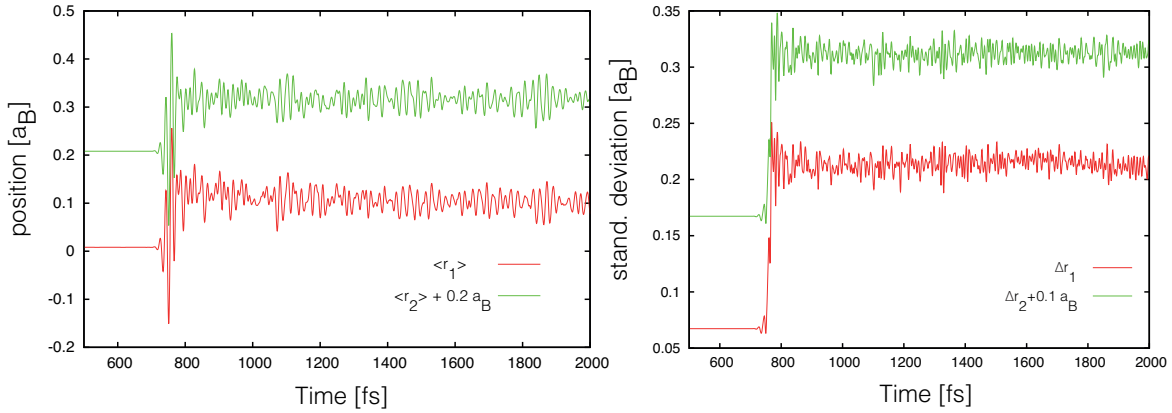

Figure 3.10: Position and standard deviation for vibrational coordinates for $\vec{e}_X$ polarized field excitation. Position for r_2 is shifted by 0.2 a_B and standard deviation by 0.1 a_B for clarity.

In Fig. 3.11 the positions and standard deviations are presented for mixed coordinates r_1-R_1 and r_2-R_2. The vibrational coordinate for r_1 is discussed above. The dissociation coordinate R_1 starts to move when laser field hits the system but its oscillation amplitude decrease in time. The width of the wave packet is constantly increasing. The behavior for r_2-R_2 is similar.

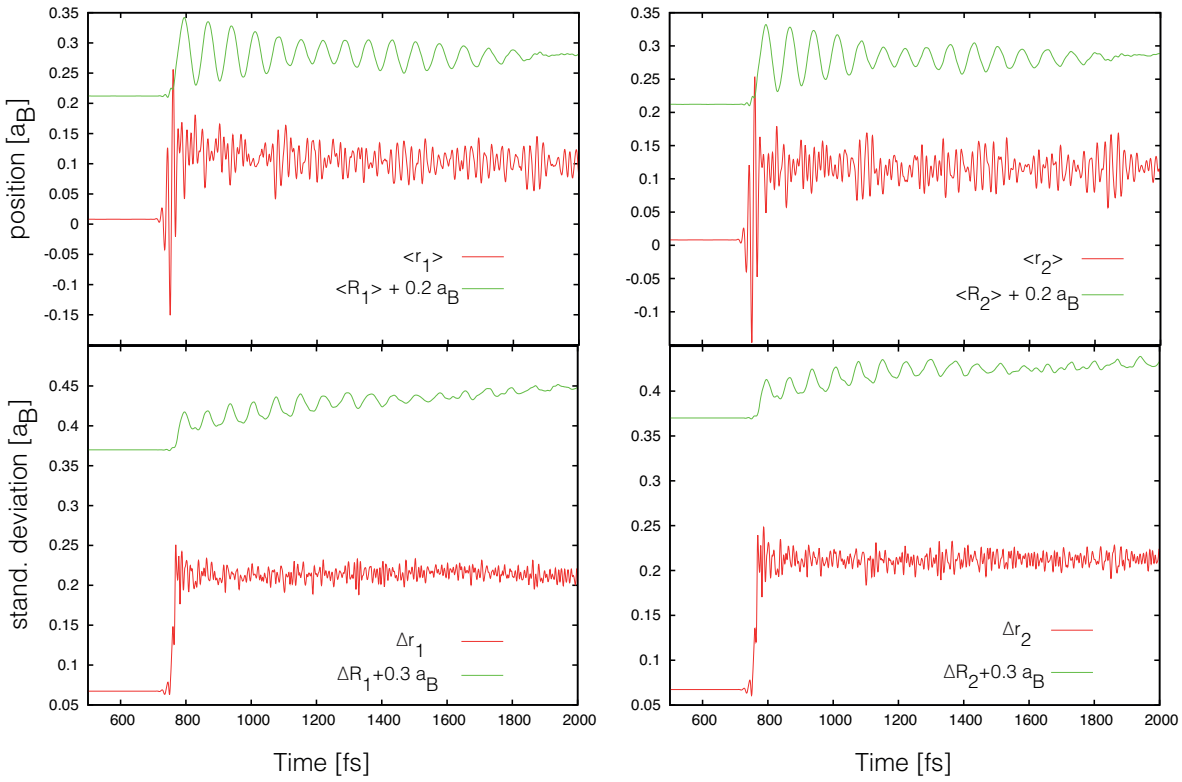

Figure 3.11: Position and standard deviation for mixed coordinates for $\vec{e}_X$ polarized field excitation. Position for R_1 and R_2 are shifted by 0.2 a_B and standard deviation by 0.3 a_B for clarity.

In order to induce antisymmetric CO vibrations, the electric field interacts with the Y-component of the DMS. In the analogy to Fig. 3.8, Fig. 3.12 shows changes in the expectation value of the molecular Hamiltonian $\langle H_{mol} \rangle$ (upper panel) and the pulse itself (lower panel). The pulse parameters were chosen similarly to the previous simulation but the frequency of the pulse ω, was approximately in resonant with the antisymmetric CO vibration and was $\omega = 1920$ cm^{-1}. There were 18 SPFs for each combined mode and the maximum population of the least occupied SPF was about 0.5%. The reaction yield presented in Fig. 3.13 is also small, $\sim 10^{-7}$ and therefore no dissociation could be observed. The difference between R_1 and R_2 comes from the fact that the PES is not symmetric and the two exit channels are not equivalent. When exciting antisymmetric vibrations the wave packet stays longer in the region where $r_1 > r_2$.

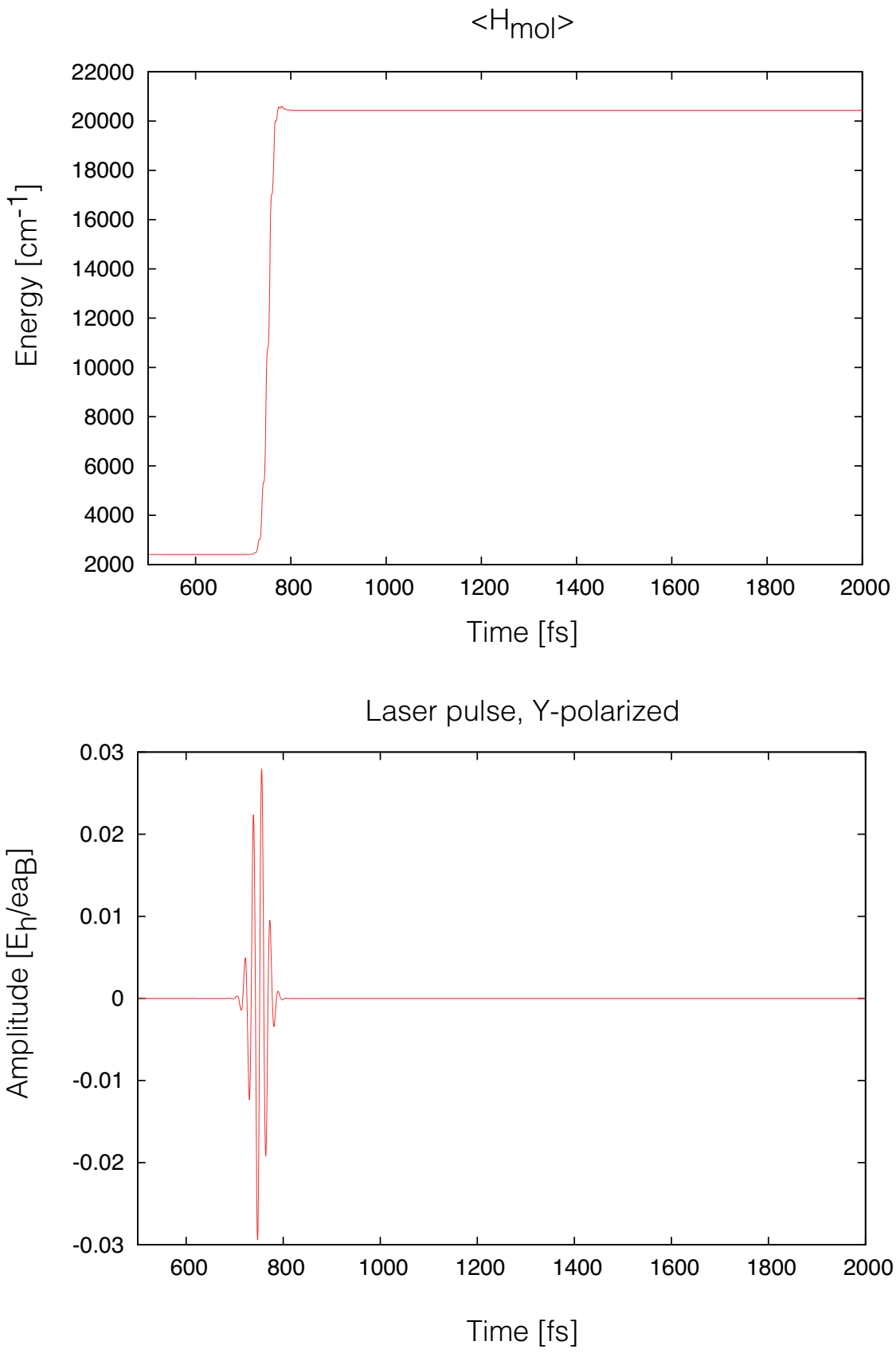

Figure 3.12: Expectation value of the system Hamiltonian for the simulation with linearly polarized light (upper panel) and laser pulse (lower panel).

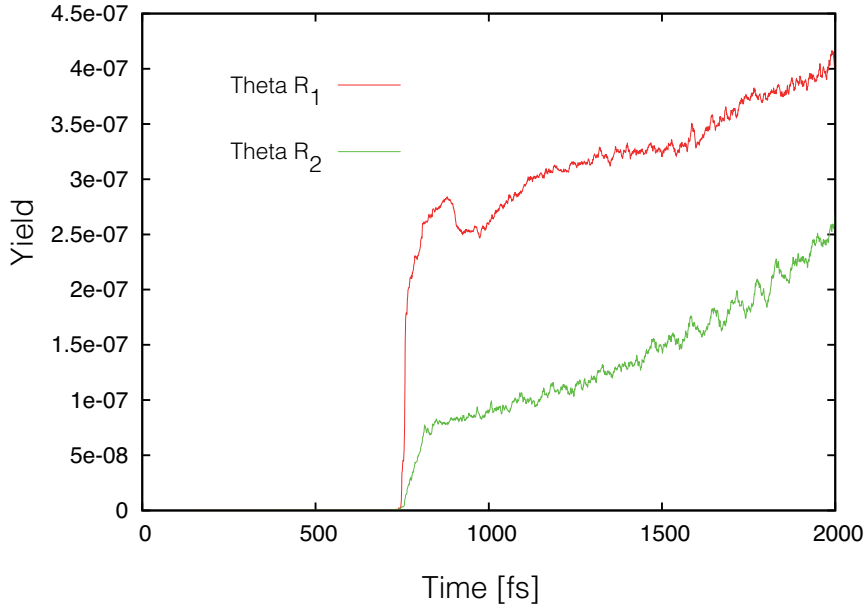

Figure 3.13: Reaction yields for two exit channels for the simulations with linearly Y-polarized light.

In Fig. 3.14 the position and standard deviation for vibrational coordinate are presented. In Fig. 3.15 the positions and standard deviations are presented for mixed coordinates r_1-R_1 and r_2-R_2. The behavior of the expectation values for all cases is similar as for the simulation with X-component of DMS discussed above.

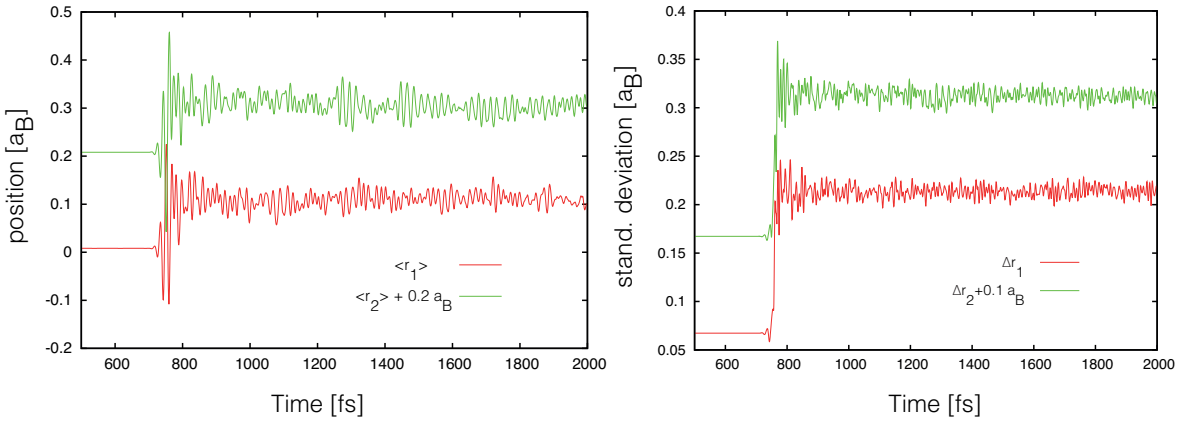

Figure 3.14: Position and standard deviation for vibrational coordinates for $\vec{e}_Y$ polarized field excitation. Position for r_2 is shifted by 0.2 a_B and standard deviation by 0.1 a_B for clarity.

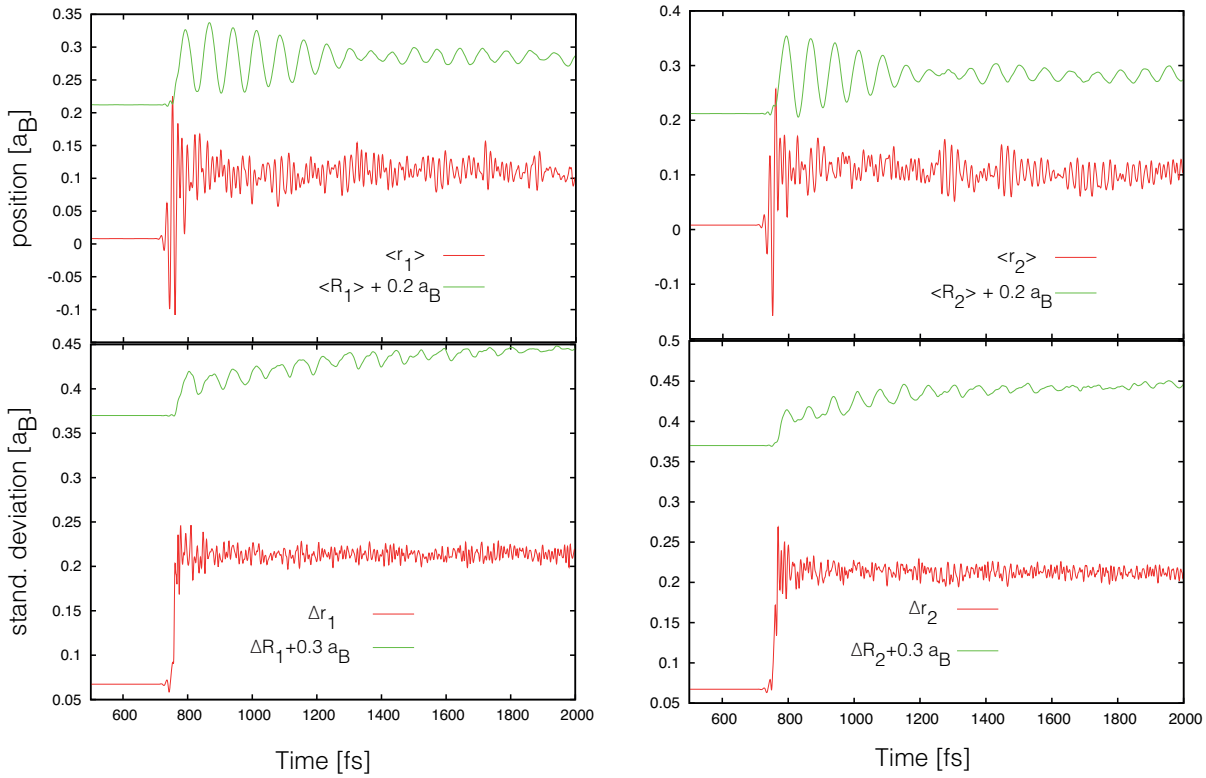

Figure 3.15: Position and standard deviation for mixed coordinates for $\vec{e}_Y$ polarized field excitation. Positions for R_1 and R_2 are shifted by 0.2 a_B and standard deviation by 0.3 a_B for clarity.

From the simulations with linearly-polarized light one can see that bond breaking between metal and carbonyl cannot be achieved by simple IR excitation of the symmetric and antisymmetric carbonyl stretching oscillations. Energy is distributed on a collective vibrations and is not sufficient to induce dissociation. Expectation values of the dissociation coordinates show the initial motion of this coordinates but the elongation is not enough. In the same time the standard deviation increases. This is the reason why the reaction yields are very low i.e. around 10^{-7}.

3.7 Localization of collective CO vibrations

The collective nature of the CO normal mode vibrations in cases of multiple CO groups introduces a challenge for laser control of bond breaking, since upon excitation the energy is not deposited into a single bond, but is spread over many bonds within the molecule. The question arises, if using femtosecond IR laser pulses, would one be able to induce localized vibrations along a *single* CO bond. In order to explore this issue one can use a two-pulse scheme with *relative* phase between them, as described in Sec. 2.4. Recalling the Eq. (2.61)

$$\vec{E}(t) = \mathcal{E}(t)(\vec{e}_X \cos(\omega_X t + \phi_X) + \vec{e}_Y \cos(\omega_Y t + \phi_Y)),$$

where, $\mathcal{E}(t)$ is the gaussian shape envelope, $\vec{e}_X = (1, 0, 0)$ and $\vec{e}_Y = (0, 1, 0)$, frequencies - ω_X and ω_Y - have been chosen to be approximately resonant with the fundamental transition of the ν_s and ν_a mode, polarized in X and Y direction, respectively (ω_X = 1965 cm^{-1} and ω_Y = 1920 cm^{-1}). The phases $\phi_{X,Y}$ have different values for different polarization directions $\vec{e}_{X,Y}$. It can be noticed, that only the relative phase, $\Delta\phi = \phi_Y - \phi_X$, will be of interest in the following. Three different field amplitudes will be considered, $E_0 = 0.001$ E$_\mathrm{h}$/ea$_\mathrm{B}$, $E_0 = 0.0015$ E$_\mathrm{h}$/ea$_\mathrm{B}$ and $E_0 = 0.002$ E$_\mathrm{h}$/ea$_\mathrm{B}$. Each is selected such that the expectation value of the 4D molecular Hamiltonian rises up to a certain energy and no decrease due to the stimulated emission is observed. The energy uptake for these three cases is about 560, 1260 and 2230 cm^{-1} as shown in the middle panel in Fig. 3.16 with the choice of $\Delta\phi = 0$ degree. The energy expectation value is not significantly influenced by the alternative choice of $\Delta\phi = 180$ degrees. In terms of the PES in the upper panels in Fig. 3.16 these energies are still in the part where the anharmonicity of the PES is small. Furthermore, these energies are well below the dissociation threshold, i.e. wave packet motion will occur approximately in the range up to the red contour lines at 3000 cm^{-1} and at 4500 cm^{-1}, which indicate approximately energies for amplitude $E_0 = 0.001$ E$_\mathrm{h}$/ea$_\mathrm{B}$ and $E_0 = 0.002$ E$_\mathrm{h}$/ea$_\mathrm{B}$, respectively. The lower panel of this figure presents the laser pulses polarized in X and Y direction for the $\Delta\phi = 0$ degrees.

The position expectation values for the $\langle r_1 \rangle$ and $\langle r_2 \rangle$ coordinates together with their standard deviations are shown in Fig. 3.17 in the left and right panels, respectively. The relative phase between the pulses is $\Delta\phi = 0$ degree. The bond oscillations are modulated such that if $\langle r_1 \rangle$ has its minimum $\langle r_2 \rangle$ has a maximum and vice versa. In terms of the dynamics on the bond distance PES this implies that there are certain periods where the motion is essentially along r_1 or r_2 only. In other words, whereas each pulse separately would excite a collective vibration, i.e. along $q_s = (r_1 + r_2)/2$ or

$q_a = (r_2 - r_1)/2$, a superposition of the two pulses leads to a transient localization of the vibrational motion in the individual CO bonds. The wave packet associated with this localized vibration, however, does not correspond to an eigenstate of the system. For the weak-field excitation (upper-left panel), i.e. $E_0 = 0.001$ $\mathrm{E_h/ea_B}$, this oscillation is easily identified. One observes a wave packet motion between two localized vibrations with a time scale for "switching" of about $\pi/(\omega_s - \omega_a) = 363$ fs. During the propagation the wave packets stay rather compact, which can be seen from the upper-right panel in Fig. 3.17, where the standard deviation of the coordinates is plotted. This indicates that anharmonicity is still rather small under these excitation conditions. Starting around 1500 fs we notice that the localization in one coordinate is no longer perfect, i.e. the wave packet becomes increasingly influenced by the anharmonicity of the potential and the relation for the "switching" time - $\pi/(\omega_s - \omega_a)$ - no longer holds.

When increasing the field amplitude to $E_0 = 0.0015$ $\mathrm{E_h/ea_B}$ the localization is no longer perfect and the wave packet dispersion is stronger. It can be seen in the middle panels of Fig. 3.17. Here, one may see that when the oscillation amplitude of $\langle r_1 \rangle$ decreases the standard deviation of the wave packet at the same time increases.

By increasing the field amplitude to $E_0 = 0.002$ $\mathrm{E_h/ea_B}$ the wave packet dispersion is more pronounced and the simple two state superposition picture should break down. Nevertheless, the weak-field behavior of oscillations is still visible from lower-left panel in Fig. 3.17. Notice, that in particular the oscillation amplitude of $\langle r_1 \rangle$ decreases. Since the standard deviation increases at the same time (lower-right panel), the delocalized wave packet is no longer well described by the coordinate expectation value, i.e. the classical picture of a vibrating bond coordinate doesn't apply.

The molecule-field interaction from Eq. (3.4) can be written approximately as

$$H_{\mathrm{field}}(t) \approx \mathcal{E}(t)(q_{\mathrm{s}} \cos(\omega t) + q_{\mathrm{a}} \cos(\omega t + \Delta\phi)). \tag{3.8}$$

Hence, for the choice of $\Delta\phi = 0$, the field effectively drives the coordinate $q_s + q_a = r_2$, i.e. the superposition which corresponds to localized motion along r_2, cf. Fig. 3.17. For the alternative choice of $\Delta\phi = 180$ degrees, however, one would expect a driving of $q_s - q_a = r_1$. Indeed, this is true as can be seen from Fig. 3.18 in the upper-left panel. Since there is not much difference in the PES concerning the two directions, a behavior similar to $\Delta\phi = 0$ is found upon increasing the field amplitude to $E_0 = 0.0015$ $\mathrm{E_h/ea_B}$ and $E_0 = 0.002$ $\mathrm{E_h/ea_B}$, middle and lower panels, respectively.

The maximum populations of the least occupied SPF for simulations in Figs. 3.17 and 3.18 are shown in Appendix A.

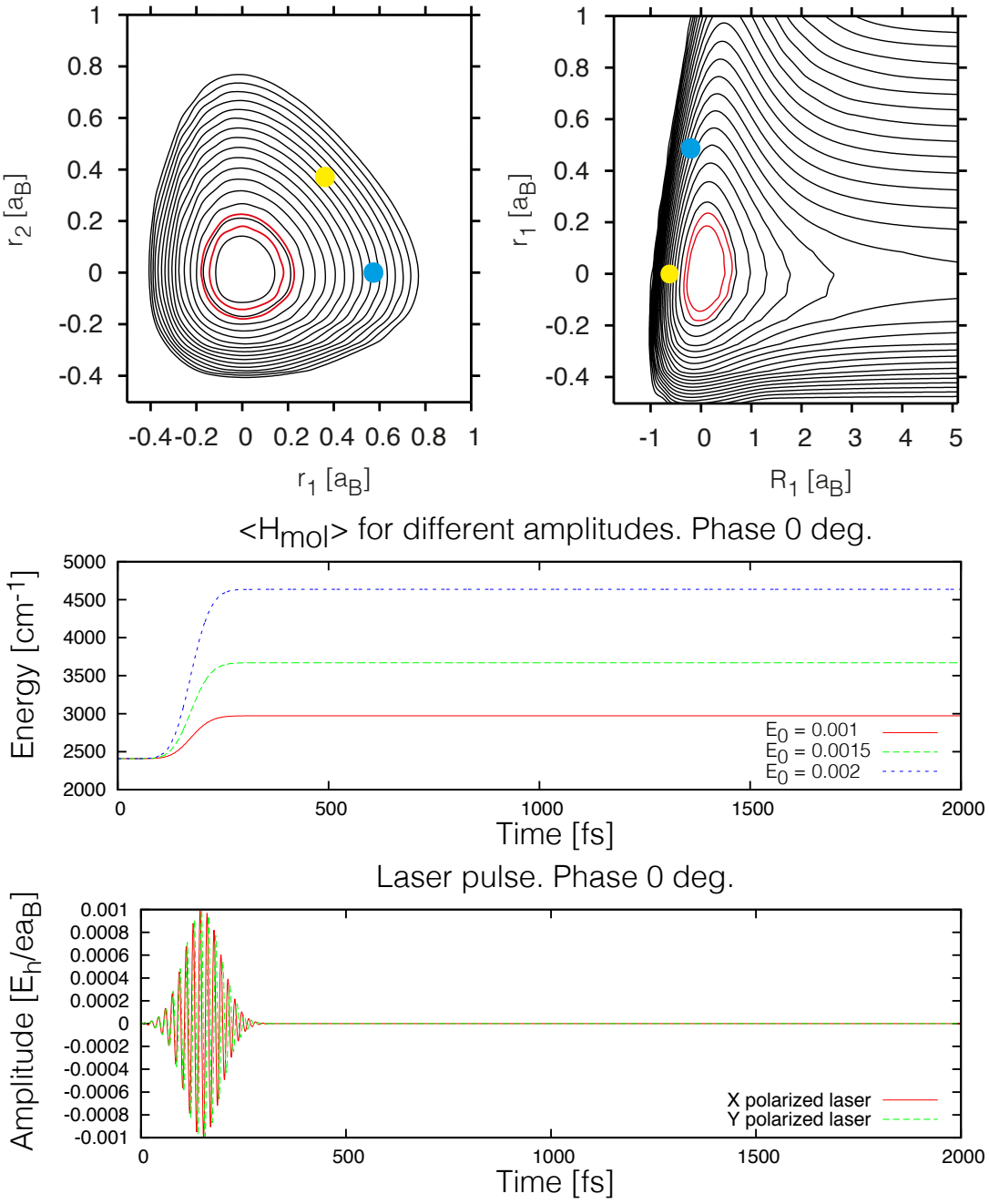

Figure 3.16: In the upper panels red contour lines at 3 000 cm^{-1} and at 4 500 cm^{-1} point out the energy gained by the system for simulations with amplitudes, defined in Eq. (2.59), $E_0 = 0.001$ E_h/ea_B and $E_0 = 0.002$ E_h/ea_B, respectively. Yellow and blue dots on the surfaces indicate the initial displacement of the wave packet as simulated in Sec. 3.8. In the middle panel the energy expectation value is presented for three different laser pulse amplitudes 0.001, 0.0015, 0.002 E_h/ea_B. Phase between two pulses is zero, for phase 180 degrees the energy (not shown) has similar values. The laser pulse for amplitude 0.001 E_h/ea_B is shown in the lower panel and the width of the pulse is τ=75 fs.

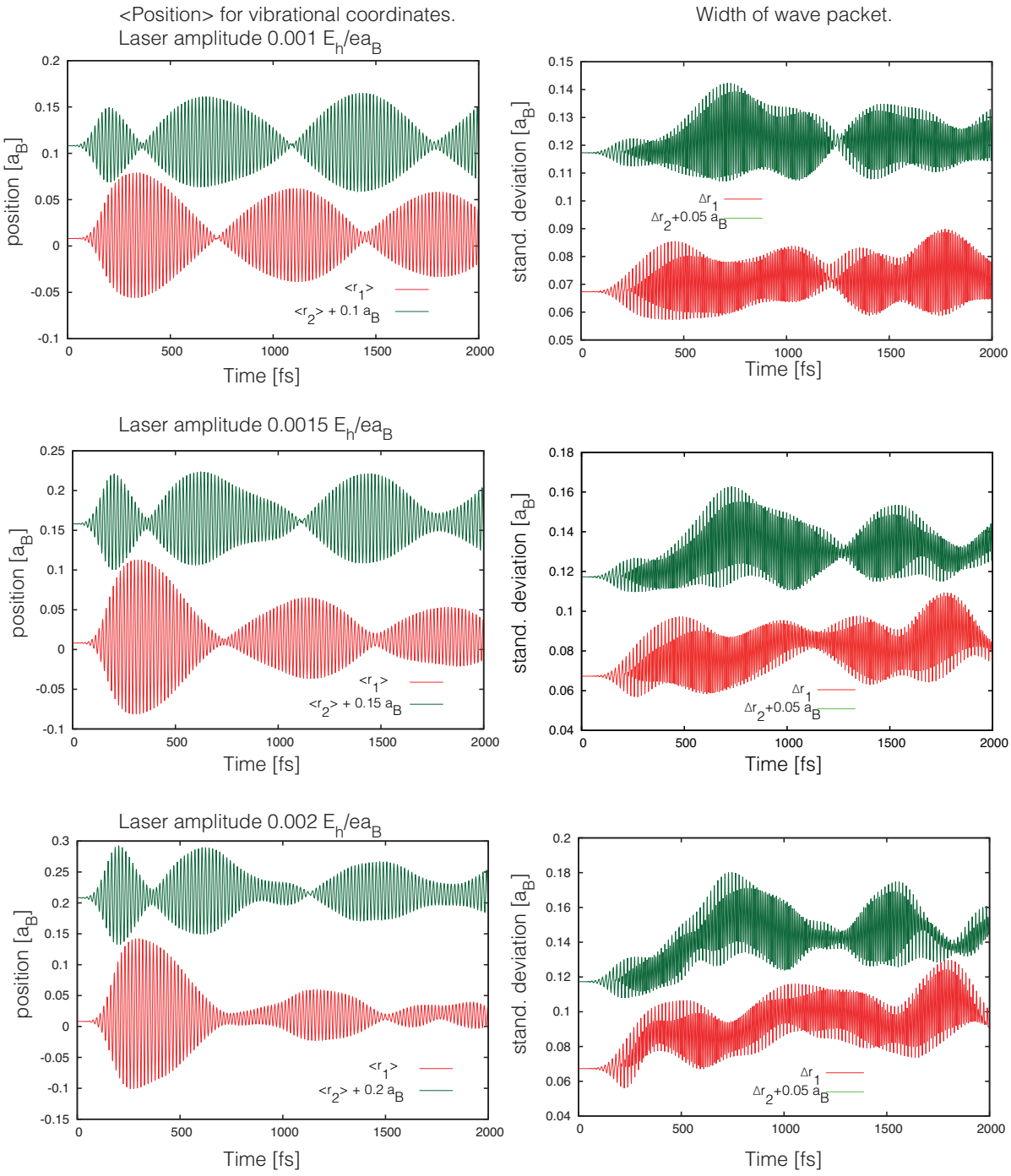

Figure 3.17: Position expectation values and standard deviation of the wave packet for r_1 and r_2 degrees of freedom for three different field amplitudes. The phase between the pulses is zero.

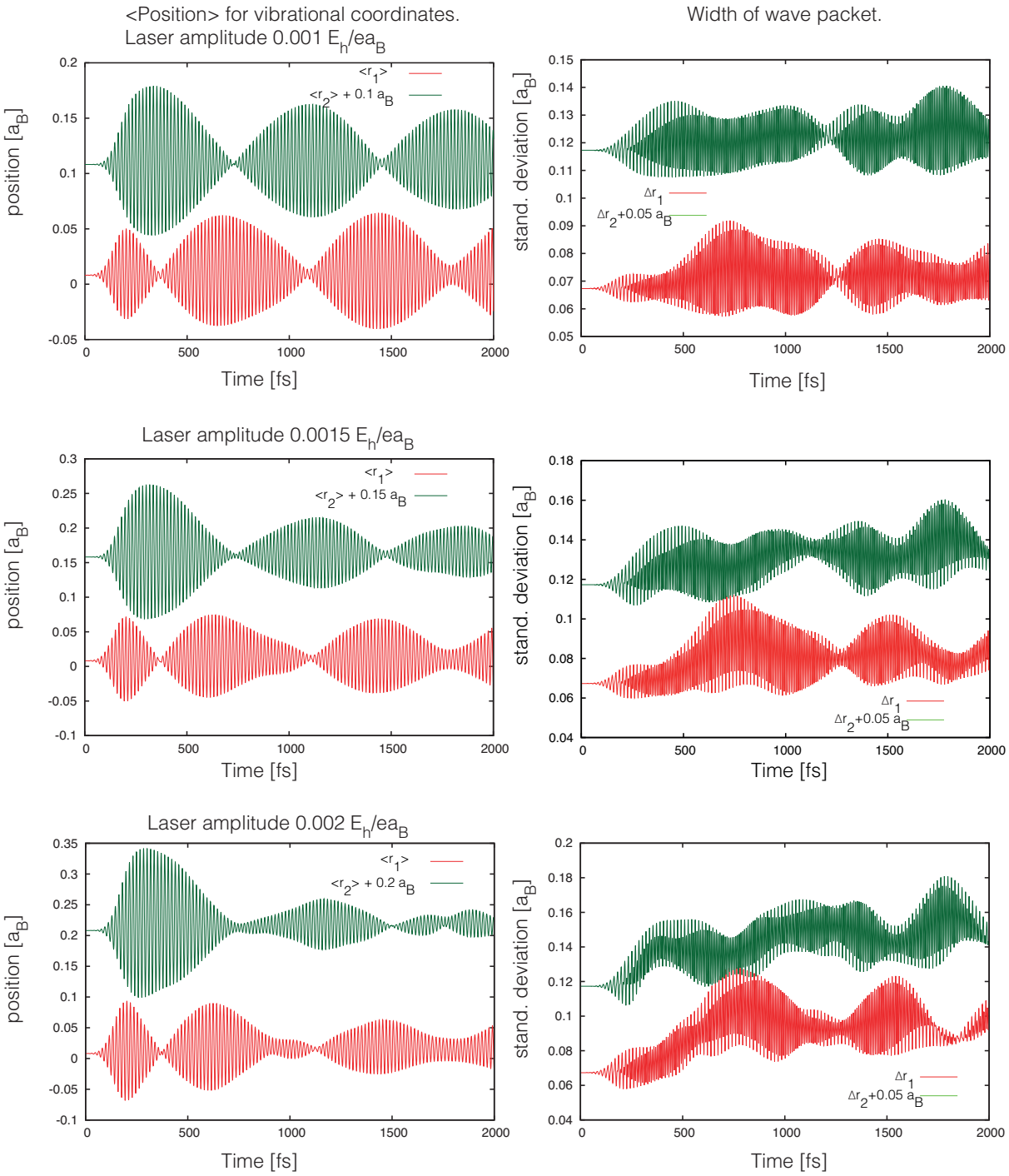

Figure 3.18: Position expectation values and standard deviation of the wave packet for r_1 and r_2 degrees of freedom for three different field amplitudes. The phase between the pulses is 180 degrees.

An interesting situation appears when increasing the field amplitude significantly, such as $E_0 = 0.005$ E_h/ea_B. One might argue that this would be a prerequisite for bond breaking. It can be seen in Fig. 3.19, that the oscillation picture breaks down completely for $\Delta\phi = 0$ (middle-left panel) and $\Delta\phi = 180$ (middle-right panel). The widths of the wave packets increase dramatically, which can be seen in the lower panels of this figure. In the upper-right panel the laser pulse is shown. The width of the pulse is $\tau = 75$ fs. In the upper-left panel the expectation value of the Hamiltonian is presented. The energy absorb by the system is around 12 000 cm^{-1}. The energy is below the dissociation energy that is around 20 000 cm^{-1}. From the Fig. 3.20 one can see that the dissociation coordinates are not elongated enough to have dissociation. The width of the wave packet increases during the simulation.

Next we investigate what will occur if the pulse will be longer than the "switching" time? For this simulation the results are shown in Fig. 3.21. The width of the pulse is $\tau = 500$ fs and its amplitude is $E_0 = 0.0001$ E_h/ea_B. In the middle panels it can be seen that slow oscillations appear when the laser pulse starts to act, for $\Delta\phi = 0$ (left panel) and $\Delta\phi = 180$ (right panel). The width of the wave packet is on average constant during the simulation, shown in the lower panels. The energy absorbed by the system is around 250 cm^{-1} as can be seen in the upper-left panel and in the right panel the pulse itself. Qualitatively the oscillation behavior does not depend on the pulse width, but it depends on the two laser pulses that excite the two states. One pulse is resonant to one transition and the second pulse is resonant to the second transition. The pulses create a superposition of this two states that is, however, not an eigenstate of the system.

Another question is whether the phase between the pulses is $\Delta\phi = 90$ degrees. Will the circular motion of the wave packet be present as in Ref. [38]? The results for the simulations with the circularly polarized light are shown in the Fig. 3.22 (left panels). The wave packet still exhibits the switching behavior. The reason is that for $Mn_2(CO)_{10}$ due to symmetry there are vibrations which have dipole moments in X and Y direction. In contrast, each vibration in the present case, is associated with a particular direction of the dipole. The amplitude of the pulse is $E_0 = 0.001$ E_h/ea_B and width $\tau = 75$ fs. The width of the wave packet (middle panels) is not increasing significantly. The energy absorb by the system is around 550 cm^{-1}, as shown in the lower panels. A similar situation occurs when the phase will be changed to $\Delta\phi = 45$ degrees (right panels).

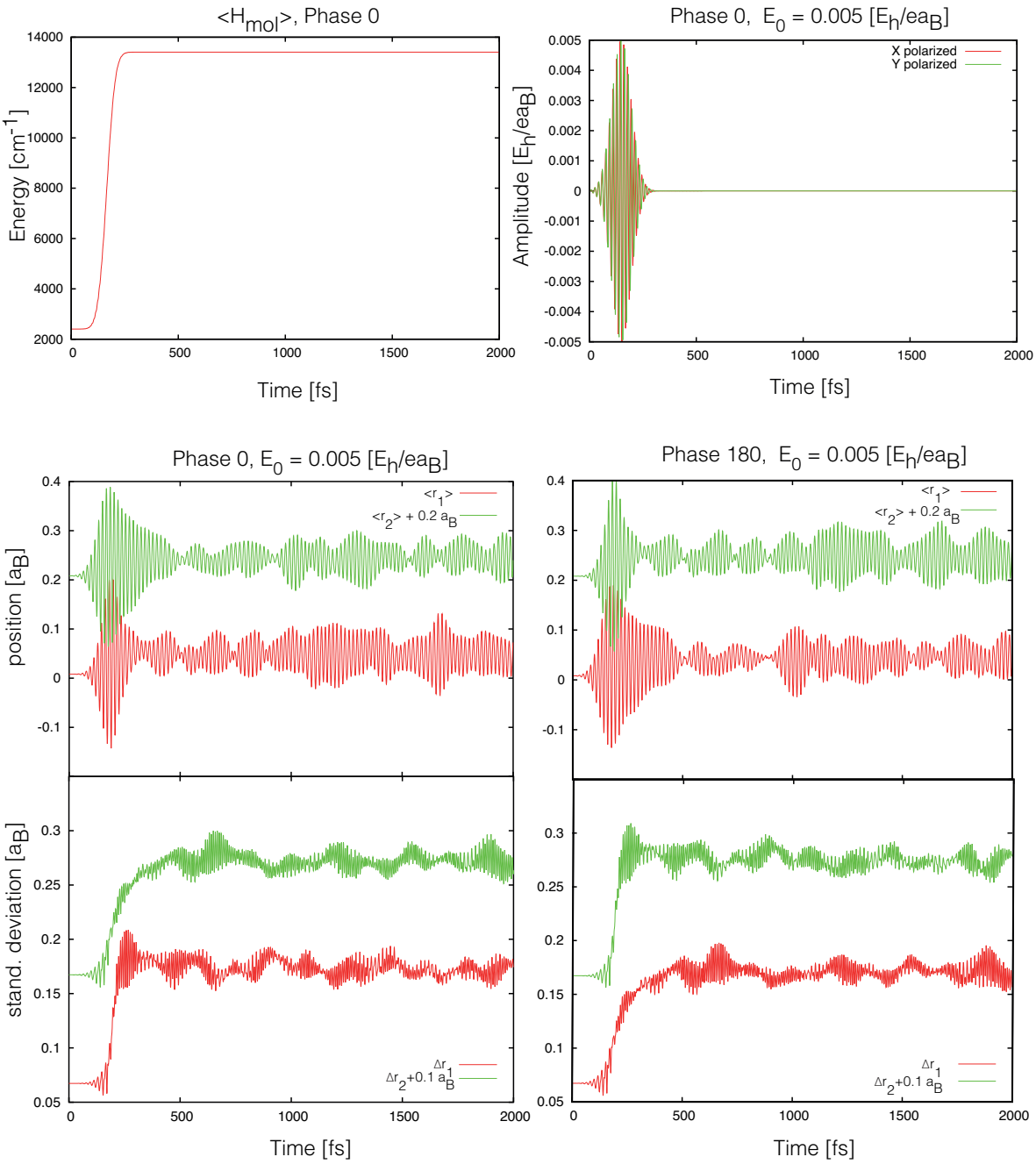

Figure 3.19: Position expectation values and standard deviation of the wave packet for r_1 and r_2 degrees of freedom for strong laser pulse with amplitude $E_0 = 0.005$ $\mathrm{E_h/ea_B}$. Phase between pulses is zero (left) and 180 degrees (right). The upper-left panel shows the expectation value of the system Hamiltonian for phase zero and on the right the laser pulse with the same phase and width $\tau = 75$ fs.

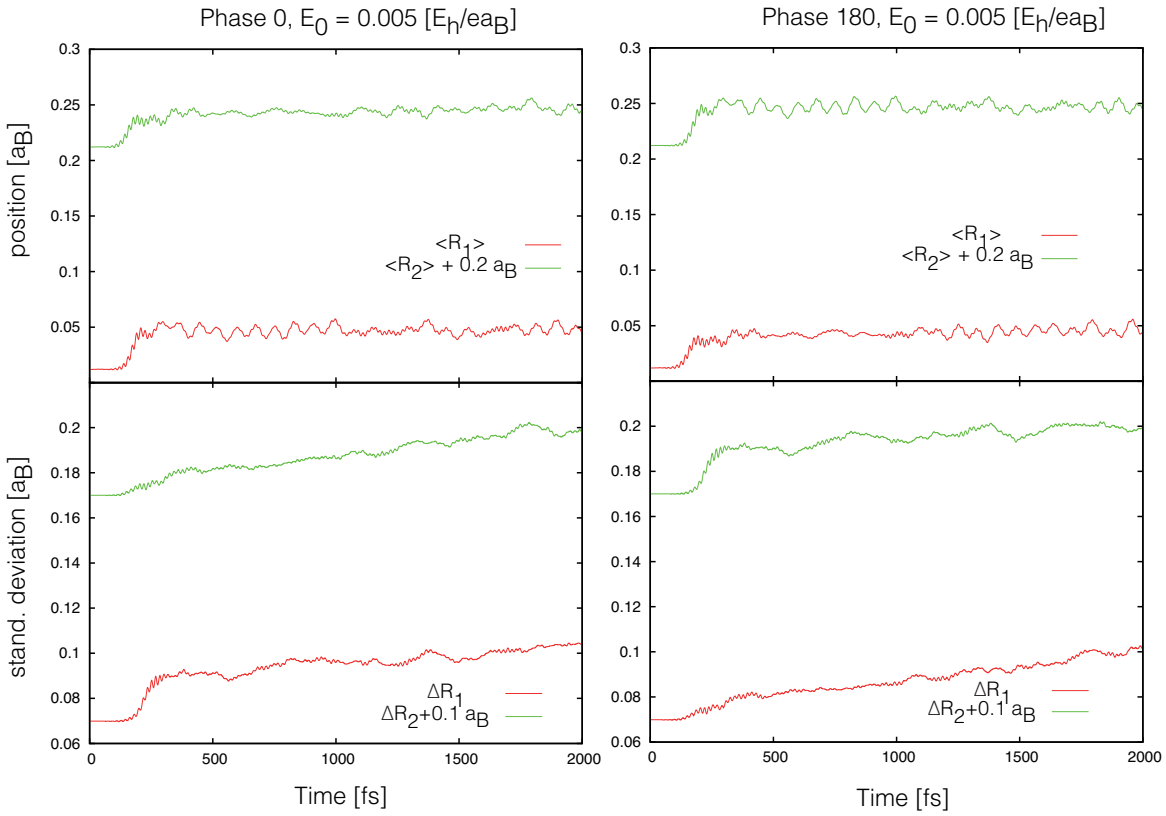

Figure 3.20: Position expectation values and standard deviation of the wave packet for R_1 and R_2 degrees of freedom for strong laser pulse with amplitude $E_0 = 0.005$ $\mathrm{E_h/ea_B}$. Phase between pulses is zero (left) and 180 degrees (right). No dissociation has been observed.

For the experimental setup it is more convenient to choose the frequency of the laser field that is not in the resonance with the vibrational transitions, but is in the middle of the symmetric and antisymmetric vibrations, i.e. $\omega = 1943$ cm^{-1}. The results for this simulations are shown in Figs. 3.23 and 3.24 for phase $\Delta\phi = 0$ degrees and $\Delta\phi = 180$ degrees, respectively. The simulations do not differ much from the ones with frequencies chosen to be approximately in resonance with symmetric and antisymmetric carbonyl vibrations. But when we take the longer pulse such as in the Fig. 3.25 and compare to the Fig. 3.21 we see a difference. The stimulated emission, that can be seen in the upper-left panel, is because the pulses that excite the vibrational transitions are not in resonance with these transitions.

In this section it has been shown, how to excite local bond vibrations. However, this method works for weak fields only. Thus, the excitation is not sufficient to enable bond breaking. But, one might ask what are the conditions for bond breaking in this molecule within the reduced dimensional model. This question is addressed in the next section.

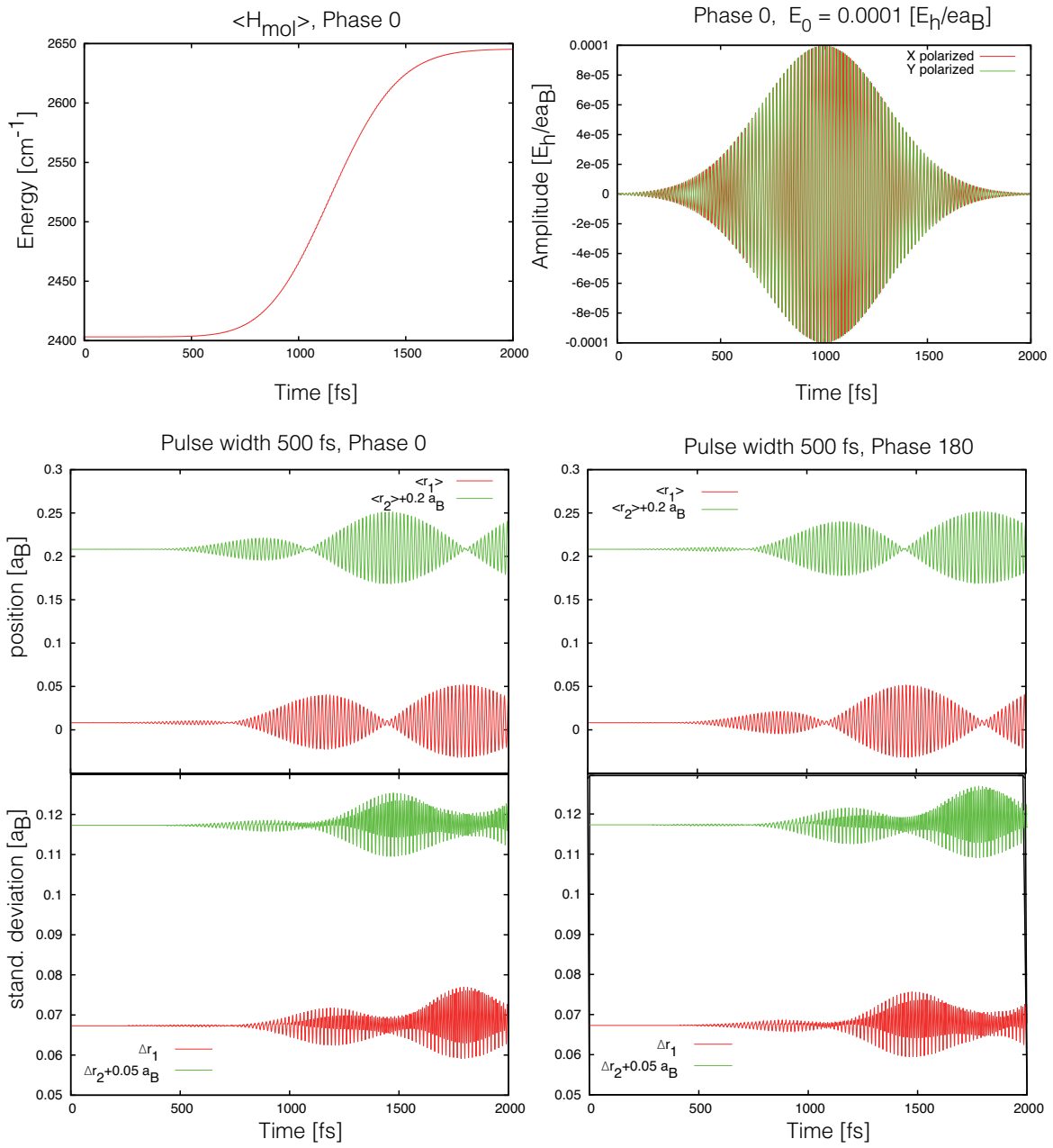

Figure 3.21: Position expectation values and standard deviation of the wave packet for r_1 and r_2 degrees of freedom for weak but long laser pulse with amplitude $E_0 = 0.0001$ $\mathrm{E_h/ea_B}$ and $\tau = 500$ fs. Phase between the pulses is zero (left) and 180 degrees (right). The upper-left panel illustrates the expectation value of the system Hamiltonian for phase zero. On the right the laser pulse with the same phase itself is given.

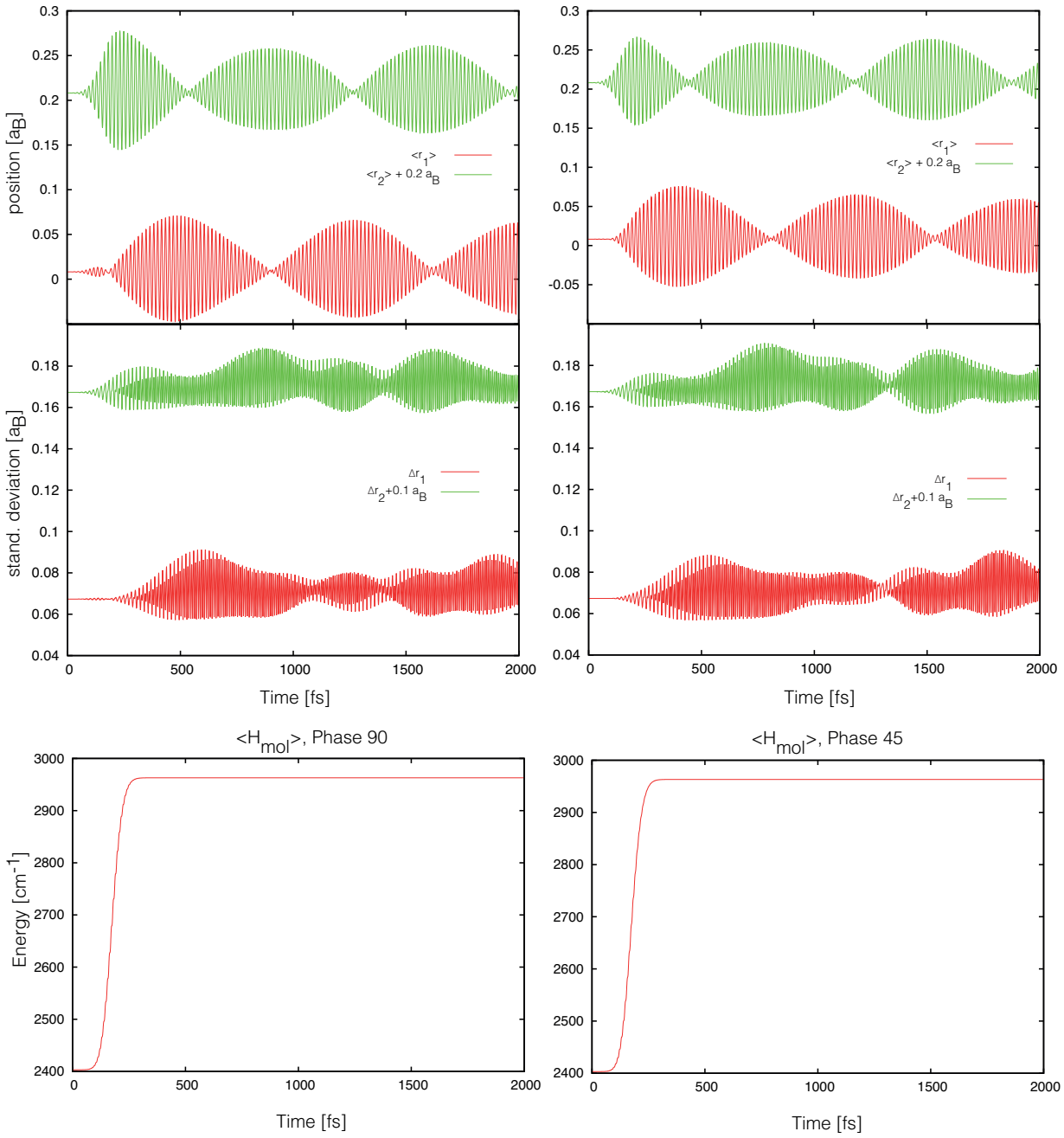

Figure 3.22: Position expectation values and standard deviation of the wave packet for r_1 and r_2 degrees of freedom for laser pulse with amplitude $E_0 = 0.001$ $\mathrm{E_h/ea_B}$ and $\tau = 75$ fs. Phase between the pulses is 90 degrees (left) and 45 degrees (right). Lower panels show the expectation value of the system Hamiltonian for phase 90 degrees (left) and 45 degrees (right).

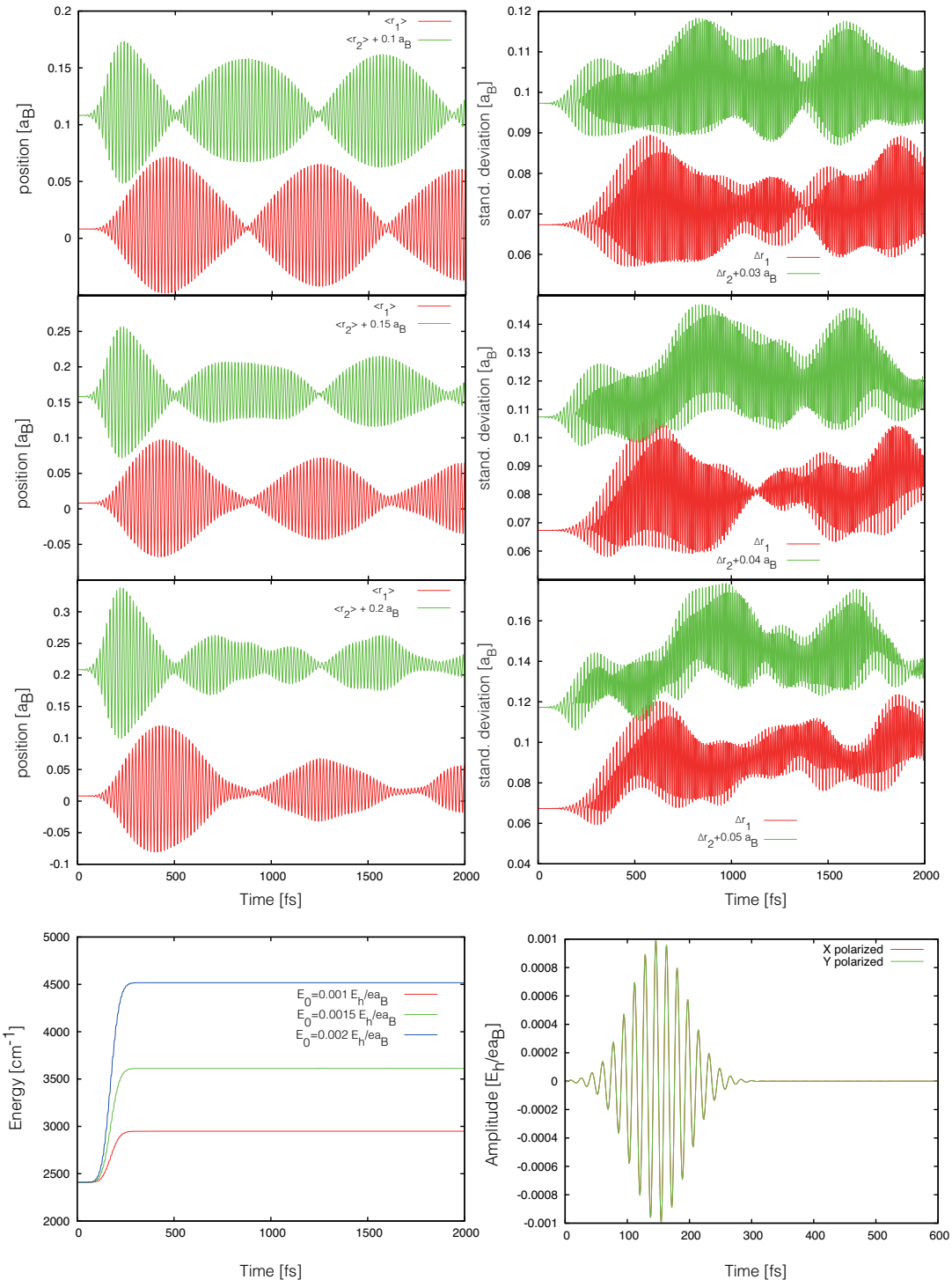

Figure 3.23: Position expectation values and standard deviation of the wave packet for r_1 and r_2 degrees of freedom for three different field amplitudes $E_0 = 0.001$ $\mathrm{E_h/ea_B}$, $E_0 = 0.0015$ $\mathrm{E_h/ea_B}$ $E_0 = 0.002$ $\mathrm{E_h/ea_B}$. The lower-left panel shows the expectation values of the system Hamiltonian and on the right the laser pulses with phase between them equal zero, but the frequency is not in resonance with any of the two distinct transitions, but in the middle, $\omega = 1943$ $\mathrm{cm^{-1}}$ and width is $\tau = 75$ fs.

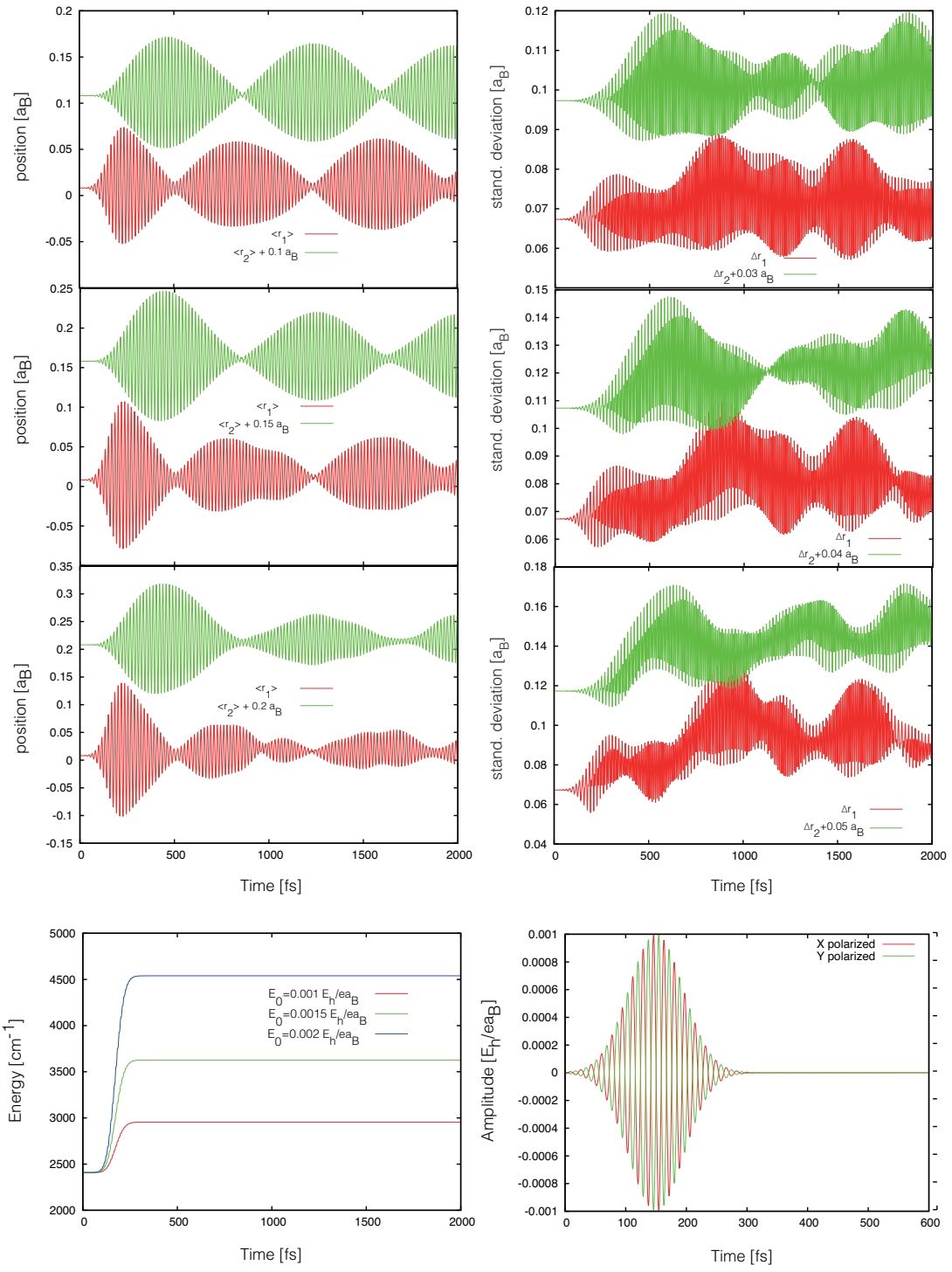

Figure 3.24: Position expectation values and standard deviation of the wave packet for r_1 and r_2 degrees of freedom for three different field amplitudes $E_0 = 0.001$ $\mathrm{E_h/ea_B}$, $E_0 = 0.0015$ $\mathrm{E_h/ea_B}$ $E_0 = 0.002$ $\mathrm{E_h/ea_B}$. The lower-left panel shows the expectation values of the system Hamiltonian and on the right the laser pulses with phase between them equal 180 degrees, width is $\tau = 75$ fs, and frequency is $\omega = 1943$ $\mathrm{cm^{-1}}$.

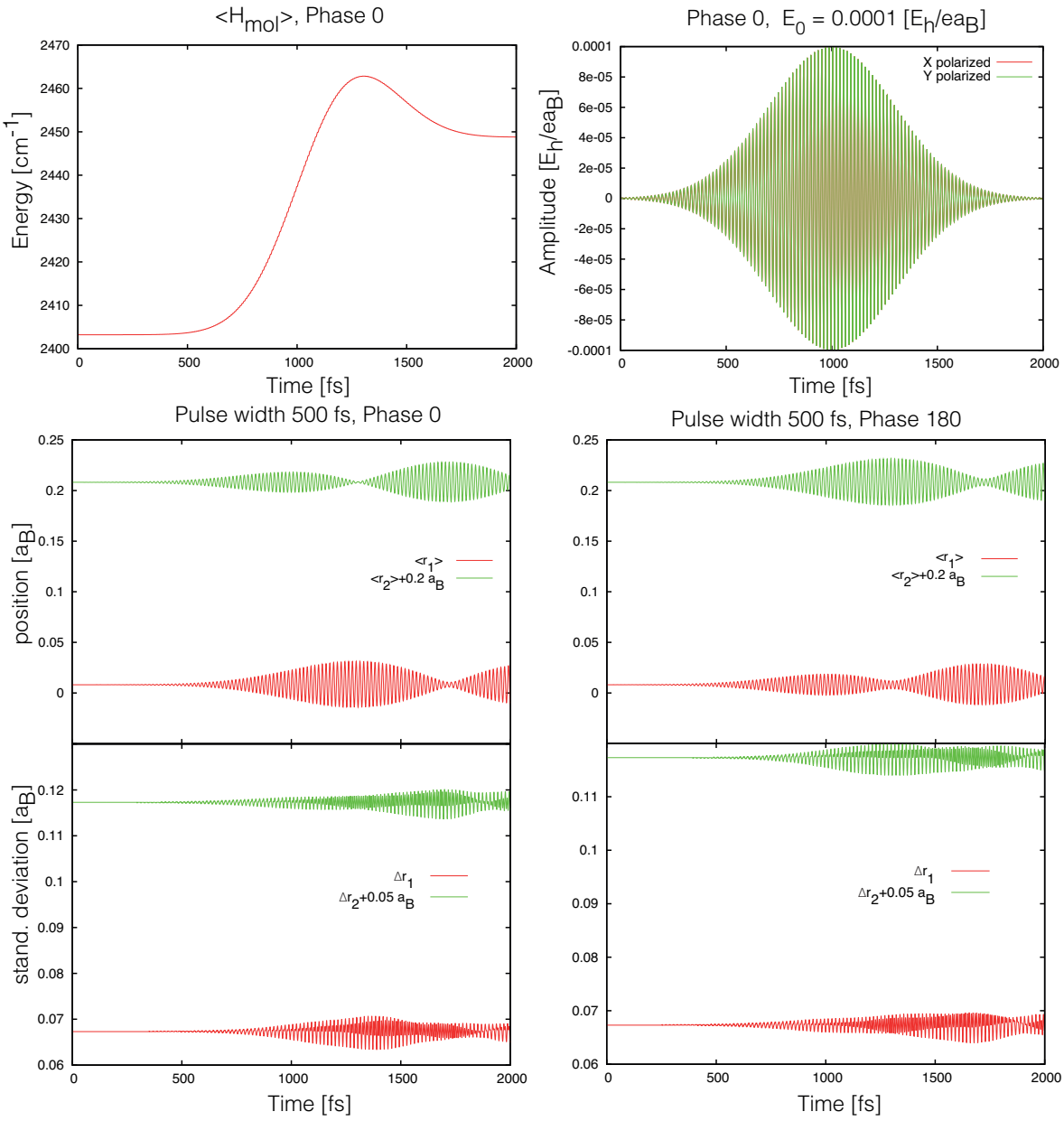

Figure 3.25: Position expectation values and standard deviation of the wave packet for r_1 and r_2 degrees of freedom for field amplitude $E_0 = 0.0001$ $\mathrm{E_h/ea_B}$, for phase zero (left) and 180 degrees (right). The upper-left panel shows the expectation values of the system Hamiltonian and on the right the laser pulses with phase between them equal 0 degrees, width is $\tau = 500$ fs, and frequency is $\omega = 1943$ $\mathrm{cm^{-1}}$.

3.8 Exploring the PES

In section 3.6 the possibility of bond breaking has been studied by using linearly-polarized light. The reaction yields were very low. One of the reasons is that the energy is deposited over many bonds within the molecule. To focus it into a single bond one may use a two pulse scheme with a *relative* phase as done in the previous section. Here we address the question, what are possible conditions for bond breaking within 4D model. In the following section, the ground state wave packet will be initially displaced on the PES and propagated freely without any electric field. Its center will be at the positions given by the dots in Fig. 3.16, upper panels. These points have been chosen such that the expectation value of the energy is slightly above the dissociation energy, i. e. 20 970 cm^{-1} (2.6 eV). To see the equilibrium values for position and standard deviation check Table 3.2.

In the upper-left panel of the Fig. 3.16 the vibrational surface is presented. The blue dot shows the position of the center of the ground state wave packet shifted in r_1 coordinate to the place where r_1=0.55 a_B and r_2 coordinate was kept in the equilibrium position. The resulting reaction yield, defined in Eq. (3.6) and presented in the Fig. 3.26, is rather low on the time scale of 2 ps. In particular, it is not larger than $\sim 10^{-5}$ in R_1 exit channel and is negligible in R_2 exit channel. In the lower panels the position expectation values for r_1 and R_1 coordinates are presented on the left and their standard deviations on the right. It can be noticed that the standard deviation of the vibrational coordinate initially increases in time and later stays on average constant.

The yellow dot on the vibration surface (Fig. 3.16) presents the initial position of the wave packet shifted to r_1=r_2=0.35 a_B coordinates. The reaction yield is shown in Fig. 3.27 in the upper panel and as before it is not larger than $\sim 10^{-5}$. Yield for the R_2 channel is higher than for the R_1 channel, because PES for r_2 coordinate is more flat than for the r_1 coordinate. That is why, when comparing the position expectation value for the wave packet, one can see that it stays more often in the region where $r_2 > r_1$. In the lower panel the position expectation values for vibrational coordinates are shown on the left and their expectation values on the right. In Fig. 3.28 the position expectation values (left) and their standard deviations (right) are shown for r_1-R_1 coordinates (top) and r_2-R_2 coordinates (bottom) panels. It can be seen that the wave packet along R spreads such that oscillations disappear in $\langle R \rangle$.

In the upper-right panel of Fig. 3.16, on vibration-dissociation PES for r_1-R_1 coordinates, the blue dot represents the position of the ground state wave packet shifted to r_1=0.5 a_B and R_1=-0.1 a_B coordinates. The displacement along the Co-CO R_1 bond coordinate increases the yield by a factor of two. There is no yield for the R_2 exit channel. It is shown in Fig. 3.29 in the upper panel. In the lower panel the position

expectation values are shown for this mixed coordinates and standard deviations on the left and right, respectively.

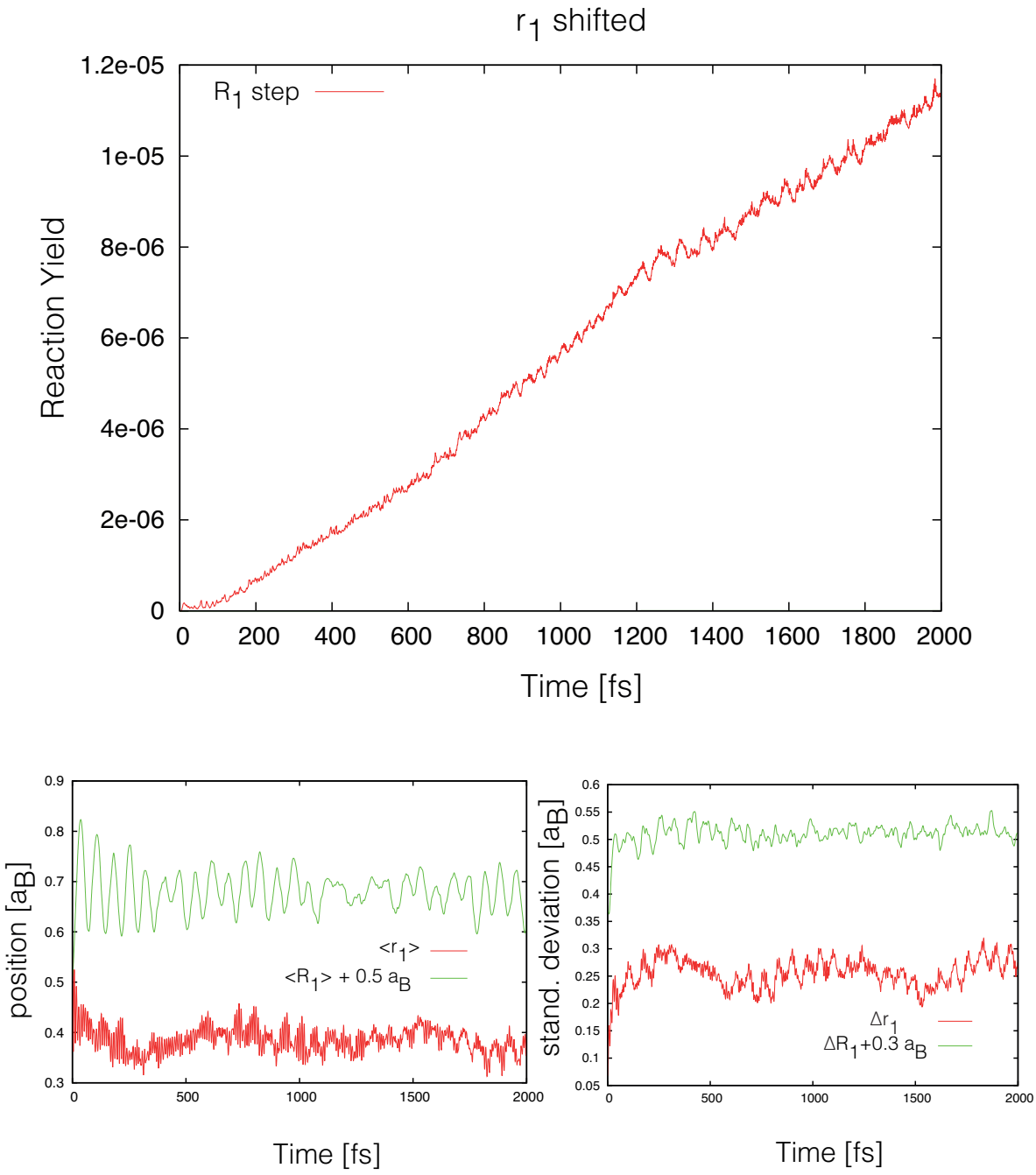

Figure 3.26: Reaction yields are shown in the upper panel. In the lower panels position expectation values for r_1 and R_1 coordinates are presented on the left and their standard deviation on the right. Initially, r_1 coordinate was shifted to r_1=0.55 a_B. After 2 ps the width of the distribution of the vibrational coordinate stays on average constant. Values for dissociation coordinate are shifted by 0.5 a_B (left) and 0.3 a_B (right) for clarity. 10 SPFs were used for convergence and maximum population of the least occupied SPF was $< 0.1\%$.

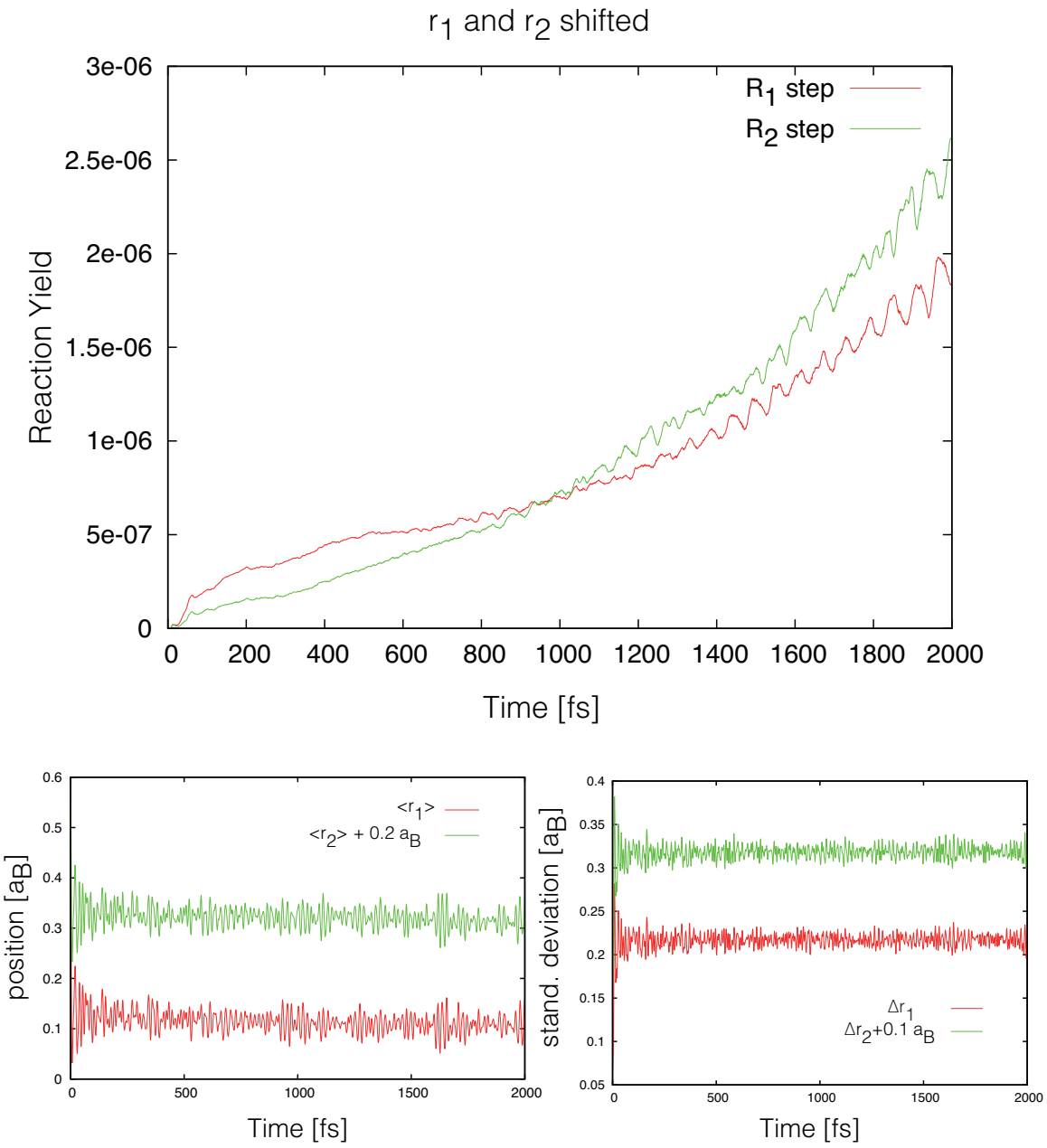

Figure 3.27: In the upper panel reaction yields for two exit channels are presented. In the lower panels the position expectation values for r_1 and r_2 coordinates are shown on the left and standard deviations on the right. Initially, wave packet was shifted to r_1=r_2=0.35 a_B. Values for r_2 coordinate are shifted by 0.2 a_B (left) and 0.1 a_B (right) for clarity. 25 SPFs were used and maximum population of the least occupied SPF was about 0.4%.

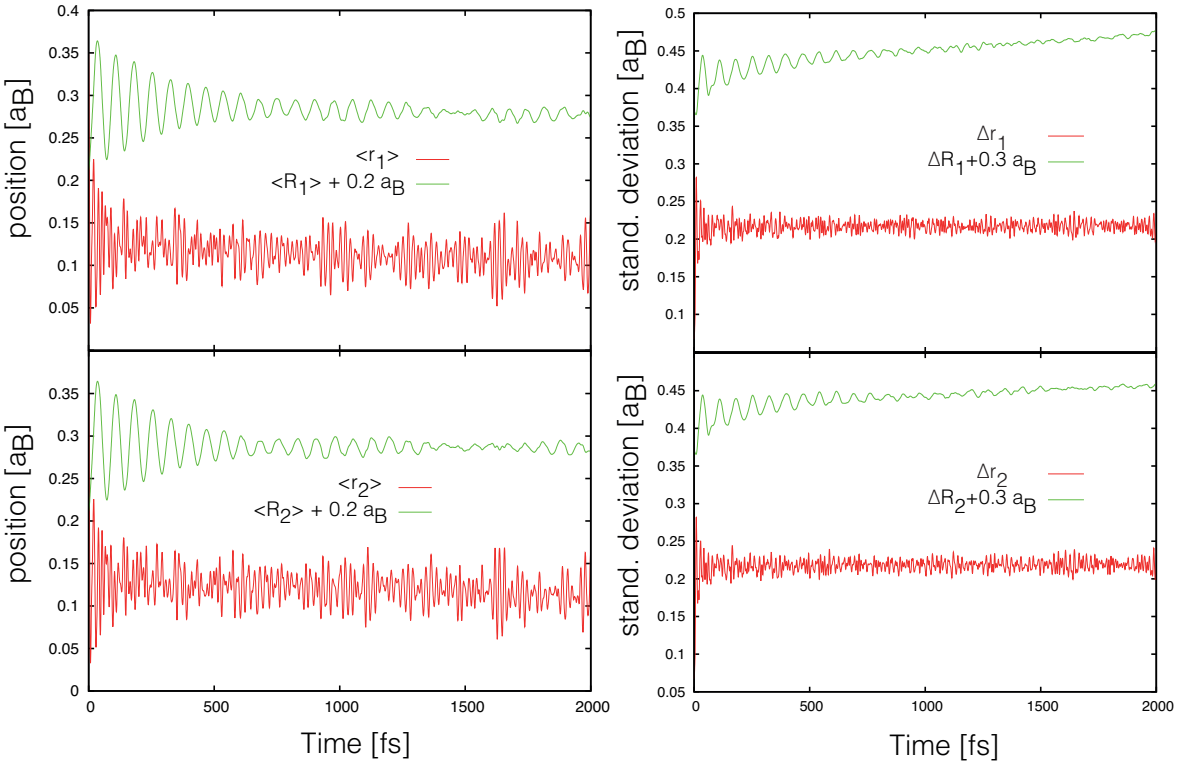

Figure 3.28: Position expectation values and standard deviation for the mixed coordinates r_1-R_1 (top) and r_2-R_2 (bottom) for situation of Fig. 3.27. Values for dissociation coordinates are shifted by 0.2 a_B (left panels) and by 0.3 a_B (right panels) for clarity.

The yellow dot on the vibration-dissociation surface of Fig. 3.16 shows the position of the ground state wave packet shifted to R_1=-0.625 a_B. The r_1 coordinate was kept at the equilibrium position. This extreme compression of the Co-CO R_1 bond gives an appreciable reaction yield of $\sim 10^{-2}$. There was no yield observed for R_2 exit channel. This is shown in the Fig. 3.30 in the upper panel. In the lower panel the position expectation values for these mixed coordinates are shown on the left and their standard deviations on the right. It should be emphasized that the width of the dissociation coordinate increases remarkably. Initially, the wave packet moves towards the repulsion PES in the r_1-R_1 plane (see Fig. 3.16). The backscattering is such that most kinetic energy will go into the bond vibration coordinate (see Fig. 3.31). According to the figure the partitioning of the kinetic energy is such that the most of it is localized in the r_1 coordinate. Therefore, only little dissociation is observed.

In conclusion, the reaction yield is rather low on the time scale of 2 ps, i.e similar to the case of the carboxymyoglobin model of Ref. [26]. In particular, excitation of the carbonyl stretching coordinates, regardless of whether it is localized (Fig. 3.26) or collective (Fig. 3.27) doesn't lead to a yield larger than $\sim 10^{-5}$. Simultaneous displacement along the Co-CO bond coordinates (Fig. 3.29) increases the yield by a factor of two. In fact, only an extreme compression of the Co-CO bond (Fig. 3.30)

does give an appreciable reaction yield of about $\sim 10^{-2}$. However, apart from the experimental constraints, driving the metal-carbonyl bond could be complicated by the fact, that in this spectral range, modes that are not part of the present model would influence the dynamics, e.g., via IVR processes.

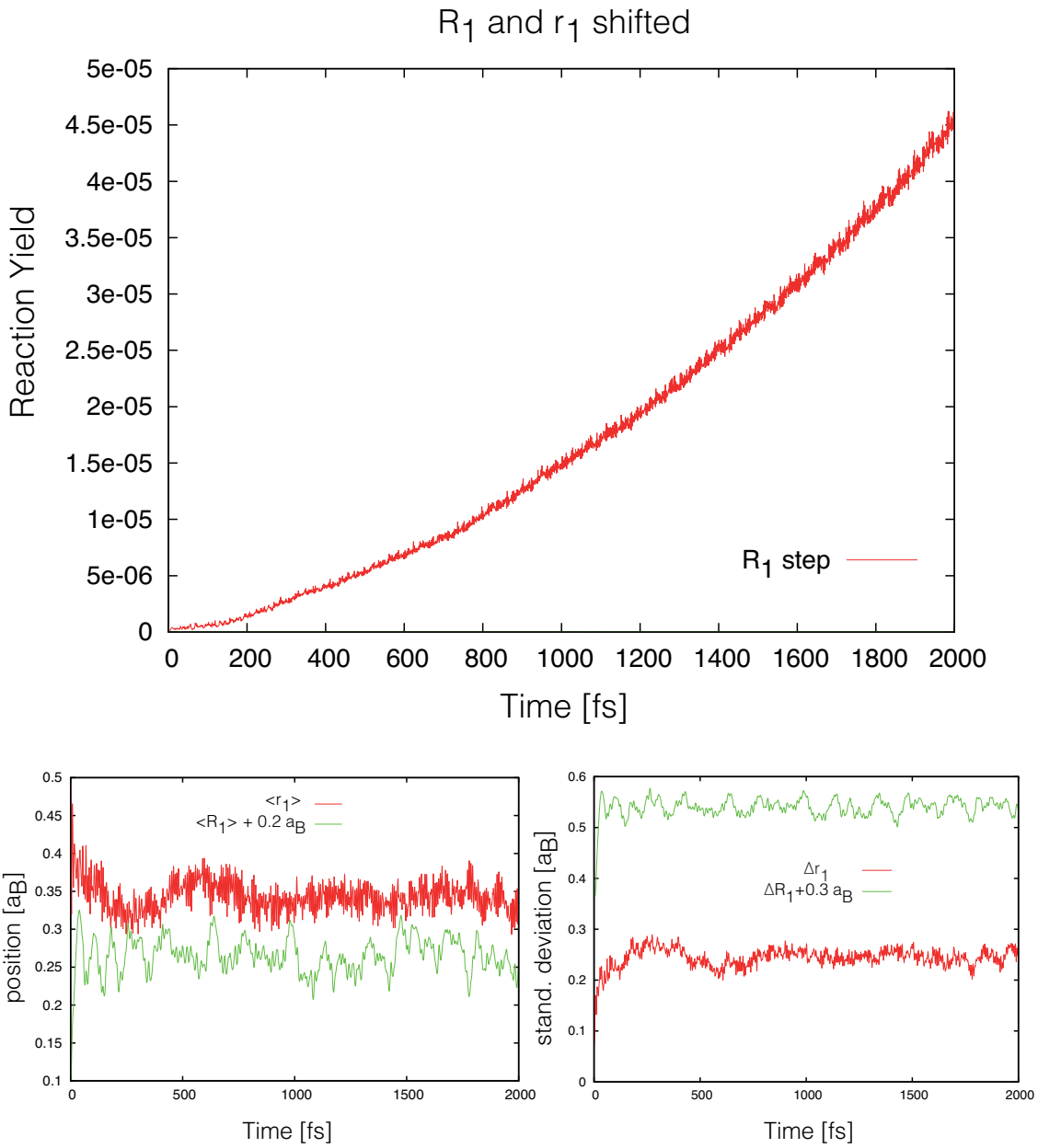

Figure 3.29: Reaction yields are shown in the upper panel. Displacement along Co-CO, R_1 coordinate, enhances yield. In the lower panels the expectation values for the position are shown (left) and their standard deviation (right). Initially wave packet was shifted to r_1=0.5 a_B and R_1=-0.1 a_B. Values for dissociation coordinate are shifted by 0.2 a_B (left) and 0.3 a_B (right) for clarity. 12 SPFs were used and maximum population of the least occupied SPF was $< 0.1\%$.

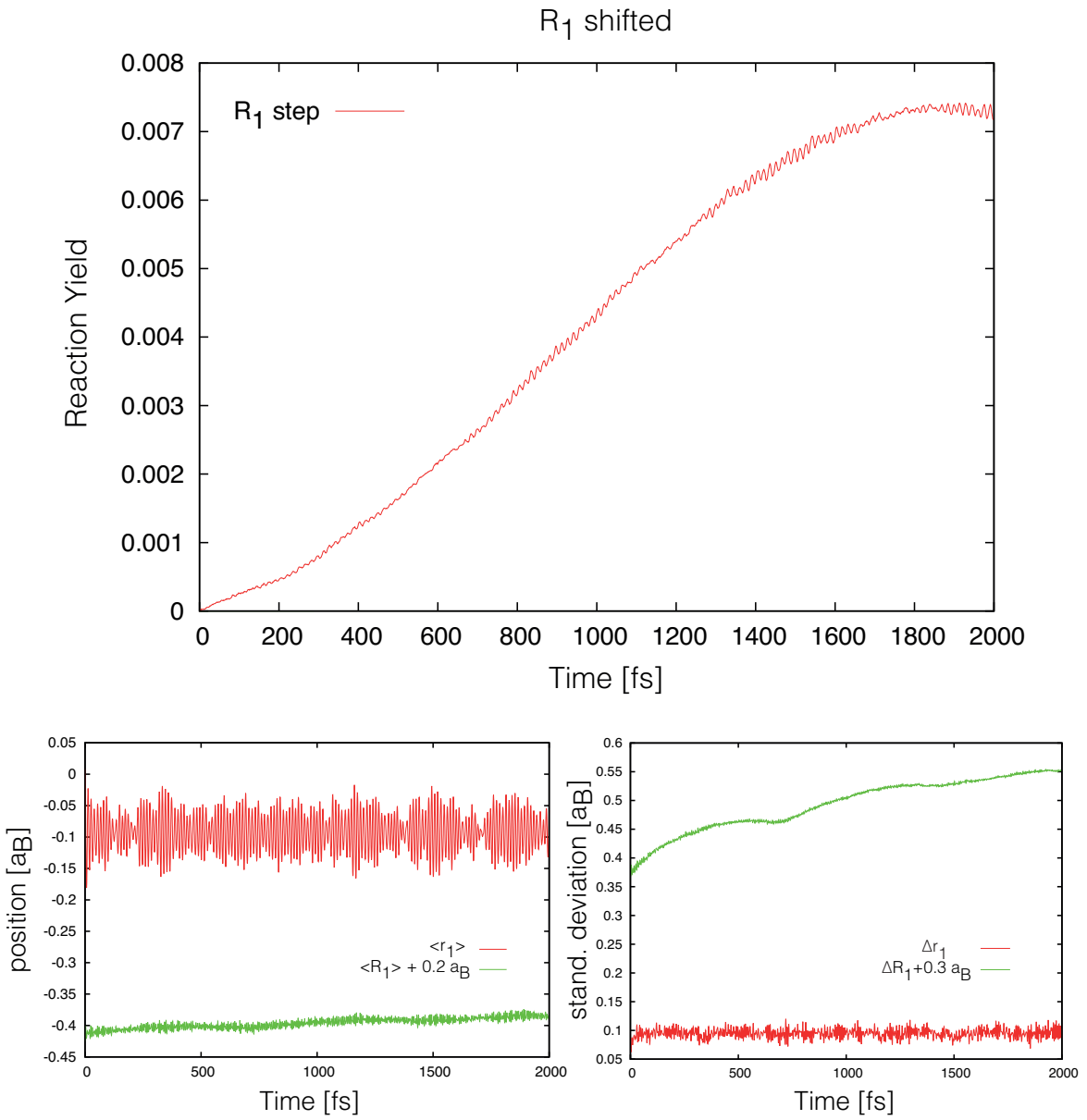

Figure 3.30: In the upper panel reaction yield reached up to $\sim 10^{-2}$. Extreme Co-CO bond compresion in R_1 coordinate gives appreciable yield. In the lower panels position expectation values are shown (left) and their standard deviation (right). Values for dissociation coordinate are shifted by 0.2 a_B (left) and 0.3 a_B (right) for clarity. Initially wave packet was shifted to R_1=-0.625 a_B. 8 SPFs were used and maximum population of the least occupied SPF was $< 0.1\%$.

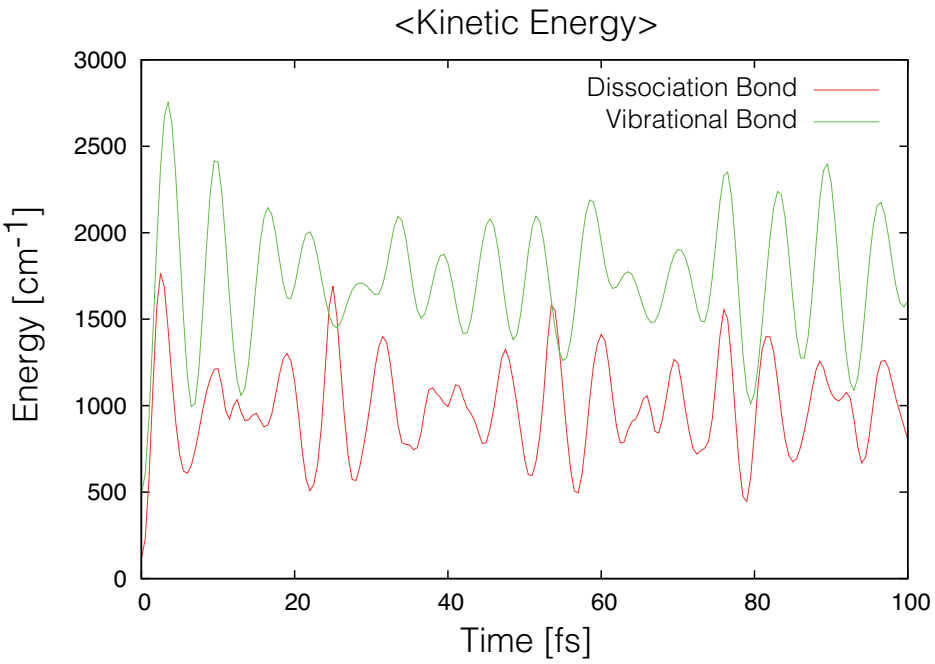

Figure 3.31: Kienetic energy expectation values for bond dissociation coordinate R_1 and bond vibration coordinate r_1 for situation of Fig. 3.30.

3.9 Summary

In this chapter, a model dicarbonyl complex $CpCo(CO)_2$ has been studied. The electronic structure calculations have been done at DFT/B3LYP/LanL2DZ level of theory. 4D surfaces were created in order to describe metal-carbonyl bonds dissociation and carbonyl vibrations. Laser driven quantum dynamics has been simulated using the MCTDH method. From quantum dynamics simulations anharmonic IR spectra were determined for metal-carbonyl and carbonyl vibrations.

The possibility of bond breaking has been studied by linearly-polarized laser pulses. Although much energy has been given to the system the bond breaking was impossible due to insufficient anharmonic coupling between Co-CO and C-O coordinates.

Following, the focus was placed on the local coordinate oscillations. Given a pair of IR active symmetric and antisymmetric stretching vibrations, a superposition state was excited, which corresponded to an alternating oscillation along local bond stretching coordinate. This was achieved by choosing the relative phase between two overlapping pulses. However, the efficiency of this process diminishes with increasing excitation level due to the anharmonicity leading to wave packet dispersion.

The simple pulse scheme is not suitable for strong excitation of a local CO bond, such that IVR can cause dissociation of the neighboring metal-carbonyl bond. Whether more complicated pulse forms (see e.g. Ref. [37]) can achieve the goal of keeping wave

packet compact even at high energies remains to be shown. In this respect instantaneous displacement of a ground state wave packet has been performed in order to examine the general possibility of bond breaking. However the result was negative except for unrealistic strong dissociation coordinate compression. Thus we conclude that $CpCo(CO)_2$ appears to be another example where non-statistical metal-carbonyl bond breaking cannot be achieved by a reasonable IR excitation of the carbonyl stretching vibrations.

Chapter 4

Alcoholysis of Isocyanates

4.1 Introduction

The general reaction scheme for alcoholysis of isocyanates to urethane can be seen in Sec. 1.2. In the present work the focus is on the identification of educts and products of the thermally driven reaction by means of IR absorption spectroscopy. Performing temperature-dependent experiments it was possible to obtain Arrhenius activation energies [84]. To connect the activation energies with molecular motions the IRC can be investigated. The IRC is a path downhill from a saddle point to the minimum [56]. In the following two reactions were considered: phenylisocyanate (PIC) with cyclohexanol (**I**) and TDI with chloraldhydrate (**II**), but only for latter case the IRC path was calculated because only this reaction can lead to polyurethane formation. However, reaction **I** involves the same initial steps, cf. Fig. 1.2, but in contrast to **II** a different marker band has to be used to extract the Arrhenius activation energy.

We start with a literature review on quantum chemical studies of alcoholysis reactions. The alcoholysis reaction of several aromatic diisocyanate molecules with n-butanol has been studied theoretically by Çoban and Konuklar using density functional theory with the B3LYP functional and a 6-31+G(d,p) basis set [85]. This work confirmed the concerted pathway (C=N addition) yielding s-trans-urethane via a four member transition state with an O-H-N hydrogen bond. For the particular case of 2,4-toluene-diisocyanate the reaction barrier (free energy difference in harmonic approximation) with respect to the separate reactants was found to be 40.1 kcal/mol in gas phase and 29.5 kcal/mol in benzene. The effect of the solvent had been included via the polarizable continuum model (PCM). In this model the solvent has macroscopic dielectric properties and is described by the dielectric constant ε [46]. The addition reaction of ethylene glycol with TDI and other diisocyanates was investigated in Ref. [86] using the DFT/B3LYP/6-311+G(d,p) level of theory in gas phase and PCM benzene.

Here, a multi-step addition (C=O) approach had been in the focus with the first step having a free energy of activation of 63 kcal/mol. These authors also performed an investigation of the basis set dependence of the binding free energy, concluding that the minimal requirement is a triple zeta basis including polarization and diffuse functions. They also pointed to the differentiation with respect to the addition at the second isocyanate group that has lower reactivity due to a substitution effect.

In general the reported values for free energies of activation appear to be rather large as compared to experimentally-determined Arrhenius activation energies, which are for polyols with mono- and diisocyanates in between 5 and 11 kcal/mol [87, 88]. Experimental values for phenylisocyanates in benzene range from 9-12 kcal/mol [89] and are found to be 4.4 kcal/mol in p-dioxane [90]. A similar value of 9.3 kcal/mol was obtained from a Raman study of 4,4'-diphenyl-methane diisocyanate and 1,4-butanediol in hydroxyl terminated poly(butylene adipate) [91]. Recent experiments on phenylisocyanate with cyclohexanol and 2,4-toluene-diisocyanate with chloralhydrate gave the values of 6.7 ± 0.2 kcal/mol and 2.8 ± 0.3 kcal/mol, respectively [84]. An explanation of this discrepancy between experiment and theory has been proposed by Raspoet and co-workers [92]. Based on concentration dependent kinetic studies it was concluded that more than one alcohol participates in the reaction with isocyanate and that the additional alcohol molecules serve as a catalyst. In fact second-order Møller-Plesset (MP2)/6-311++G(d,p)/PCM calculations for HN=C=O+$n$$CH_3OH$ reactions showed a decrease of the free energy of activation from 31 kcal/mol ($n = 1$) to 9.5 kcal/mol ($n = 3$). Note, however, that this comes at the expense of an increasingly complicated reaction path, including several minima and transition states that might be strongly affected by the interaction with a solvent. A similar conclusion was reached by Samuilov and co-workers in a series of papers (see, e.g., Ref. [93] for reaction of phenyl isocyanate with methanol associates). Notice that here also a pre-reaction (encounter) complex is discussed, whose stability decreases for larger methanol associates. Most recently, Wang et al. investigated the reaction of TDI with methanol using DFT/B3LYP/6-311G(d,p) confirming the acceleration due to what was termed a proton transporter mechanism in the presence of an additional methanol. Reported values for activation free energies in gas phase are 39 kcal/mol (single methanol) and 25 kcal/mol (methanol dimer) [94].

4.2 IR spectroscopy and reaction rates

4.2.1 Equilibrium Structures

Optimized gas phase structures at stationary points corresponding to educts and products are shown in Fig. 4.1. Quantum chemical geometry optimisations have been per-

formed for educts and products of reactions **I** and **II** in gas phase using DFT/B3LYP with the 6-31++G(d,p) basis set as implemented in Gaussian 09 [55]. IR absorption spectra were calculated employing anharmonic corrections to the harmonic frequencies and intensities as detailed in Ref. [95]. In both cases the educts are actually not the separeated reactants but Hydrogen-bonded encounter complexes.

In **Ia** a nonlinear O-H$\cdots$N Hydrogen bond exists with a bond length of 3.19 Å and angle of 158°. In the product state (**Ib**) this Hydrogen bond is broken and the C-O bond formed instead. The C-O distance changes from 3.91 Å (**Ia**) to 1.22 Å (**Ib**).

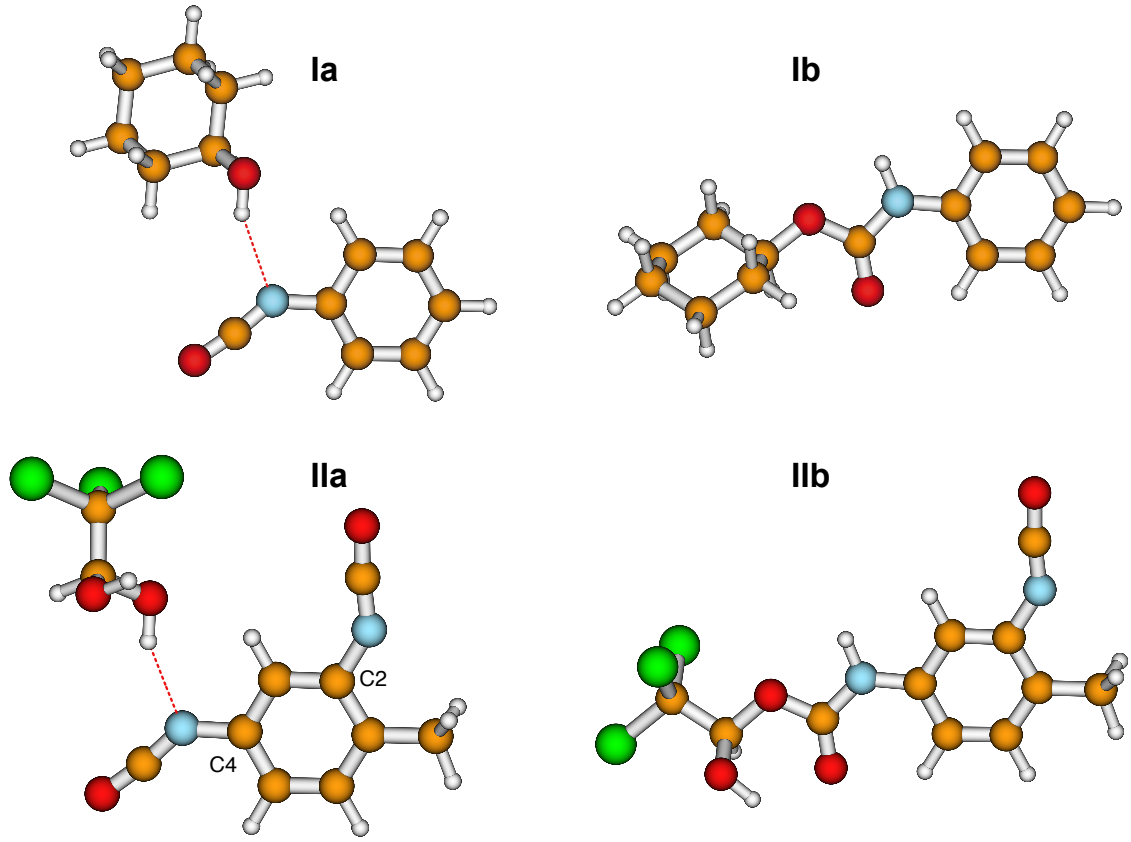

Figure 4.1: Optimized gas phase geometries (DFT/B3LYP/6-31++G(d,p)) for educts (a) and products (b) of reactions **I** and **II**.

Concerning reaction **II** only the C4 position is considered, whose reactivity is 1.5 to 3 times higher than for the C2 position due to sterical hindrance by the methyl group [85]. In **IIa** a nonlinear O-H$\cdots$N Hydrogen bond exists with a bond length of 3.03 Å and angle of 156°. In the product state (**IIb**) this Hydrogen bond is broken and the C-O bond formed instead. The C-O distance changes from 3.78 Å (**IIa**) to 1.37 Å (**IIb**).

4.2.2 Monitoring the Reactions by IR Spectroscopy

Reaction I

The experimental spectra at preparation time as well as after 180 minutes are dominated by a strong NCO-absorption around 2270 cm^{-1}. The sample was freshly prepared at room temperature with filtered PIC and was filled in a CaF_2 cuvette [84]. Due to the high concentration the absorption is saturated such that this band is not suitable for further analysis. The respective spectra in the fingerprint and AH-stretching region are shown in Fig. 4.2a. One clearly notices changes due to urethane formation, i.e. especially strong peaks at 1544 cm^{-1} and 1730 cm^{-1}. In the AH-stretching region changes can be observed with respect to the OH-absorption of the educt around 3400-3550 cm^{-1} and the amine NH-stretching mode of the product in the range of 3250-3320 cm^{-1}. Figure 4.2b shows the enlarged AH-stretching range as well as the difference between spectra taken at preparation time and 180 minutes thereafter. The spectra are normalised to the OH-absorption maximum such as to emphasize the changes in the NH-stretching range in the difference spectra. From these data it is clear that this spectral range can be used to monitor the amount of consumed alcohol during the reaction from **Ia** to **Ib**.

The assignment of the experimental IR spectrum listed above is based on the results of the anharmonic vibrational calculations for the structures **Ia** and **Ib** in Fig. 4.1. For the educt the OH-stretching vibration is predicted to be at 3571 cm^{-1} (intensity: 126 km/mol). In the product this vibration disappears and the NH-stretching mode appears at 3466 cm^{-1} (24 km/mol). The isocyanate group contributes the very intense NCO stretching vibration at 2302 cm^{-1} (1179 km/mol) in **Ia**. In the product this mode is absent, but there appears an amide I type CO-stretching band at 1756 cm^{-1} (146 km/mol) and an NH-bending mode at 1521 cm^{-1} (265 km/mol).

In Table 4.1 the harmonic and anharmonic frequencies for reaction **I** are presented together with their intensities. For displacement vectors see Fig. 4.3. In Fig. 4.4 the harmonic and anharmonic spectra are shown for initial state (upper) and product state (lower panel) for reaction **I**. The anharmonic spectra are red-shifted and improve an agreement with the experiment. In Fig. 4.5 the anharmonic spectrum for combination bands and overtones is shown for initial state (upper) and product state (lower panel). Combination bands are present at range around 3000 cm^{-1} but they don't disturb the OH stretch. A more detailed account on frequencies is given in Appendix B. The overtones and combination bands are presented in Appendix C.

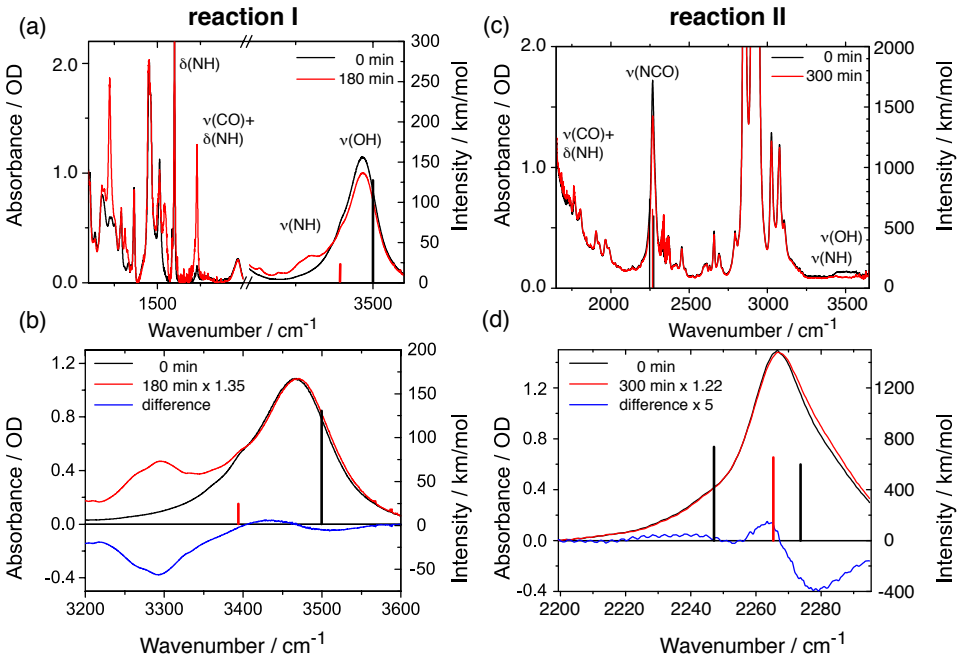

Figure 4.2: (a) Experimental IR spectra obtained by the group of Prof. K. Heyne, of PIC and cyclohexanol in tetrahydrofuran at preparation time (black line) and after 180 minutes (red line). (b) IR spectra in the spectral window around 3400 cm^{-1} for 0 min and 180 min, normalized to the OH absorption band at 3460 cm^{-1}, as well as their difference. (c) Experimental IR spectra of TDI and chloralhydrate solved in nitrobenzene at preparation (black line) and after 300 minutes (red line). (d) IR spectra in the spectral window around 2280 cm^{-1} for 0 min and 300 min (normalized to the NCO peak at 2263 cm^{-1}), as well as their difference. The calculated frequencies are shown as stick spectra in panels (b) and (d) (B3LYP/6-31++G(d,p) in gas phase, scaled by an empirical factor of 0.98 to improve the agreement with experimental data). The figure has been adopted from Ref. [84].

Reaction **I** Cyclohexanol					
No.	Mode	E(harm) cm^{-1}	I(harm) km/mol	E(anharm)	I(anharm)
1.	**OH**	3816	15	3641	11
Reaction **I** Phenylisocyanate					
2.	**NCO**	2362	1689	2320	1274
Reaction **I** Initial state					
3.	**OH**	3762	171	3571	126
4.	**NCO**	2339	1425	2302	1179
Reaction **I** Product state					
5.	**NH-stretching**	3630	32	3466	24
6.	**CO**	1784	267	1756	146
7.	**NH-bending**	1567	629	1521	265

Table 4.1: Vibration modes together with harmonic and anharmonic frequencies and their intensities for reaction **I**.

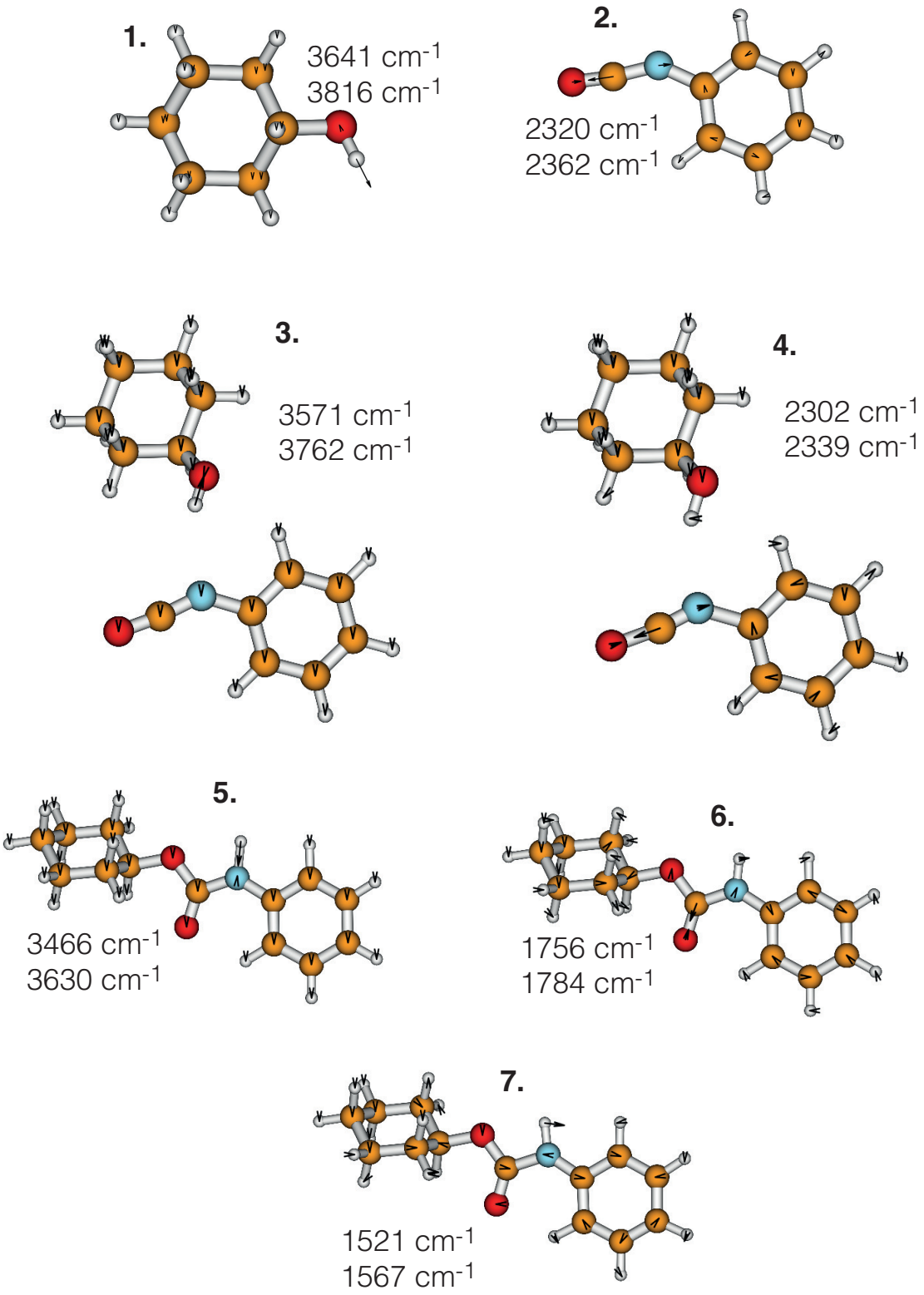

Figure 4.3: Anharmonic and harmonic frequencies for reaction **I** with normal mode displacement vectors. Numbers as in Table 4.1.

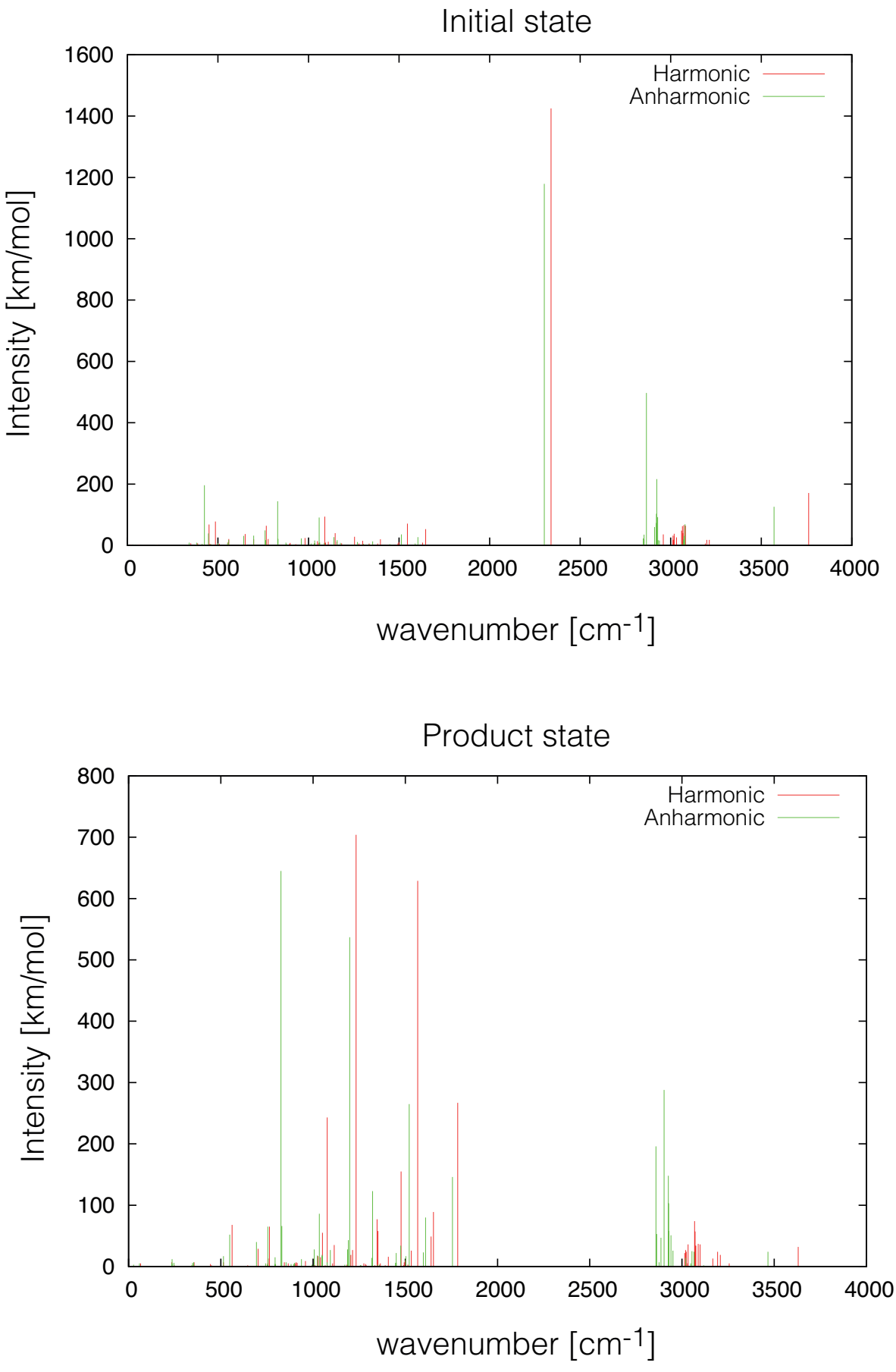

Figure 4.4: Harmonic and anharmonic absorption spectrum for reaction **I**.

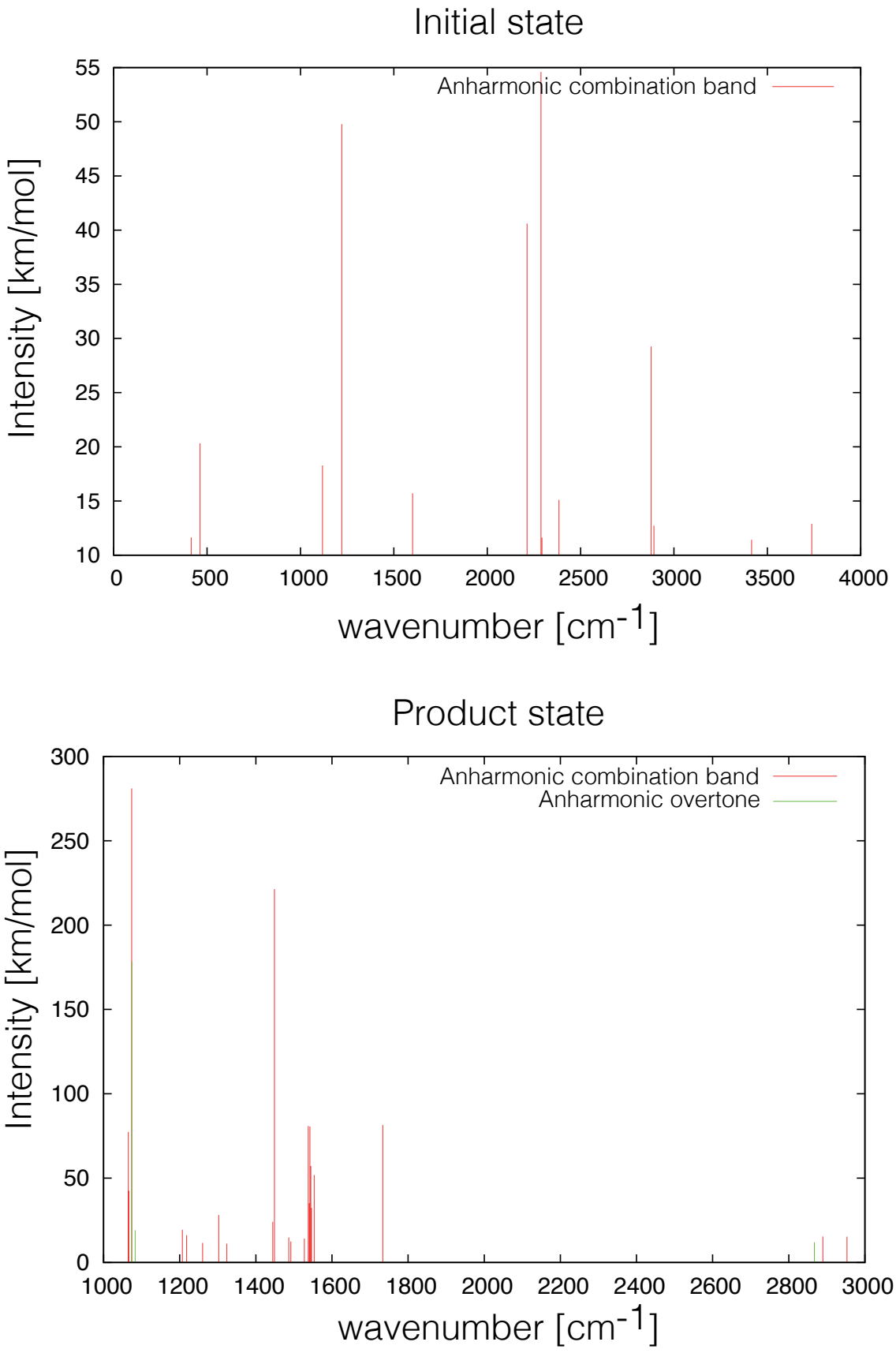

Figure 4.5: Anharmonic spectrum for combination bands and overtones for reaction **I**.

Reaction II

The discussion of the IR spectra for reaction **II** is complicated due to the fact that, in contrast to **I**, for the free reactants there are two hydroxyl and two isocyanate groups resulting in symmetric and antisymmetric collective vibrations. Let us focus on the results of the anharmonic frequency calculations for the educt (**IIa**) and the product (**IIb**). The free OH-stretching vibrations of the alcohol are found at 3614 cm^{-1} and 3577 cm^{-1}. Upon H-bonding in the educt complex the respective value reduces to 3488 cm^{-1}. The intensity of this transition is 181 km/mol and exceeds that of the remaining free OH-vibration at 3596 cm^{-1} (25 km/mol). In the reaction product, **IIb**, we calculate the remaining OH-vibration at 3560 cm^{-1} (106 km/mol) as well as the newly formed NH-vibration at 3465 cm^{-1} (30 km/mol). The symmetric and antisymmetric NCO-stretching vibrations of the two isocyanate groups in the isolated TDI are at 2308 cm^{-1} and 2323 cm^{-1}, respectively. In the educt complex, **IIa**, the symmetry is broken and the frequencies are 2284 cm^{-1} (737 km/mol) and 2311 cm^{-1} (599 km/mol) for the NCO-vibration at the reaction site and at the free isocyanate group, respectively. In the product complex, **IIb**, the H-bonded and red-shifted NCO-vibration disappears and the other one changes to 2302 cm^{-1}(654 km/mol). This results in a predicted intensity blue-shift of the total isocyanate stretching vibrational band.

The calculated spectra can be correlated to the changes in the experimental ones, observed between preparation and 300 minutes after preparation. Inspecting Fig. 4.2c one notices considerable intensity changes around 3500 cm^{-1} and 2263 cm^{-1} as well as smaller changes around 1763 cm^{-1} and 3395 cm^{-1}. In principle there are also some small changes around 3000 cm^{-1}, a range which is shaped by CH-stretching vibrations. The latter will not be considered in the following discussion. Spectral changes are due to alcoholysis of TDI and we assign them to the reaction of **IIb** formation and **IIa** consumption as follows. The OH-stretching vibrations of the chloralhydrate show one broad absorption peak at 3500 cm^{-1} (Fig. 4.2c). The NCO-vibrations of TDI absorb mainly at 2263 cm^{-1}, and 2240 cm^{-1} (Fig. 4.2d). Both the OH-stretching band intensities of the chloralhydrate and the NCO-stretching band intensity of TDI decreases with time, indicating consumption of TDI and chloralhydrate. At the same time the weaker NH-stretching vibrational band at 3395 cm^{-1}, and the CO-stretching/NH-bending vibrational band at 1763 cm^{-1} increases with time (Fig. 4.2c). Both bands clearly demonstrate the increase of an urethane reaction product. Thus the product formation of **IIb** results in a loss of one NCO-vibration, a small blue shift of the NCO absorption band, as depicted in Fig. 4.2d, and a total loss of the NCO vibrational band intensity.

In Table 4.2 the harmonic and anharmonic frequencies for reaction **II** are presented

together with their intensities. For displacement vectors see Figs. 4.6 and 4.7. In Fig. 4.8 the whole spectrum for reaction **II** is shown for harmonic and anharmonic frequencies for initial state (upper) and product state (lower panel). The anharmonic spectra are red-shifted and improve an agreement with the experiment. In Fig. 4.9 the anharmonic spectrum for combination bands and overtones is shown for initial (upper) and product state (lowe panel). There are combination bands at the range of around 2300 cm^{-1} but the intensities are much smaller than for the isocyanate vibrations. A more detailed account on frequencies is given in Appendix B. The overtones and combination bands are presented in Appendix C.

No.	Mode	E(harm) cm^{-1}	I(harm) km/mol	E(anharm)	I(anharm)
Reaction **II** Chloralhydrate					
8.	**OH**	3802	50	3614	43
9.	**OH**	3776	48	3577	43
Reaction **II** 2,4-Toluene Diisocyanate					
10.	**NCO**	2370	860	2323	558
11.	**NCO**	2354	2804	2308	1905
Reaction **II** Initial state					
12.	**OH**	3765	32	3596	25
13.	**OH**	3694	468	3488	181
14.	**NCO**	2363	1240	2311	599
15.	**NCO**	2331	2002	2284	737
Reaction **II** Product state					
16.	**OH**	3757	124	3560	106
17.	**NH**	3624	37	3465	30
18.	**NCO**	2364	1735	2302	654
19.	**CO/NH**	1776	341	1749	9

Table 4.2: Vibration modes together with harmonic and anharmonic frequencies and their intensities for reaction **II**.

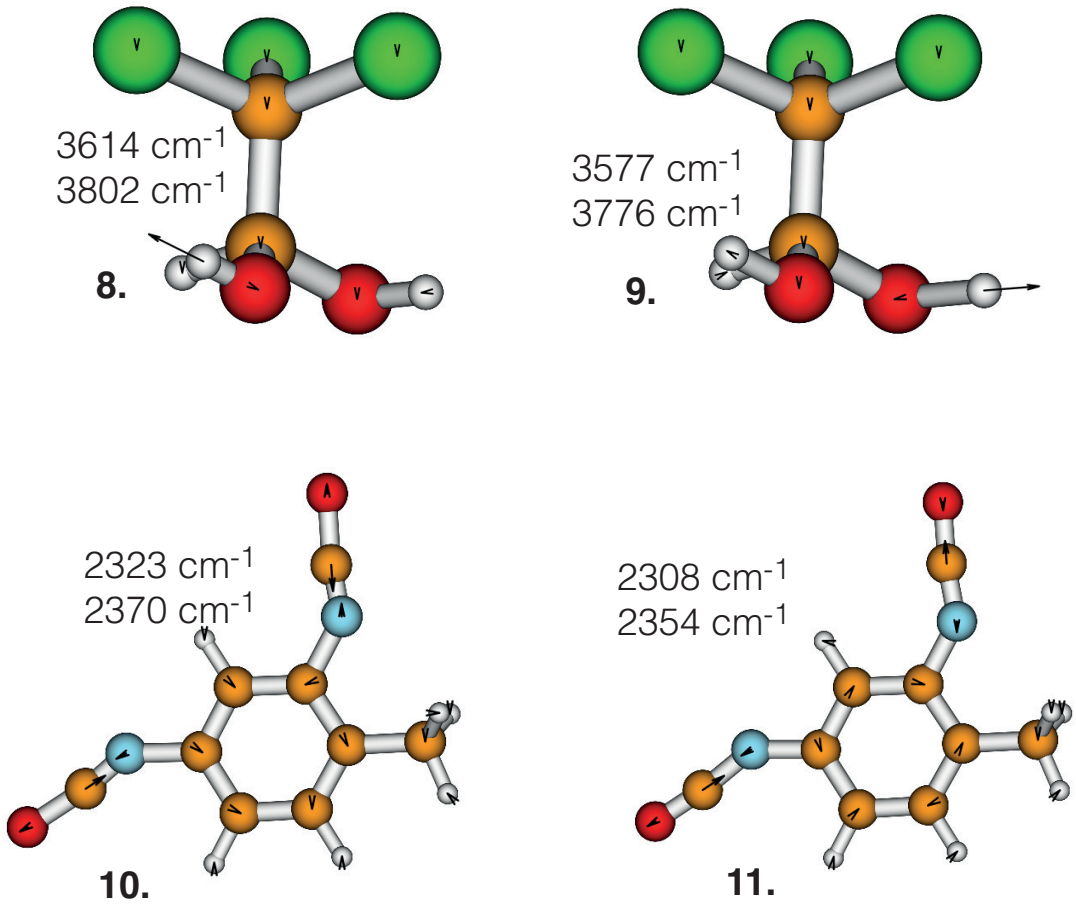

Figure 4.6: Anharmonic and harmonic frequencies for reaction **II** with normal mode displacement vectors. Numbers as in Table 4.2.

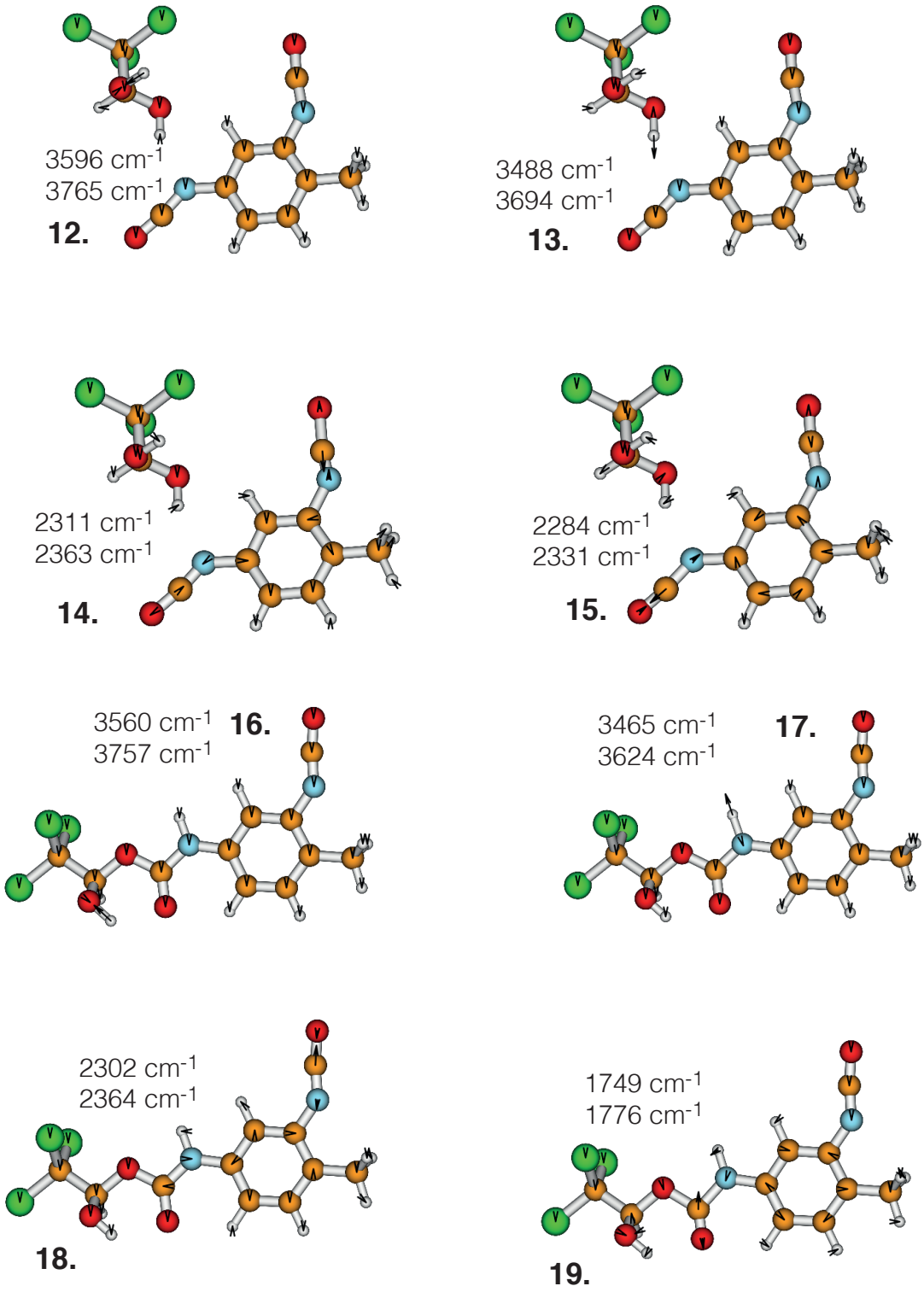

Figure 4.7: Anharmonic and harmonic frequencies for reaction **II** with normal mode displacement vectors. Numbers as in Table 4.2.

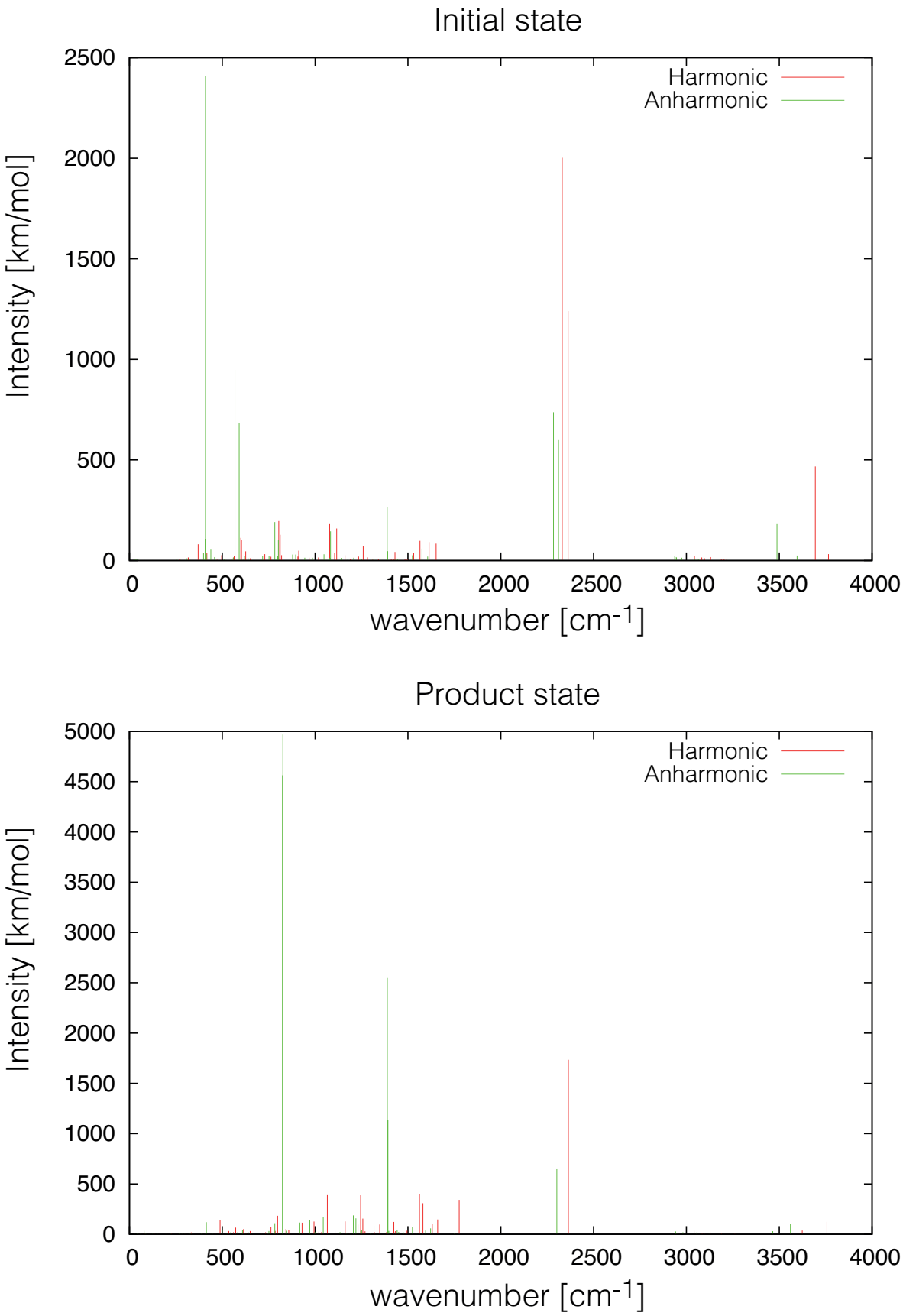

Figure 4.8: Harmonic and anharmonic absorption spectrum for reaction **II**.

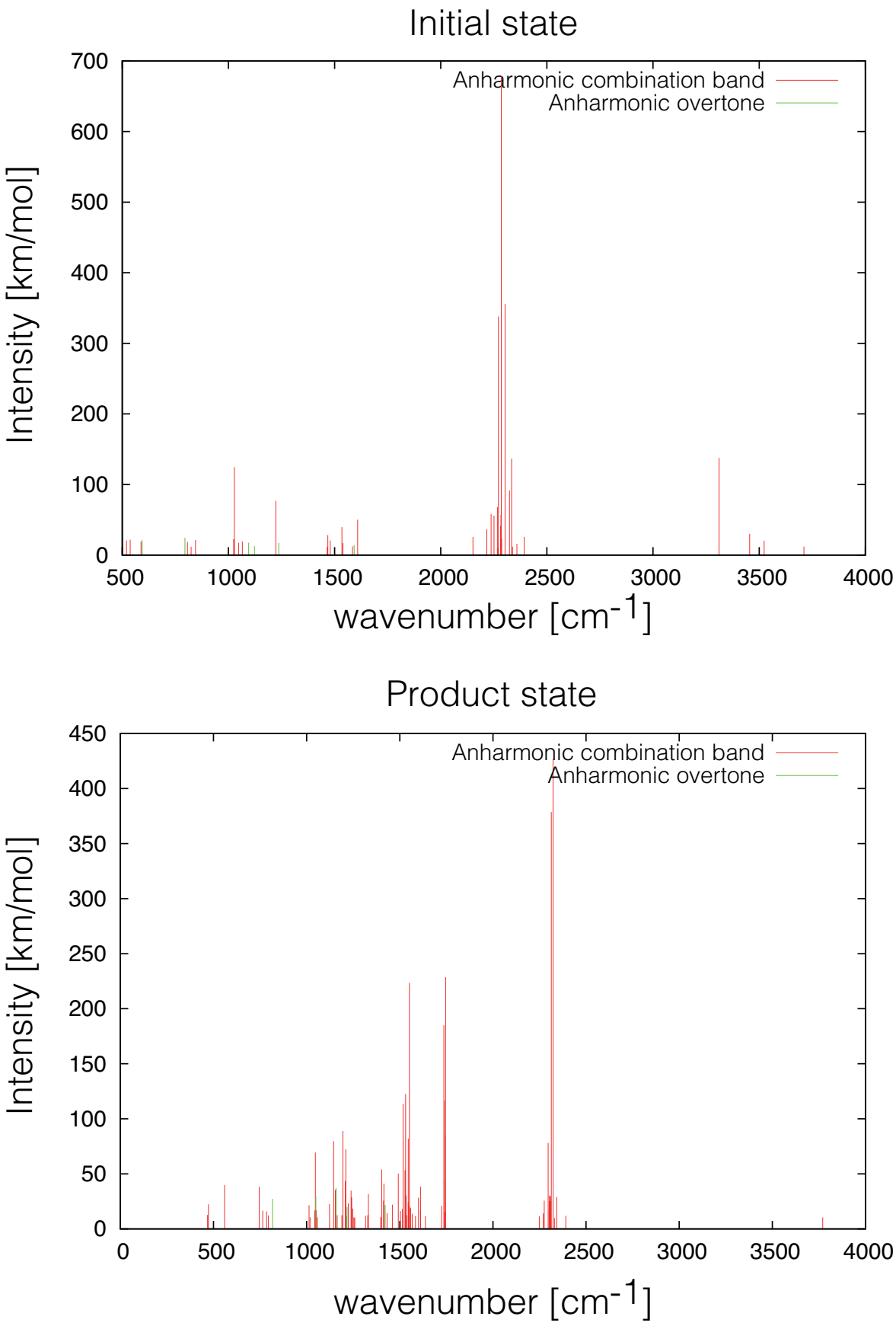

Figure 4.9: Anharmonic spectrum for combination bands and overtones for reaction **II**.

4.2.3 Arrhenius Activation Energies

The experimental results for Arrhenius activation energy obtained by the group of Prof. K. Heyne are presented in Fig. 4.10. For reaction **I** in panel (a) three time traces for change of the inverse absorbance of the OH-stretching band are depicted at different temperatures. The reaction can be described as a second-order kinetics. The slope corresponds with the rate constant of the reaction. Panel (b) presents the evaluation of the rate constant as a function of temperature. From this curve one can deduce the maximal reaction rate of 0.5 ± 0.2 L/mol s ($5.9 \pm 0.4 \times 10^{-6}$ L/mol s at room temperature) and the Arrhenius activation energy 6.7 ± 0.2 kcal/mol.

For reaction **II** in panel (c) are presented three time traces for change of the inverse absorbance of the NCO-band at different temperatures. Again the reaction can be described as second order kinetics. In panel (d) the result of an evaluation of the rate constant as a function of temperature is presented. From this curve one can deduce the maximal reaction rate of 1.1 $\pm 0.4 \times 10^{-3}$ L/mol s ($8.9 \pm 0.4 \times 10^{-6}$ L/mol s at room temperature) and the Arrhenius activation energy 2.8 ± 0.3 kcal/mol.

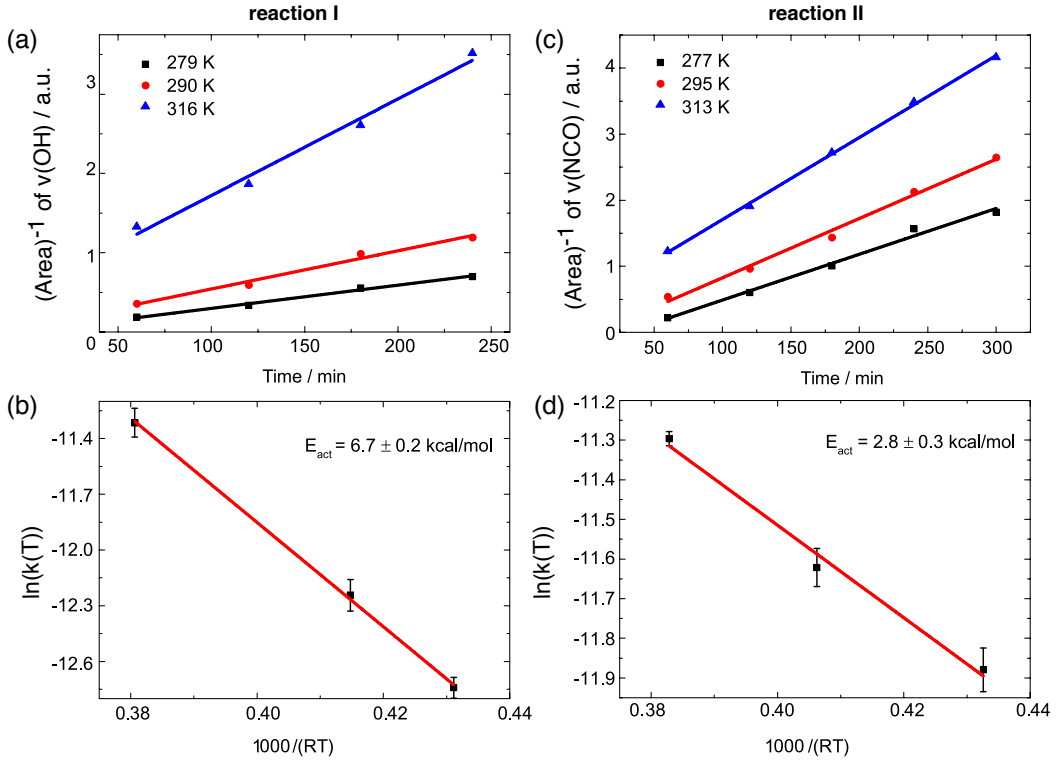

Figure 4.10: Change of the reciprocal vibrational band intensities with time and temperature for reactions **I** (a) and **II** (c). The linear slopes correspond to the second-order reaction rate constants. Panels (b) and (d) show the respective Arrhenius plots of the reaction rate constants at different temperatures (error bars have been determined from the error in the slopes in panels (a) and (c)). Experimental results obtained by the group of Prof. K. Heyne and jointly published in [84], figure adopted from that reference.

4.3 IRC and reaction barrier

In the previous section the reactions were monitored by IR spectroscopy and experimental values for Arrhenius activation energies have been shown. Now let us focus on the reaction barrier and look how the reaction proceeds along the reaction coordinate.

The present model study will focus on the alcoholysis reaction of isocyanates to form urethane. Specifically, the reaction of TDI (**III**) with chloralhydrate ($C_2H_3Cl_3O_2$ (**IV**)) will be considered, see Fig. 4.11.

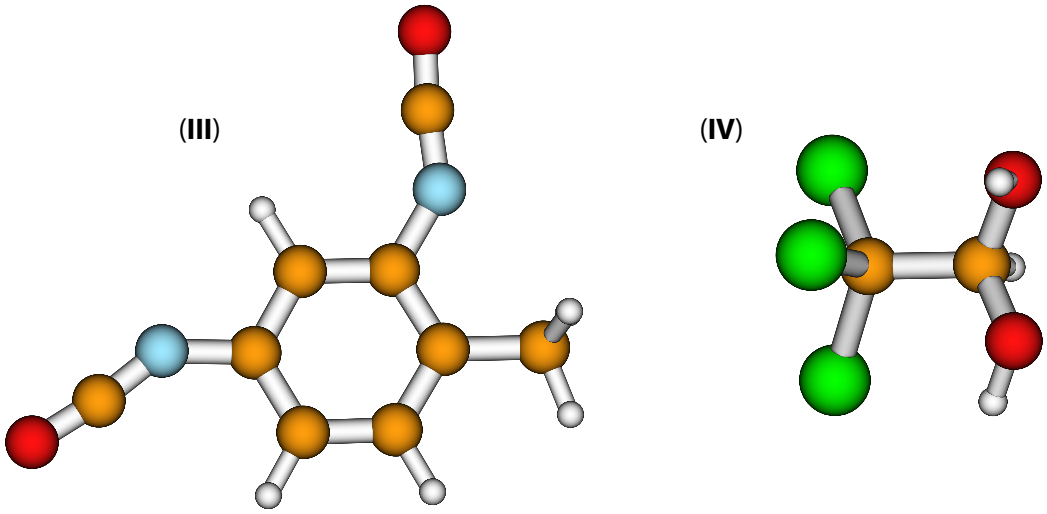

Figure 4.11: Educt molecules considered in this study: **III** - TDI and **IV** - chloralhydrate. The shown structures have been optimized at the DFT/B3LYP/6-31++G(d,p) level of theory in nitrobenzene described by the PCM approach.

Reference calculations have been performed using DFT/B3LYP with the 6-31++G(d, p) basis set as implemented in Gaussian 09 [55]. Solvent effects (nitrobenzene, $\varepsilon = 34.809$) are taken into account using the PCM approach [96]. Thermochemistry analysis has been performed assuming the harmonic approximation to be valid for the vibrational degrees of freedom. The IRC energy profile was calculated using the Hessian-based Predictor-Corrector integrator with a step-size of 0.15 a_B [97]. In the gas phase case a geometry optimization for a 6-311+G(d,p) basis set was performed as well. At this level also the MP2 correction to the electronic energies has been determined. Further, the magnitude of the basis set superposition error (BSSE) was estimated using the counterpoise correction [98].

Optimized gas phase structures (DFT/B3LYP(6-31++G(d,p)) at stationary points are shown in Fig. 4.12. Starting from the educts in Fig. 4.11 first, an intermediate or encounter complex is formed (**IIa**) while proceeding towards the transition state (**IIc**).

For completeness Fig. 4.12 contains the optimized structure (**IId**) for addition of a second TDI as well.

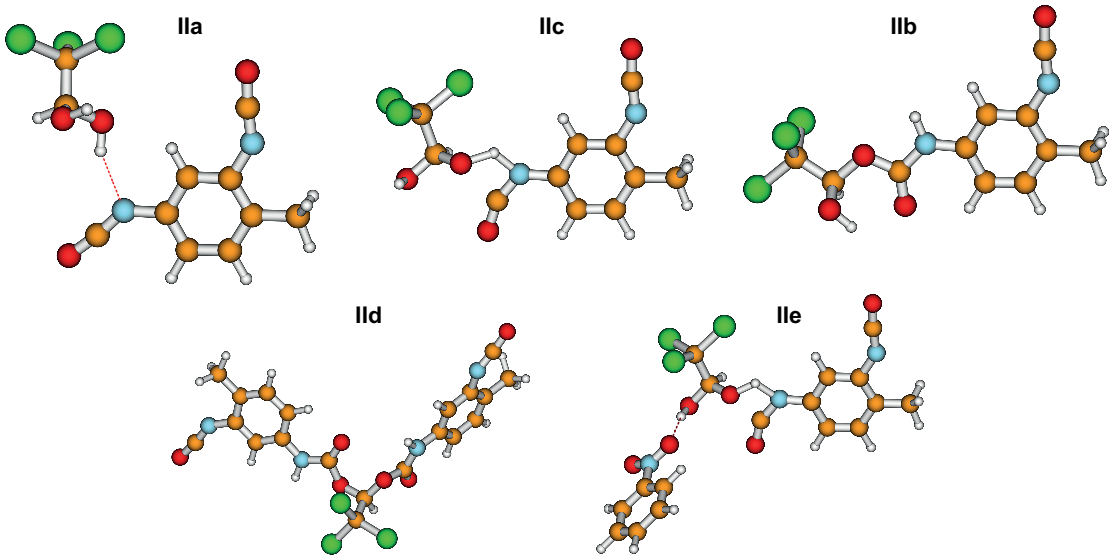

Figure 4.12: Optimized geometries (DFT/B3LYP/6-31++G(d,p)) for intermediate (**IIa**), transition state (**IIc**), and product (**IIb**) complex of the reaction model. Structure (**IId**) is the product state for addition of a second TDI molecule, i.e. polyurethane formation. (**IIe**) gives the transition state complex for the case of taking into account one explicit solvent nitrobenzene molecule.

The electronic energy along the gas phase IRC is shown in Fig. 4.13. The functional B97D has also been used to incorporate the dispersion correction. The nonlinear O-H$\cdots$N Hydrogen bond, mentioned in Sec. 4.2.1, at transition state contracts to 2.21 Å. The C-O bond distance for transition state contracts to 1.94 Å. The formation of the C-O bond takes place only after the H-transfer is completed. Atomic motions along the IRC path up to $\sim$-1.1 a_B essentially involve a compression of the O-H-N Hydrogen-bond length down to 2.26 Å(red line, ON distance). At this distance the electronic barrier with respect to the separated fragments has been reduced from about 36 kcal/mol to about 12 kcal/mol. From the lower panel it can be seen that the distance between N-H decreases, while between O-H increases at the same time and the whole process occurs at the narrow window such that the reactants come close together and suddenly H jumps to the other side.

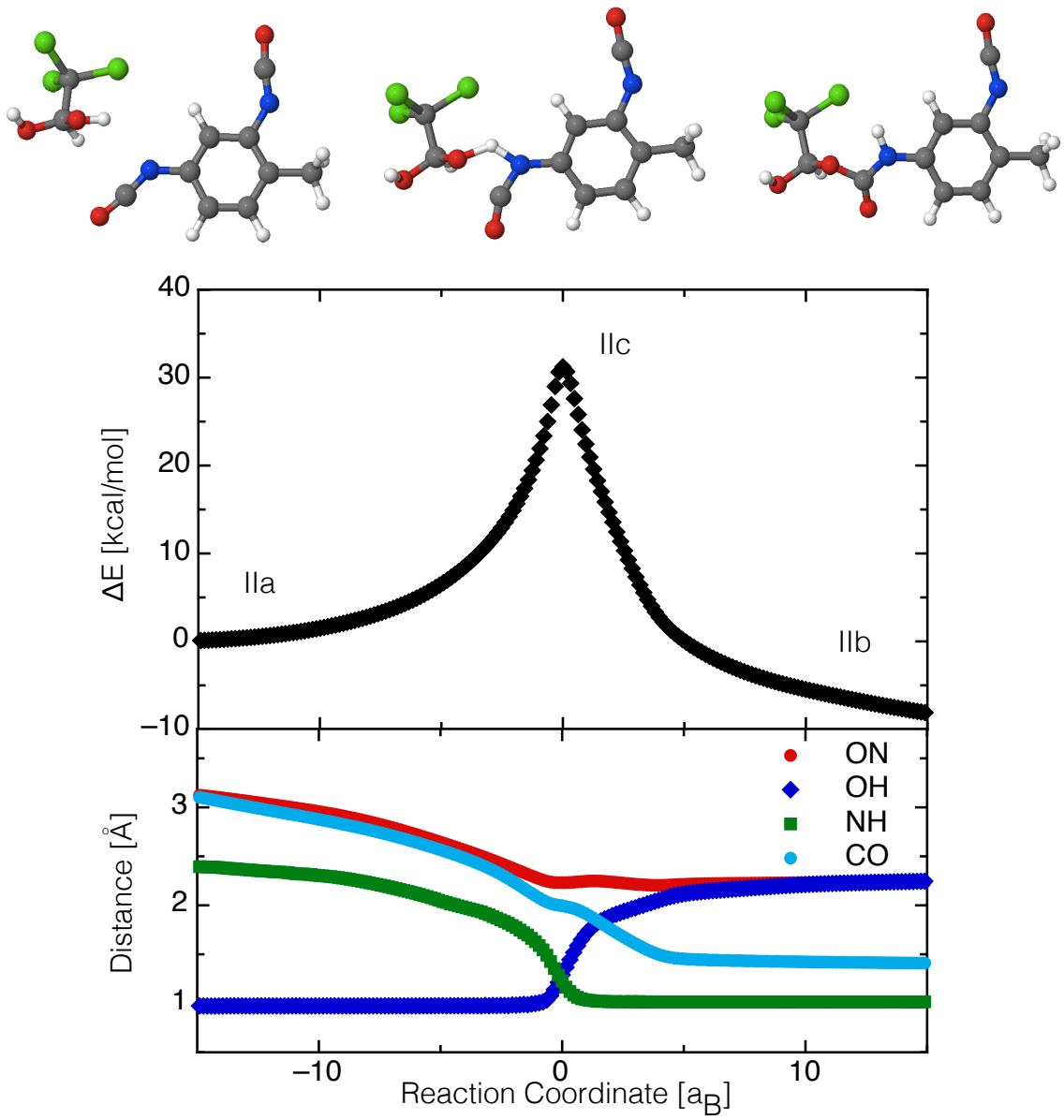

Figure 4.13: IRC path corresponding to the reaction shown on top. Distances between atoms are shown in the lower panel. The calculations have been performed with B97D functional.

Table 4.3: Energetics of the alcoholysis reaction model relative to separate reactants (in kcal/mol). Values are given in gas phase and for the 6-31++G(d,p) basis set. ΔE_{el} is the electronic energy difference and ΔH is the difference of the enthalpy. ΔG values in parentheses denote PCM nitrobenzene (ΔG(PCM)) and B3LYP/6-311++G(d,p) (ΔG(6-311++G(d,p))) results. ΔE_{MP2} gives the MP2 correction to the electronic energy calculated with the 6-311++G(d,p) basis set. The Arrhenius activation energy has been calculated as $E_{\mathrm{act}} = \Delta H + RT$ ($T = 298$K).

	B3LYP				B97D			ΔE_{MP2}
	ΔE_{el}	ΔH	ΔG	E_{act}	ΔH	ΔG	E_{act}	
IIa	-2.9	-1.5	6.7 (7.0, 6.9)	-	-5.0	4.5	-	-5.0
IIc	33.5	31.6	43.0 (43.8, 43.9)	32.2	26.2	37.6	26.8	-4.4
IIb	-18.2	-15.7	-2.5 (-1.2,0.2)	-	-13.1	-0.2	-	-5.5

The energetics of the reaction model is summarized in Table 4.3. Let us focus on the B3LYP/6-31++G(d,p) gas phase results first. The free energy of activation, ΔG, is 43.0 kcal/mol (or 36.3 kcal/mol with respect to **IIa**), i.e. it is close to the value reported for a similar reaction by Çoban and Konuklar [85]. In accord with Ref. [86] the reaction is exothermic. In contrast to Ref. [85] we find no appreciable effect of the solvent in the present case, i.e. ΔG stays almost the same. This can be traced to the fact that a certain stabilization of the transition state geometry is out-weighted by the longer H-bond (2.31 Å). Notice that in Ref. [85] no re-optimization in solution had been performed. Table 4.3 also contains results for a 6-311++G(d,p) basis set, ΔG(6-311++G(d,p)), which give almost the same free energy of activation and differ slightly in the stability of the product only. Given the modest size of the basis set we have also calculated the counter poise correction. The BSSE correction at the B3LYP/6-31++G(d,p) level amounts to 1.58 kcal/mol and appears to be negligible.

Overall, an Arrhenius activation energy of $E_{\mathrm{act}} = 32.2$ kcal/mol is obtained at the B3LYP/6-31++G(d,p) gas phase level of theory. Upon including the PCM solvent this value changes only slightly to 32.5 kcal/mol. Compared with experimental values for similar systems [87–91] and those reported above this value appears to be too large by a factor of about ten. To check for possible failures of standard DFT we have also performed geometry optimization including an empirical correction for dispersion interaction with the B97D functional. As can be seen from Table 4.3 this reduced the free energy of activation to 37.6 kcal/mol and the Arrhenius activation energy to $E_{\mathrm{act}} = 26.8$ kcal/mol. The structural changes at the transition state are modest only. As a further potential correction we have calculated the MP2 correlation energy at the DFT/6-311++G(d,p) optimized geometry. Compared to DFT this reduces the electronic barrier by -4.4 kcal/mol, see Table 4.3.

4.4 Discussion

Given the simplicity of our theoretical model the calculated and measured IR spectra are in reasonable agreement. One should note that, besides of the limitations inherent to the quantum chemical methodology, our model cannot capture the solvent effect leading to line broadening. Nevertheless, characteristic changes are observed in the range of the OH- and NCO-stretching vibrations, both in experiment and theory, providing evidence that indeed the two alcoholysis reactions can be monitored by theses marker bands in the IR spectrum. This complements the previously used methods discussed in Sec. 4.1 [87–91].

From the experimental studies on various alcoholysis reactions one can conclude that the Arrhenius energy of activation is in the range between 3 and 12 kcal/mol, with the present values being 6.7±0.2 kcal/mol and 2.8±0.3 kcal/mol for reaction **I** and **II**, respectively. This is in stark contrast to theoretical values reported so far, which are in general in the range around 30 kcal/mol [85, 86, 92–94]. A notable exception being the work of Raspoet et al. who promoted the catalyzing effect of additional alcohol molecules [92]. In the present case such catalyzing effect can be excluded for several reasons: First, as seen from Fig. 4.10 the reaction is rather well-described by second-order kinetics. Second, due to steric reasons it appears to be difficult to form larger complexes for the present alcohols. Third, the solvent nitrobenzene, for instance, cannot play the role of promoting proton transfer. This is illustrated in Fig. 4.12 where we show the optimized transition state geometry in the presence of a single nitrobenzene molecule (**IIe**). At the B3LYP/6-31++G(d,p) level one obtains a free energy of activation of $\Delta G = 43$ kcal/mol. Indeed preliminary quantum chemical calculations for reactions **I** and **II** in a PCM solvent model in Sec. 4.3 indicate that the Arrhenius activation energy is on the order of 30 kcal/mol, i.e. similar to literature values for such reactions [85, 86, 92–94].

A possible solution for the discrepancy between experiment and theory might come from the IRC in Fig. 4.13. As noted above, most part of the reaction coordinate movement from **IIa** to **IIc** corresponds to a compression of the O-H-N H-bond due to the translational approach of the chloralhydrate and TDI fragments. Substantial structural changes and in particular the actual H-transfer occurs only after about -1.1 a_B. At this point the electronic barrier has already been reduced by a factor of three. In fact one might argue that in the real solvated system the averaged effect of the interaction with the surrounding solvent molecules might cause such a H-bond compression, thus effectively reducing the reaction barrier (cage effect). This hypothesis is further supported by experiments in the group of Prof. Heyne on TDI and chloralhydrate in different solvents, which demonstrated that the reaction rate is significantly influenced by the

specific interactions with the solvent molecules. For instance, upon changing the solvent from nitrobenzene to DMSO we found that the speed of reaction **II** increases more than tenfold at room temperature. This could be taken as evidence that specific interactions between the educt complex and its solvent cage, might influence the reactions. Since the latter involves a proton transfer step, a compression of the Hydrogen-bond due to interactions with the solvent might reduce the barrier considerably [99].

4.5 Summary

In summary, we have shown that the progress of the acoholysis reaction of TDI with chloraldhydrate can be monitored by measuring the IR marker bands in the isocyanate NCO and alcohol OH stretching region. For the reaction of PIC with cyclohexanol the marker band is the OH-absorption, since the absorption of the isocyanate band is too strong. Experiments conducted at different temperatures gave a second-order kinetics, reaction rates in the range of 0.5 ± 0.2 L/mol s and $1.1 \pm 0.4 \times 10^{-3}$ L/mol s, and the Arrhenius activation energy 6.7 ± 0.2 kcal/mol, and 2.8 ± 0.3 kcal/mol for system **I** and **II**, respectively [84]. Quantum chemical calculations of the reaction path propose a mechanism, which is typical for H-transfer reactions. The educts approach each other thus reducing the H-bond length up to a point where the H atom transfers from the alcohol to the isocyanate group. Only after H-transfer the C=O bond is formed. An open question concerns the role of the solvent environment. Here, we propose that it leads, via a cage effect, to a compression of the H-bond in the precursor complex. This could explain the rather large difference between calculated and measured Arrhenius activation energies. Further evidence derives from the low reaction rate of system **II**. This can be explained by the weak hydrogen bond strength between TDI and chloral-hydrate, which results in a low probability for the formation of the precursor complex **IIa**. Once this precursor complex is formed it will be rather flexible, which reduces the probability for optimal cage configurations. Further work is needed to substantiate this hypothesis.

Chapter 5

Summary and Outlook

In summary, various aspects of reactive and non-reactive molecular dynamics in the electronic ground state have been considered.

First, a four dimensional model of the metal-dicarbonyl dynamics of *CpCo(CO)$_2$* has been obtained by DFT calculations at B3LYP/LanL2DZ level of theory. It contains two metal-carbonyl bond dissociation coordinates and two carbonyl vibrations coordinates. The anharmonic coupling between these coordinates was identified by looking at the shape of the PES and it was small for moderate energies. The time-dependent Schrödinger equation has been solved numerically by using MCTDH method. From propagation of the wave packet the anharmonic IR absorption spectra has been obtained.

By using linearly polarized light symmetric and antisymmetric CO vibrations were induced in order to investigate the possibility of bond breaking. In both cases the reaction yields were to small to observe the dissociation. One of the reason is that the anharmonic coupling between Co-CO and C-O coordinates was insufficient. Another one is that the energy is deposited over many bonds within a molecule.

It has been shown that two perpendicularly polarized laser pulses could be used to localize the collective carbonyl vibrations into a single CO bond and accumulate the energy. With this two pulses a superposition of eigenstates has been created. The alternating localization happens with the switching time determined by the energy gap between symmetric and antisymmetric fundamental transition frequencies. This process is, however, limited by the anharmonicity of the PES, what leads to wave packet dispersion for higher excitation energies.

Finally, the wave packet has started from an artificial initial conditions to further explore the anharmonicity. To this end, the ground state wave packet was displaced on the PES and propagated freely without any external electric field. It has been shown that only the extreme compression of the Co-CO bond does give an appreciable reaction yield. For CpCo(CO)$_2$ model system, the non-statistical metal-carbonyl bond breaking

was impossible to achieve by IR excitation of the carbonyl stretching vibrations. The dynamics could also be influenced by the other modes that are not implemented in the 4D model, i.e. via IVR processes what needs to be further investigated.

In the second part of the thesis, the alcoholysis reaction of isocyanates was considered. Two reactions have been presented. Only the second one leads to the formation of the polyurethane, but the first reaction requires the same initial step. Quantum chemical calculations at DFT/B3LYP/6-31++G(d,p) level of theory have been done to optimize gas phase structures at stationary points. It has been shown for both cases that educts were Hydrogen-bonded encounter complexes.

IR absorption spectra have been obtained from anharmonic vibrational calculations. They were compared with the experimental results obtained by the group of Prof. K. Heyne. The essential changes are in the range of the NCO- and OH-stretching vibrations. This means that in fact the two alcoholysis reactions can be monitored by these marker bands in the IR spectrum.

From the experimental studies the Arrhenius activation energies have been determined. The values are in strong contrast with the theoretical results. To learn why, the IRC path has been calculated. From the result one could see, that the complete reaction happens at the small window, such that the reactants come close together and the Hydrogen jumps to the other side. At that point, the electronic barrier was reduced by a factor of three. So, in the solvated system, the effect of the surrounding solvent molecules might effectively reduce the reaction barrier (cage effect).

The next step for the metal-carbonyl system could be an optimal control study. Optimal control theory is used in order to find a suitable laser field that steers the wave packet from the ground state to the desired exit channel. Another possibility, would be to find a different system, where the coupling between the vibrational-dissociation DOFs would be stronger. For the isocyanate system further theoretical work should be done in order to investigate the effect of the solvent on the reaction barrier and prove the hypothesis of the cage effect.

Bibliography

[1] Constantin Brif, Raj Chakrabarti, and Herschel Rabitz. Control of quantum phenomena: past, present and future. *New J. Phys.*, 12:075008, 2010.

[2] Paul Brumer and Moshe Shapiro. Laser Control of Molecular Processes. *Annu. Rev. Phys. Chem.*, 43:257–282, 1992.

[3] Hitoshi Kawashima, Marc M. Wefers, and Keith A. Nelson. Femtosecond Pulse Shaping, Multiple-Pulse Spectroscopy, and Optical Control. *Annu. Rev. Phys. Chem.*, 46:627–656, 1995.

[4] Yi-Yian Yin, D.S. Elliott, R. Shehadeh, and E.R. Grant. Two-pathway coherent control of photoelectron angular distributions in molecular NO. *Chem. Phys. Lett.*, 241:591 – 596, 1995.

[5] B. Sheehy, B. Walker, and L. F. DiMauro. Phase Control in the Two-Color Photodissociation of HD^+. *Phys. Rev. Lett.*, 74:4799–4802, 1995.

[6] David J. Tannor and Stuart A. Rice. Control of selectivity of chemical reaction via control of wave packet evolution. *J. Chem. Phys.*, 83:5013–5018, 1985.

[7] Markus Schröder, José-Luis Carreón-Macedo, and Alex Brown. Implementation of an iterative algorithm for optimal control of molecular dynamics into MCTDH. *Phys. Chem. Chem. Phys.*, 10:850–856, 2008.

[8] P. Balling, D. J. Maas, and L. D. Noordam. Interference in climbing a quantum ladder system with frequency-chirped laser pulses. *Phys. Rev. A*, 50:4276–4285, 1994.

[9] T. Witte, J. S. Yeston, M. Motzkus, E. J. Heilweil, and K.-L. Kompa. Femtosecond infrared coherent excitation of liquid phase vibrational population distributions (v>5). *Chem. Phys. Lett.*, 392:156 – 161, 2004.

[10] Christopher J. Bardeen, Vladislav V. Yakovlev, Jeff A. Squier, and Kent R. Wilson. Quantum Control of Population Transfer in Green Fluorescent Protein by Using Chirped Femtosecond Pulses. *J. Am. Chem. Soc.*, 120:13023–13027, 1998.

[11] Carlos R. Baiz, Porscha L. McRobbie, Jessica M. Anna, Eitan Geva, and Kevin J. Kubarych. Two-Dimensional Infrared Spectroscopy of Metal Carbonyls. *Acc. Chem. Res.*, 42:1395–1404, 2009.

[12] Carlos R. Baiz, Porscha L. McRobbie, Nicholas K. Preketes, Kevin J. Kubarych, and Eitan Geva. Two-Dimensional Infrared Spectroscopy of Dimanganese Decacarbonyl and Its Photoproducts: An Ab Initio Study. *J. Phys. Chem. A*, 113:9617–9623, 2009.

[13] S. Rice and M. Zhao. *Optical Control of Molecular Dynamics*. Wiley, Hoboken, 2001.

[14] O. Kühn and L. Wöste, editors. *Analysis and Control of Ultrafast Photoinduced Reactions*. vol. 87 of Springer Series in Chemical Physics. Springer, Heidelberg, 2007.

[15] Moshe Shapiro and Paul Brumer. *Principles of the Quantum Control of Molecular Processes*. Wiley-VCH, Weinheim, 2011.

[16] S. Chelkowski, A. D. Bandrauk, and P. B. Corkum. Efficient molecular dissociation by a chirped ultrashort infrared laser pulse. *Phys. Rev. Lett.*, 65:2355, 1990.

[17] Steven Arrivo, Thomas Dougherty, W. Grubbs, and Edwin Heilweil. Ultrafast infrared spectroscopy of vibrational CO-stretch up-pumping and relaxation dynamics of $W(CO)_6$. *Chem. Phys. Lett.*, 235:247–254, 1995.

[18] D. J. Maas, D. I. Duncan, R. B. Vrijen, W. J. van der Zande, and L. D. Noordam. Vibrational ladder climbing in NO by (sub)picosecond frequency–chirped infrared laser pulses. *Chem. Phys. Lett.*, 290:75, 1998.

[19] T. Witte, T. Hornung, L. Windhorn, D. Proch, R. de Vivie-Riedle, M. Motzkus, and K. L. Kompa. Controlling molecular ground-state dissociation by optimizing vibrational ladder climbing. *J. Chem. Phys.*, 118:2021, 2003.

[20] Lars Windhorn, Jake S. Yeston, Thomas Witte, Werner Fuss, Marcus Motzkus, Detlev Proch, Karl-Ludwig Kompa, and C. Bradley Moore. Getting ahead of IVR: A demonstration of mid-infrared induced molecular dissociation on a sub-statistical time scale. *J. Chem. Phys.*, 119:641–645, 2003.

[21] D. B. Strasfeld, Sang-Hee Shim, and Martin T. Zanni. New advances in mid-IR pulse shaping and its application to 2D IR spectroscopy and ground-state coherent control. *Adv. Chem. Phys.*, 141:1–28, 2009.

[22] David B. Strasfeld, Sang-Hee Shim, and Martin T. Zanni. Controlling vibrational excitation with shaped mid-IR pulses. *Phys. Rev. Lett.*, 99:038102, 2007.

[23] David B. Strasfeld, Chris T. Middleton, and Martin T. Zanni. Mode selectivity with polarization shaping in the mid-IR. *New J. Phys.*, 11:105046, 2009.

[24] S. Ashihara, K. Enomoto, and J. Tayama. Controlling Quantum Interferences in IR Vibrational Excitations in Metal Carbonyls. *EPJ Web of Conferences*, 41:3, 2013.

[25] Cathie Ventalon, James M. Fraser, Marten H. Vos, Antigoni Alexandrou, Jean-Louis Martin, and Manuel Joffre. Coherent vibrational climbing in carboxyhemoglobin. *Proc. Natl. Acad. Sci. U.S.A.*, 101:13216–13220, 2004.

[26] O. Kühn. Multidimensional vibrational quantum dynamics of CO-heme compounds: ultrafast IVR mediated Fe-CO bond-breaking after CO excitation? *Chem. Phys. Lett.*, 402:48–53, 2005.

[27] M. H. Beck, A. Jäckle, G. A. Worth, and H. D. Meyer. The multiconfiguration time-dependent Hartree (MCTDH) method: a highly efficient algorithm for propagating wavepackets. *Phys. Rep.*, 324:1–105, 2000.

[28] O. Kühn. Laser Driven Dynamics and Quantum Control of Molecular Wave Packets. In H.-D. Meyer, F. Gatti, and G. A. Worth, editors, *Multidimensional Quantum Dynamics*, page 335. Wiley-VCH, Weinheim, 2009.

[29] C. Gollub, B. M. R. Korff, K. L. Kompa, and R. de Vivie-Riedle. Chirp-driven vibrational distribution in transition metal carbonyl complexes. *Phys. Chem. Chem. Phys.*, 9:369–376, 2007.

[30] Christoph Meier and Marie-Catherine Heitz. Laser control of vibrational excitation in carboxyhemoglobin: A quantum wave packet study. *J. Chem. Phys.*, 123:044504, 2005.

[31] Volker Engel, Christoph Meier, and David J. Tannor. Local Control Theory: Recent Applications to Energy and Particle Transfer Processes in Molecules. In *Adv. Chem. Phys.*, pages 29–101. John Wiley & Sons, Inc., 2009.

[32] Cyril Falvo, Arunangshu Debnath, and Christoph Meier. Vibrational ladder climbing in carboxy-hemoglobin: Effects of the protein environment. *J. Chem. Phys.*, 138:145101, 2013.

[33] Arunangshu Debnath, Cyril Falvo, and Christoph Meier. State-Selective Excitation of the CO Stretch in Carboxyhemoglobin by Mid-IR Laser Pulse Shaping: A Theoretical Investigation. *J. Phys. Chem. A*, 117:12884–12888, 2013.

[34] A. E. Orel, Y. Zhao, and O. Kühn. Laser driven ground state photodissociation of $HCo(CO)_4$: An ab initio quantum molecular dynamics approach. *J. Chem. Phys.*, 112:94, 2000.

[35] Y. Zhao and O. Kühn. Selective infrared laser pulse control of H and CO branching in the ground-state photodissociation of $HCo(CO)_4$ - A two-dimensional model simulation. *Chem. Phys. Lett.*, 302:7–14, 1999.

[36] O. Kühn, J. Manz, and Y. Zhao. Ultrafast IR Laser Control of Photodissociation: Single- versus Multi-pulse Schemes. *Phys. Chem. Chem. Phys.*, 1:3103, 1999.

[37] Y. Zhao and O. Kühn. Competitive Local Laser Control of the Photodissociation Reaction $HCo(CO)_4 \rightarrow HCo(CO)_3 + CO$ in the Electronic Ground State. *J. Phys. Chem. A*, 104:4882, 2000.

[38] Mahmoud Abdel-Latif and Oliver Kühn. Carbonyl vibrational wave packet circulation in $Mn_2(CO)_{10}$ driven by ultrashort polarized laser pulses. *J. Chem. Phys.*, 135:084314, 2011.

[39] Mangirdas Malinauskas, Maria Farsari, Algis Piskarskas, and Saulius Juodkazis. Ultrafast laser nanostructuring of photopolymers: A decade of advances. *Phys. Rep.*, 533:1–31, 2013.

[40] A. A. Caraculacu and S. Coseri. Isocyanates in polyaddition processes. Structure and reaction mechanisms. *Prog. Polym. Sci*, 26:799–851, 2001.

[41] K. Heyne, F. Kössl, V. Kozich, M. Lisaj, and O. Kühn. Femtosecond mid-IR laser tailored step-growth polymerization process. In M. Roeffaers and J. Hofkens, editors, *Book of Abstracts ICP Leuven*, page 81, 2013.

[42] P. Hamm, S. M. Ohline, and W. Zinth. Vibrational cooling after ultrafast photoisomerization of azobenzene measured by femtosecond infrared spectroscopy. *J. Chem. Phys.*, 106:519–529, 1997.

[43] Martin T. Zanni, S. Gnanakaran, Jens Stenger, and Robin M. Hochstrasser. Heterodyned Two-Dimensional Infrared Spectroscopy of Solvent-Dependent Conformations of Acetylproline-NH_2. *J. Phys. Chem. B*, 105:6520–6535, 2001.

[44] V. Kozich, W. Werncke, A. I. Vodchits, and J. Dreyer. Ultrafast excitation of out-of-plane vibrations and vibrational energy redistribution after internal conversion of 4-nitroaniline. *J. Chem. Phys.*, 118:1808–1814, 2003.

[45] Karsten Heyne, Erik T. J. Nibbering, Thomas Elsaesser, Milena Petković, and Oliver Kühn. Cascaded Energy Redistribution upon O-H Stretching Excitation in an Intramolecular Hydrogen Bond. *J. Phys. Chem. A*, 108:6083–6086, 2004.

[46] Volkhard May and Oliver Kühn. *Charge and Energy Transfer Dynamics in Molecular Systems, 3rd Revised and Enlarged Edition.* Wiley-VCH, Weinheim, 2011.

[47] P. Hohenberg and W. Kohn. Inhomogeneous Electron Gas. *Phys. Rev.*, 136:B864–B871, 1964.

[48] W. Koch and M. C. Holthausen. *A Chemist's Guide to Density Functional Theory.* Wiley, 2000.

[49] W. Kohn and L. J. Sham. Self - Consistent Equations Including Exchange And Correlation Effects. *Phys. Rev.*, 140:1133–1138, 1965.

[50] Robert G. Parr and Weitao Yang. *Density - Functional Theory of Atoms and Molecules.* Oxford University Press USA, 1989.

[51] A. D. Becke. Density - functional thermochemistry. III. The role of exact exchange. *J. Chem. Phys.*, 98:5648–5652, 1993.

[52] Andreas Dreuw, Barry D. Dunietz, and Martin Head-Gordon. Characterization of the Relevant Excited States in the Photodissociation of CO-Ligated Hemoglobin and Myoglobin. *J. Am. Chem. Soc.*, 124:12070–12071, 2002.

[53] A. D. Becke. Density - functional exchange-energy approximation with correct asymptotic behavior. *Phys. Rev. A*, 38:3098–3100, 1988.

[54] Chengteh Lee, Weitao Yang, and Robert G. Parr. Development of the Colle-Salvetti correlation-energy formula into a functional of the electron density. *Phys. Rev. B*, 37:785–789, 1988.

[55] M. J. Frisch, G. W. Trucks, H. B. Schlegel, G. E. Scuseria, M. A. Robb, J. R. Cheeseman, G. Scalmani, V. Barone, B. Mennucci, G. A. Petersson, H. Nakatsuji, M. Caricato, X. Li, H. P. Hratchian, A. F. Izmaylov, J. Bloino, G. Zheng, J. L. Sonnenberg, M. Hada, M. Ehara, K. Toyota, R. Fukuda, J. Hasegawa, M. Ishida, T. Nakajima, Y. Honda, O. Kitao, H. Nakai, T. Vreven, J. A. Montgomery, Jr., J. E. Peralta, F. Ogliaro, M. Bearpark, J. J. Heyd, E. Brothers, K. N. Kudin, V. N.

Staroverov, R. Kobayashi, J. Normand, K. Raghavachari, A. Rendell, J. C. Burant, S. S. Iyengar, J. Tomasi, M. Cossi, N. Rega, J. M. Millam, M. Klene, J. E. Knox, J. B. Cross, V. Bakken, C. Adamo, J. Jaramillo, R. Gomperts, R. E. Stratmann, O. Yazyev, A. J. Austin, R. Cammi, C. Pomelli, J. W. Ochterski, R. L. Martin, K. Morokuma, V. G. Zakrzewski, G. A. Voth, P. Salvador, J. J. Dannenberg, S. Dapprich, A. D. Daniels, . Farkas, J. B. Foresman, J. V. Ortiz, J. Cioslowski, and D. J. Fox. Gaussian 09 Revision D.01. Gaussian Inc. Wallingford CT 2009.

[56] Christopher J. Cramer. *Essentials of Computational Chemistry: Theories and Models*. John Wiley & Sons, Chichester, West Sussex, England, 2004.

[57] Stefan Grimme. Density functional theory with London dispersion corrections. *WIREs Comput. Mol. Sci.*, 1:211–228, 2011.

[58] C. Møller and M. S. Plesset. Note on an approximation treatment for many-electron systems. *Phys. Rev.*, 46:618–622, 1934.

[59] Ansgar Schäfer, Hans Horn, and Reinhart Ahlrichs. Fully optimized contracted gaussian basis sets for atoms Li to Kr. *J. Chem. Phys.*, 97:2571–2577, 1992.

[60] Ansgar Schäfer, Christian Huber, and Reinhart Ahlrichs. Fully optimized contracted gaussian basis sets of triple zeta valence quality for atoms Li to Kr. *J. Chem. Phys.*, 100:5829–5835, 1994.

[61] A. D. McLean and G. S. Chandler. Contracted Gaussian basis sets for molecular calculations. I. Second row atoms, Z = 11 - 18. *J. Chem. Phys.*, 72:5639–5648, 1980.

[62] Computational Chemistry List, ccl.net website. `http://www.ccl.net/cca/documents/basis-sets/basis.html`.

[63] P. Jeffrey Hay and Willard R. Wadt. Ab initio effective core potentials for molecular calculations. Potentials for the transition metal atoms Sc to Hg. *J. Chem. Phys.*, 82:270–283, 1985.

[64] Willard R. Wadt and P. Jeffrey Hay. Ab initio effective core potentials for molecular calculations. potentials for main group elements Na to Bi. *J. Chem. Phys.*, 82:284–298, 1985.

[65] P. Jeffrey Hay and Willard R. Wadt. Ab initio effective core potentials for molecular calculations. Potentials for K to Au including the outermost core orbitals. *J. Chem. Phys.*, 82:299–310, 1985.

[66] Mohamed Shibl. *Mechanisms of Double Proton Tautomerization & Quantum Control of Tautomerism in Enantiomers by Light*. PhD thesis, Freie Universitaet Berlin, 2006.

[67] H. D. Meyer, U. Manthe, and L. S. Cederbaum. The multi-configurational time-dependent Hartree approach. *Chem. Phys. Lett.*, 165:73–78, 1990.

[68] H. D. Meyer, F. Gatti, and G. A. Worth. *Multidimensional Quantum Dynamics: MCTDH Theory and Applications*. Wiley-VCH, Weinheim, 2009.

[69] Hans-Dieter Meyer. Studying molecular quantum dynamics with the multiconfiguration time-dependent Hartree method. *WIREs Comput. Mol. Sci.*, 2:351–374, 2012.

[70] David J. Tannor. *Introduction to Quantum Mechanics: A Time-Dependent Perspective*. University Science Books, USA, 2007.

[71] P. A. M. Dirac. Note on exchange phenomena in the Thomas atom. *Proc. Cambridge Philos. Soc.*, 26:376–385, 1930.

[72] A. Frenkel. *Wave Mechanics: Advanced General Theory*. The Clarendon Press, Oxford, 1934.

[73] M. H. Beck and H. D. Meyer. An efficient and robust integration scheme for the equations of motion of the multiconfiguration time-dependent Hartree (MCTDH) method. *Z. Phys. D Atom Mol. Cl.*, 42:113–129, 1997.

[74] H. Tal-Ezer and R. Kosloff. An accurate and efficient scheme for propagating the time dependent Schrödinger equation. *J. Chem. Phys.*, 81:3967–3971, 1984.

[75] Tae Jun Park and J. C. Light. Unitary quantum time evolution by iterative Lanczos reduction. *J. Chem. Phys.*, 85:5870–5876, 1986.

[76] G. A. Worth, M. H. Beck, A. Jäckle, and H. D. Meyer. *The MCTDH Package, Version 8.2, (2000), University of Heidelberg, Heidelberg, Germany. H.-D. Meyer, Version 8.3 (2002), Version 8.4 (2007), O. Vendrell and H.-D. Meyer, Version 8.5 (2011)*. See http://mctdh.uni-hd.de, 2007.

[77] R. Kosloff and H. Tal-Ezer. A direct relaxation method for calculating eigenfunctions and eigenvalues of the Schrödinger equation on a grid. *Chem. Phys. Lett.*, 127:223–230, 1986.

[78] S. Martin, L. Chen, R. Brédy, J. Bernard, G. Montagne, and X. Zhu. Excitation and dissociation of tungsten hexacarbonyl $W(CO)_6$: Statistical and nonstatistical dissociation processes. *J. Chem. Phys.*, 134:034304, 2011.

[79] Barry D. Dunietz, Andreas Dreuw, and Martin Head-Gordon. Initial steps of the photodissociation of the CO Ligated Heme Group. *J. Phys. Chem. B*, 107:5623–5629, 2003.

[80] B. Beagley, C. T. Parrott, V. Ulbrecht, and G. G. Young. A gas-phase electron diffraction study of the molecular structure of cyclopentadienyl cobalt dicarbonyl, $C_5H_5Co(CO)_2$. *J. Mol. Struct.*, 52:47–52, 1979.

[81] A. Jäckle and H.-D. Meyer. Product representation of potential energy surfaces. *J. Chem. Phys.*, 104:7974–7984, 1996.

[82] G. A. Worth, M. H. Beck, A. Jäckle, H.D. Meyer, F. Otto, M. Brill, and O. Vendrell. The Heidelberg MCTDH Package: A set of programs for multi-dimensional quantum dynamics. User's Guide. Heidelberg, Germany, 2014.

[83] F. A. Cotton, A. D. Liehr, and G. Wilkinson. Infrared Spectra and Structures of Cyclopentadienyl-Carbon Monoxide Compounds of V, Mn, Fe, Co, Mo, and W. *J. Inorg. Nucl. Chem.*, 1:175–186, 1955.

[84] F. Kössl, M. Lisaj, V. Kozich, K. Heyne, and O. Kühn. Monitoring the alcoholysis of isocyanates with infrared spectroscopy. *Chem. Phys. Lett.*, 621:41 – 45, 2015.

[85] M. Çoban and F. A. S. Konuklar. A computational study on the mechanism and the kinetics of urethane formation. *Comp. Theor. Chem.*, 963:168–175, 2011.

[86] P. Cysewski, P. Król, and A. Shyichuk. First principle simulations of ethylene glycol addition to diisocyanates. *Macromol. Theory Simul.*, 16:541–547, 2007.

[87] P. Król, B. Atamanczuk, and Jan Pielichowski. Kinetic study of the polycondensation of diisocyanates with polyols. *J. Appl. Polym. Sci.*, 46:2139–2146, 1992.

[88] Piotr Król and Joanna Wojturska. Kinetic study on the reaction of 2,4- and 2,6-tolylene diisocyanate with 1-butanol in the presence of styrene, as a model reaction for the process that yields interpenetrating polyurethane–polyester networks. *J. Appl. Polym. Sci.*, 88:327–336, 2003.

[89] S. Sivakamasundari and R. Ganesan. Kinetics and mechanism of the reaction between phenyl isocyanate and alcohols in benzene medium. *J. Org. Chem.*, 49:720–722, 1984.

[90] Y. Iwakura. The kinetics of the polyurethane-forming reaction between organic diisocyanates and glycols. I. The reaction of phenyl isocyanate with polymethylene glycol. *Makromol. Chem.*, 58:237–241, 1962.

[91] Shane Parnell, K. Min, and M. Cakmak. Kinetic studies of polyurethane polymerization with Raman spectroscopy. *Polymer*, 44:5137–5144, 2003.

[92] G. Raspoet, M. T. Nguyen, M. McGarraghy, and A. F. Hegarty. The alcoholysis reaction of isocyanates giving urethanes: Evidence for a multimolecular mechanism. *J. Org. Chem.*, 63:6878–6885, 1998.

[93] A. Y. Samuilov, L. A. Zenitova, Y. D. Samuilov, and A. I. Konovalov. Quantum-chemical study on the reaction of phenyl isocyanate with linear methanol associates. Addition at the C=N bond. *Russ. J. Org. Chem.*, 44:1316–1322, 2008.

[94] Xiaoxuan Wang, Wei Hu, Dayong Gui, Xuhui Chi, Mingliang Wang, Deyu Tian, Jianhong Liu, Xingang Ma, and Aimin Pang. DFT Study of the Proton Transfer in the Urethane Formation between 2,4-Diisocyanatotoluene and Methanol. *Bull. Chem. Soc. Jpn.*, 86:255–265, 2013.

[95] Julien Bloino and Vincenzo Barone. A second-order perturbation theory route to vibrational averages and transition properties of molecules: General formulation and application to infrared and vibrational circular dichroism spectroscopies. *J. Chem. Phys.*, 136:124108, 2012.

[96] Jacopo Tomasi, Benedetta Mennucci, and Roberto Cammi. Quantum Mechanical Continuum Solvation Models. *Chem. Rev.*, 105:2999–3094, 2005.

[97] Hrant P. Hratchian and H. Bernhard Schlegel. Accurate reaction paths using a Hessian based predictorcorrector integrator. *J. Chem. Phys.*, 120:9918–9924, 2004.

[98] S. F. Boys and F. Bernardi. The calculation of small molecular interactions by the differences of separate total energies. Some procedures with reduced errors. *Mol. Phys.*, 19:553–566, 1970.

[99] K. Giese, M. Petković, H. Naundorf, and O. Kühn. Multidimensional quantum dynamics and infrared spectroscopy of hydrogen bonds. *Phys. Rep.*, 430:211–276, 2006.

Appendices

Appendix A

Convergence for Localization Simulations

The convergence for the simulations presented in Figs. 3.17 and 3.18, is shown in Fig. A.1. It is less than $\sim$0.1% for all cases. In the left panel maximum of the smallest NOP are shown for phase zero degrees. For field amplitude $E_0 = 0.001$ $\mathrm{E_h/ea_B}$ 4 SPFs were taken, for $E_0 = 0.0015$ $\mathrm{E_h/ea_B}$ 8 SPFs and for $E_0 = 0.002$ $\mathrm{E_h/ea_B}$ 12 SPFs. The right panel for phase 180 degrees shows similar convergence for the same number of SPFs.

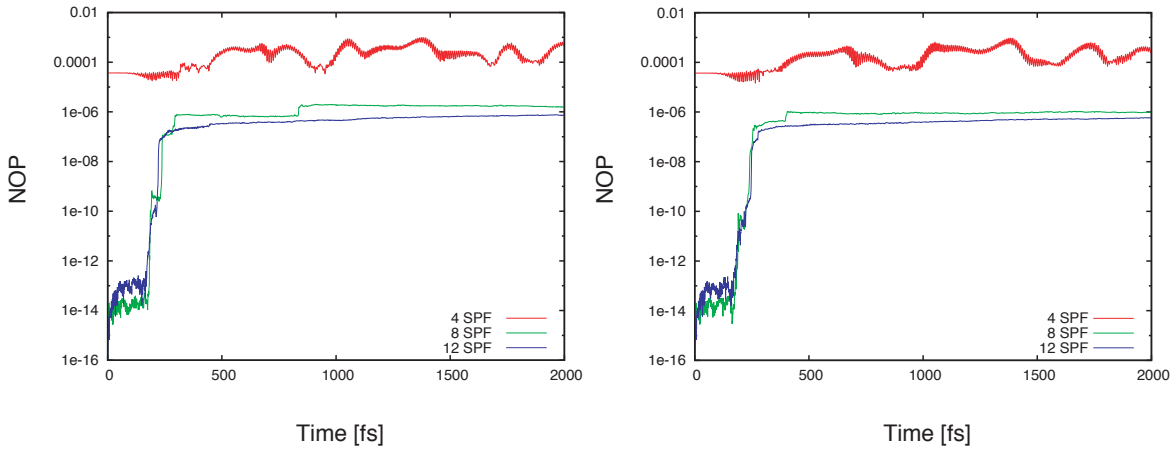

Figure A.1: Two plots show maximum of the smallest natural orbital population for simulations with phases zero (left) and phase 180 (right) degrees, see Figs. 3.17, 3.18.

Appendix B

Anharmonic Vibrational Frequencies and IR Intensities for Alcoholysis Reactions

B.1 Reaction I

Reaction **I** is composed of phenylisocyanate and cyclohexanol molecules. The harmonic and anharmonic frequencies calculations have been performed at DFT/B3LYP/6-31++G(d,p) level of theory. The computations have been done for four cases. The results for cyclohexanol alone are shown in Table B.1. The results for phenylisocyanate alone are presented in Table B.2. For the initial state the frequencies are shown in Table B.3. For the product state the results are shown in Tables B.4 and B.5. The boldface font indicates most important vibrations. For them, the assignment is given as well. If both intensities were below ten they were cut-off.

Mode	E(harm) cm^{-1}	I(harm) km/mol	E(anharm) cm^{-1}	I(anharm) km/mol
1 OH	**3816**	**15**	**3641**	**11**
2	3085	55	2933	57
3	3073	74	2923	98
4	3068	42	2921	87
5	3065	59	2924	132
6	3058	46	2908	53
7	3033	23	2888	12
8	3020	41	2864	29
9	3017	29	2901	144
10	3015	12	2860	65
11	3012	44	2866	82
12	2961	42	2851	31
14	1499	12	1460	9
19	1397	19	1358	9
28	1250	25	1223	7
30	1149	13	1127	10
31	1092	11	1071	0
32	1088	69	1060	83
34	1050	13	1033	17
36	980	22	960	26
47	343	12	341	15
49	278	116	356	107

Table B.1: Modes, harmonic and anharmonic energies and intensities for reaction **I** for cyclohexanol.

Mode	E(harm)	I(harm)	E(anharm)	I(anharm)
1	3218	4	3076	18
2	3210	15	3076	21
3	3201	17	3066	16
6 NCO	**2362**	**1689**	**2320**	**1274**
7	1649	67	1606	41
9	1560	53	1526	30
16	1146	52	1135	39
17	1102	11	1083	8
24	770	13	760	10
25	765	70	760	45
26	692	20	717	48
27	633	12	627	16
28	623	22	614	18
29	561	24	555	24
33	387	11	385	11

Table B.2: Modes, harmonic and anharmonic energies and intensities for reaction **I** for phenylisocyanate.

Mode	E(harm)	I(harm)	E(anharm)	I(anharm)
1 OH	**3762**	**171**	**3571**	**126**
2	3213	18	3074	31
3	3207	0	3079	69
4	3199	18	3071	19
7	3082	64	2928	92
8	3072	66	2922	73
9	3067	40	2921	103
10	3065	63	2923	216
11	3060	48	2911	60
12	3032	26	2938	16
13	3020	28	2930	17
14	3019	38	2866	497
15	3014	18	2853	35
16	3013	32	2853	20
17	2959	36	2849	23
18 NCO	**2339**	**1425**	**2302**	**1179**
19	1647	53	1604	27
21	1546	71	1513	36
23	1499	11	1452	3
30	1397	20	1354	13
38	1299	15	1270	11
41	1254	28	1227	3
44	1183	7	1158	17
45	1156	12	1132	2
46	1147	40	1140	27
47	1109	12	1087	8
49	1090	94	1059	91
52	1049	14	1034	16
57	981	24	960	23
62	850	0	830	144
63	850	3	832	21
66	777	21	764	17
67	767	64	760	49
68	697	20	697	32
69	650	37	642	31
71	560	21	559	18
72	556	11	553	8
74	486	78	461	4
76	456	5	447	39
77	451	68	425	196

Table B.3: Modes, harmonic and anharmonic energies and intensities for reaction **I** for initial state.

Mode	E(harm)	I(harm)	E(anharm)	I(anharm)
1 NH-stretching	**3630**	**32**	**3466**	**24**
3	3208	19	3065	24
4	3193	24	3054	25
6	3167	13	3020	14
7	3098	36	2951	26
8	3088	37	2940	51
9	3075	34	2928	50
10	3073	17	2929	58
11	3071	57	2927	103
12	3068	74	2926	148
13	3033	36	2876	7
14	3030	5	2886	47
15	3023	24	2903	288
16	3020	27	2863	53
17	3015	22	2859	196
18 CO	**1784**	**267**	**1756**	**146**
19	1653	89	1610	80
20	1640	49	1598	23
21 NH-bending	**1567**	**629**	**1521**	**265**
22	1533	26	1503	17
24	1501	10	1451	22
25	1494	7	1475	34
28	1477	155	1447	6
29	1408	16	1366	0
35	1352	58	1323	123
36	1347	77	1318	14
42	1233	704	1199	537
43	1214	27	1191	43
44	1205	19	1187	28
47	1115	35	1094	27
50	1077	243	1049	19
51	1066	2	1050	17
52	1051	55	1034	86
53	1040	15	1023	18
54	1027	17	1006	28
58	959	9	937	12
64	844	0	826	645
65	844	7	831	66
67	799	0	794	15
68	764	65	755	65
69	757	13	752	3

Table B.4: Modes, harmonic and anharmonic energies and intensities for reaction **I** for product state.

Mode	E(harm)	I(harm)	E(anharm)	I(anharm)
71	702	29	693	40
74	561	68	548	52
76	514	7	514	17
85	234	7	236	12

Table B.5: Modes, harmonic and anharmonic energies and intensities for reaction **I** for product state continued.

B.2 Reaction II

Reaction **II** is composed of 2,4-toluene-diisocyanate and chloralhydrate molecules. The harmonic and anharmonic frequencies calculations have been performed at DFT/B3LYP/ 6-31++G(d,p) level of theory. Four cases have been consider. The results for chloral-hydrate alone are shown in Table B.6. The results for 2,4-toluene-diisocyanate alone are presented in Table B.7. For the initial state the frequencies are shown in Tables B.8 and B.9. For the product state the results are shown in Tables B.10 and B.11. Like for reaction **I**, the boldface font indicates most important vibrations. For them, the assignment is given as well. As before, if both intensities were below ten they were cut-off.

Mode	E(harm)	I(harm)	E(anharm)	I(anharm)
1 OH	**3802**	**50**	**3614**	**43**
2 OH	**3776**	**48**	**3577**	**43**
3	3068	16	2929	18
4	1423	56	1386	33
5	1366	21	1330	504
6	1357	60	1319	468
7	1209	133	1179	111
8	1126	177	1090	165
9	1049	67	1022	64
11	822	130	812	109
12	782	125	766	110
13	614	103	602	89
14	570	38	556	27
16	401	18	391	19
17	345	234	281	189
18	304	33	238	162
19	296	1	293	33
20	270	6	267	13
21	263	3	256	18

Table B.6: Modes, harmonic and anharmonic energies and intensities for reaction **II** for chloralhydrate.

Mode	E(harm)	I(harm)	E(anharm)	I(anharm)
3	3187	10	3048	7
4	3128	17	2983	14
5	3097	12	2944	13
6	3042	25	2944	12
7 NCO	**2370**	**860**	**2323**	**558**
8 NCO	**2354**	**2804**	**2308**	**1905**
9	1654	102	1607	36
10	1611	93	1568	31
11	1569	110	1529	79
15	1476	17	1453	17
22	1158	26	1141	9
23	1097	47	1073	17
25	1017	17	994	16
27	911	51	896	45
28	884	24	877	27
29	822	26	807	20
31	709	12	702	11
32	709	0	744	93
33	630	14	626	12
34	620	36	615	25
36	562	32	555	17
37	558	10	551	20
43	315	17	311	16

Table B.7: Modes, harmonic and anharmonic energies and intensities for reaction **II** for 2,4-toluene-diisocyanate.

Mode	E(harm)	I(harm)	E(anharm)	I(anharm)
1 OH	**3765**	**32**	**3596**	**25**
2 OH	**3694**	**468**	**3488**	**181**
6	3130	17	2975	14
7	3098	11	2947	13
8	3083	15	2945	17
9	3043	24	2937	21
10 NCO	**2363**	**1240**	**2311**	**599**
11 NCO	**2331**	**2002**	**2284**	**737**
12	1652	84	1606	20
13	1614	92	1576	59
14	1565	98	1524	26
15	1531	37	1501	2
19	1430	43	1387	6
20	1425	3	1388	267
21	1422	5	1391	46
25	1282	16	1251	9
26	1259	70	1225	1
27	1234	20	1208	14
29	1161	26	1144	13
30	1116	159	1083	145
31	1105	39	1079	13
32	1078	181	1048	31
34	1018	15	986	14
35	968	14	944	14
37	912	49	895	30
38	907	20	879	30
39	819	27	798	23
40	812	128	802	101
41	804	196	783	191
42	762	19	752	21
43	729	32	717	23
44	717	1	708	10
45	650	11	639	11
46	626	46	619	23
48	603	101	591	683
49	600	113	568	949
50	564	24	560	15
51	559	14	549	4
53	496	27	438	54
54	472	4	458	17
56	418	1	409	2407

Table B.8: Modes, harmonic and anharmonic energies and intensities for reaction **II** for initial state.

Mode	E(harm)	I(harm)	E(anharm)	I(anharm)
57	417	39	408	107
58	407	12	399	39
59	370	81	414	31
61	317	15	310	11

Table B.9: Modes, harmonic and anharmonic energies and intensities for reaction **II** for initial state continued.

Mode	E(harm)	I(harm)	E(anharm)	I(anharm)
1 OH	**3757**	**124**	**3560**	**106**
2 NH	**3624**	**37**	**3465**	**30**
4	3189	11	3055	17
5	3181	8	3041	43
6	3128	16	2981	19
7	3096	13	2942	14
8	3085	12	2948	14
9	3041	30	2942	28
10 NCO	**2364**	**1735**	**2302**	**654**
11 CO/NH	**1776**	**341**	**1749**	**9**
12	1660	147	1622	58
13	1631	101	1595	37
14	1581	308	1547	2
15	1562	402	1524	69
16	1506	11	1477	16
17	1495	36	1450	23
18	1485	8	1442	40
19	1433	30	1397	33
20	1425	24	1389	2548
21	1424	122	1392	1136
22	1383	19	1350	2
23	1348	97	1317	85
24	1320	19	1298	8
25	1269	29	1246	34
26	1257	155	1251	45
27	1245	387	1220	158
28	1231	97	1206	187

Table B.10: Modes, harmonic and anharmonic energies and intensities for reaction **II** for product state.

Mode	E(harm)	I(harm)	E(anharm)	I(anharm)
30	1162	128	1134	22
31	1107	35	1074	28
32	1066	389	1044	175
34	1033	19	1018	3
35	1020	26	999	22
36	994	126	971	141
38	930	115	917	116
39	858	42	847	34
40	844	36	826	4968
41	843	53	825	4563
42	798	183	783	109
43	785	33	777	8
44	762	71	751	32
45	757	19	745	15
46	733	19	724	13
48	650	32	639	21
49	628	11	620	10
51	614	51	609	43
52	572	66	583	22
53	560	19	545	19
54	535	32	525	11
55	503	2	499	38
56	488	143	414	120
62	333	18	327	15
65	271	1	268	15
73	115	0	79	35
74	109	1	88	10

Table B.11: Modes, harmonic and anharmonic energies and intensities for reaction **II** for product state continued.

Appendix C

Overtones and Combination Bands

C.1 Reaction I

The results for overtones and combination bands for reaction **I** are taken from the same calculations as for frequencies, so the functional and basis set are the same. In Table C.1 the outcome is shown for cyclohexanol alone. In Table C.2 the output is shown for phenylisocyanate alone. In Tables C.3 and C.4 the results are shown for the initial state and product state, respectively. The intensities below ten were cut-off.

Mode	E(harm)	E(anharm)	I(anharm)
Overtones			
16	2984	2856	17
Combination Bands			
16 14	2991	2895	17
45 42	1247	1224	16

Table C.1: Modes, harmonic energies, as well as anharmonic energies and intensities for overtones and combination bands for reaction **I** for cyclohexanol.

Mode	E(harm)	E(anharm)	I(anharm)
Overtones			
-	-	-	-
Combination Bands			
16 6	3509	3437	14
24 7	2418	2365	14
24 9	2330	2283	244
24 11	2253	2214	10
33 24	1157	1145	11
35 6	2448	2410	49
35 9	1646	1608	20

Table C.2: Modes, harmonic energies, as well as anharmonic energies and intensities for overtones and combination bands for reaction **I** for phenylisocyanate.

Mode	E(harm)	E(anharm)	I(anharm)
Overtones			
-	-	-	-
Combination Bands			
25 23	2990	2892	13
27 24	2982	2878	29
28 18	3810	3738	13
46 18	3486	3416	11
50 41	2336	2288	55
65 21	2339	2293	12
66 28	2249	2213	41
74 67	1253	1221	50
86 18	2439	2384	15
86 21	1646	1600	16
86 51	1156	1118	18
89 77	509	462	20
89 80	445	415	12

Table C.3: Modes, harmonic energies, as well as anharmonic energies and intensities for overtones and combination bands for reaction **I** for initial state.

Mode	E(harm)	E(anharm)	I(anharm)
Overtones			
24	3003	2867	12
74	1121	1083	19
75	1079	1074	178
Combination Bands			
25 23	3008	2953	15
26 24	2992	2890	15
74 56	1560	1528	14
74 60	1475	1444	24
74 69	1317	1302	28
76 56	1514	1492	12
76 74	1075	1065	77
77 69	1225	1218	16
78 47	1564	1542	81
78 54	1476	1449	221
78 62	1351	1324	11
81 42	1588	1553	52
81 43	1569	1544	57
81 44	1560	1540	35
81 63	1220	1207	19
82 42	1584	1546	32
82 43	1566	1538	81
86 41	1501	1486	15
87 21	1781	1734	81
87 50	1291	1260	12
87 63	1079	1066	43
88 59	1076	1074	281

Table C.4: Modes, harmonic energies, as well as anharmonic energies and intensities for overtones and combination bands for reaction **I** for product state.

C.2 Reaction II

The calculations for overtones and combination bands for reaction **II** are done together with calculations for frequencies, so they have the same level of theory. In Table C.5 the outcome is shown for chloralhydrate alone. In Tables C.6 and C.7 the results are shown for 2,4-toluene-diisocyanate alone. In Tables C.8 and C.9 the results are shown for the initial state. Finally, in Tables C.10, C.11 and C.12 the output is shown for product state. The intensities below ten were cut-off.

Mode	E(harm)	E(anharm)	I(anharm)
Overtones			
16	802	784	15
Combination Bands			
16 15	813	793	26
17 9	1394	1304	10

Table C.5: Modes, harmonic energies, as well as anharmonic energies and intensities for overtones and combination bands for reaction **II** for chloralhydrate.

Mode	E(harm)	E(anharm)	I(anharm)
Overtones			
29	1644	1611	23
36	1124	1111	12
Combination Bands			
12 8	3899	3821	10
13 12	3041	2974	16
15 7	3845	3768	11
25 18	2355	2301	59
27 12	2456	2416	28
27 15	2387	2350	94
27 17	2332	2288	25
30 10	2370	2316	52
30 11	2328	2282	44
30 12	2304	2265	75
31 9	2363	2311	517
31 11	2278	2231	35
31 12	2254	2217	12
31 27	1620	1596	24
38 23	1616	1589	12
39 21	1659	1642	36
43 19	1610	1586	28
44 19	1567	1548	23
48 7	2458	2408	13
48 8	2443	2394	36
48 11	1657	1621	13

Table C.6: Modes, harmonic energies, as well as anharmonic energies and intensities for overtones and combination bands for reaction **II** for 2,4-toluene-diisocyanate.

Mode	E(harm)	E(anharm)	I(anharm)
Combination Bands cont.			
50 7	2428	2377	37
50 8	2412	2364	30

Table C.7: Modes, harmonic energies, as well as anharmonic energies and intensities for overtones and combination bands for reaction **II** for 2,4-toluene-diisocyanate continued.

Mode	E(harm)	E(anharm)	I(anharm)
Overtones			
39	1639	1592	14
46	1252	1237	17
50	1127	1123	13
51	1118	1095	17
58	814	795	25
62	601	594	21
Combination Bands			
18 11	3794	3710	12
31 26	2364	2303	356
32 26	2338	2267	68
37 15	2443	2393	26
37 18	2375	2334	137
37 19	2341	2283	57
37 20	2337	2282	41
37 21	2334	2286	679
38 21	2329	2269	10
42 13	2376	2324	92
42 14	2327	2272	338
42 15	2294	2251	56
43 13	2343	2287	23
43 14	2294	2237	58
43 15	2261	2217	37
43 18	2193	2152	26
47 36	1570	1534	40
47 38	1522	1480	21

Table C.8: Modes, harmonic energies, as well as anharmonic energies and intensities for overtones and combination bands for reaction **II** for initial state.

Mode	E(harm)	E(anharm)	I(anharm)
Combination Bands cont.			
53 48	1099	1025	23
54 31	1576	1539	17
54 48	1075	1048	17
55 33	1531	1465	11
56 53	914	845	21
58 57	824	807	18
59 57	787	824	12
60 24	1652	1609	50
63 23	1618	1584	12
65 40	1080	1066	19
66 61	562	538	22
68 56	601	588	19
71 35	1080	1028	124
71 53	607	520	21
73 10	2434	2359	16
73 28	1259	1223	77
74 18	1532	1468	28
76 10	2416	2338	12
77 2	3742	3523	20
78 2	3714	3455	30
81 2	3701	3311	138

Table C.9: Modes, harmonic energies, as well as anharmonic energies and intensities for overtones and combination bands for reaction **II** for initial state continued.

Mode	E(harm)	E(anharm)	I(anharm)
Overtones			
47	1423	1422	22
50	1240	1215	12
51	1229	1217	20
52	1145	1158	37
54	1070	1050	30
59	820	817	27
Combination Bands			
16 10	3871	3771	10
31 25	2376	2330	10
38 16	2436	2392	12
38 19	2363	2313	379
38 20	2355	2304	17
38 21	2354	2306	25
40 16	2351	2303	30
41 16	2350	2302	18
41 38	1773	1739	116
42 15	2360	2309	29
43 14	2366	2323	427
43 36	1779	1747	85
44 14	2343	2297	78
44 15	2324	2276	26
44 42	1561	1534	28
46 14	2314	2270	14
46 15	2295	2249	11
46 38	1663	1638	12
46 40	1578	1549	21
47 33	1774	1746	43
47 40	1555	1534	24
47 41	1555	1534	30
48 38	1580	1552	224
48 43	1435	1415	41
49 38	1558	1532	122
49 48	1278	1259	10
50 37	1595	1559	18
50 47	1331	1317	12
52 39	1430	1432	14
52 45	1329	1331	32
53 47	1271	1254	11
54 46	1269	1248	18
54 49	1163	1145	80
55 38	1432	1414	26

Table C.10: Modes, harmonic energies, as well as anharmonic energies and intensities for overtones and combination bands for reaction **II** for product state.

Mode	E(harm)	E(anharm)	I(anharm)
Combination Bands cont.			
56 36	1482	1397	11
56 38	1418	1328	13
56 43	1273	1189	13
56 44	1250	1164	13
56 45	1245	1154	36
56 48	1138	1047	17
58 43	1238	1224	23
60 22	1775	1737	185
60 29	1577	1558	19
60 34	1425	1403	54
60 59	802	795	12
61 47	1058	1043	13
62 19	1766	1724	21
62 27	1578	1545	82
62 30	1495	1461	22
62 38	1263	1242	29
63 23	1650	1612	38
63 26	1559	1545	24
63 44	1064	1047	69
64 23	1633	1600	28
64 25	1555	1528	53
64 43	1070	1058	11
65 16	1778	1745	15
65 44	1033	1018	11
66 16	1776	1746	229
66 23	1617	1584	12
66 42	1068	1052	17
67 62	574	560	40
68 21	1651	1611	17
68 23	1575	1537	13
68 34	1260	1239	35
68 40	1071	1047	16
68 41	1070	1046	17
70 32	1238	1207	43
70 49	800	786	16

Table C.11: Modes, harmonic energies, as well as anharmonic energies and intensities for overtones and combination bands for reaction **II** for product state continued.

Mode	E(harm)	E(anharm)	I(anharm)
Combination Bands cont.			
71 36	1157	1123	23
72 20	1561	1514	18
72 31	1242	1210	72
72 48	786	764	17
72 49	764	745	38
75 30	1243	1195	89
75 56	569	473	22
75 59	491	468	13
76 10	2432	2343	29
76 15	1630	1567	14
76 16	1574	1518	114
76 17	1563	1492	50
76 36	1062	1013	21
77 16	1571	1504	16
79 10	2403	2310	30

Table C.12: Modes, harmonic energies, as well as anharmonic energies and intensities for overtones and combination bands for reaction **II** for product state continued.

Published Papers

(1) ***Laser-driven localization of collective CO vibrations in metal-carbonyl complexes***
M. Lisaj and O. Kühn
The Journal of Chemical Physics, 141, 204303, 2014

(2) ***Monitoring the alcoholysis of isocyanates with infrared spectroscopy***
F. Kössl, M. Lisaj, V. Kozich, K. Heyne, and O. Kühn
Chemical Physics Letters, 621, 41-45, 2015

Conference Contributions

(1) ***Multidimensional Quantum Dynamics of Coupled Carbonyl Vibrations***
M. Lisaj and O. Kühn
DPG Meeting, Sttutgart, 2012

(2) ***Laser Control of Bond Breaking***
M. Lisaj
Graduate School, Rostock-Sievershagen, 2013

(3) ***Laser-Driven Wave Packet Dynamics of Metal-Dicarbonyls***
M. Lisaj and O. Kühn
DPG Meeting, Berlin, 2014